

How different is water crystallization
from polymer crystallization
under confinement ?

Dissertation

Zur Erlangung des Grades
„Doktor der Naturwissenschaften“
im Promotionsfach Physikalische Chemie

am Fachbereich Chemie, Pharmazie und
Geowissenschaften
der Johannes Gutenberg-Universität in Mainz

Yasuhito Suzuki
Geboren in Tokyo, Japan
Mainz, Juni 2015

Erster Berichterstatter: [REDACTED]

Zweiter Berichterstatter: [REDACTED]

Zusammenfassung

Ziel der vorliegenden Dissertation war es, Einblicke in das Kristallisationsverhalten weicher Materie („soft matter“), wie verschiedener Polymere oder Wasser, unter räumlicher Einschränkung („confinement“) zu erlangen. Dabei sollte untersucht werden, wie, weshalb und wann die Kristallisation in nanoporösen Strukturen eintritt. Desweiteren ist Kristallisation weicher Materie in nanoporösen Strukturen nicht nur aus Aspekten der Grundlagenforschung von großem Interesse, sondern es ergeben sich zahlreiche praktische Anwendungen. Durch die gezielte Steuerung der Kristallinität von Polymeren könnten somit Materialien mit verschiedenen mechanischen und optischen Eigenschaften erhalten werden. Desweiteren wurde auch räumlich eingeschränktes Wasser untersucht. Dieses spielt eine wichtige Rolle in der Molekularbiologie, z.B. für das globuläre Protein, und als Wolkenkondensationskeime in der Atmosphärenchemie und Physik. Auch im interstellaren Raum ist eingeschränktes Wasser in Form von Eispartikeln anzutreffen. Die Kristallisation von eingeschränktem Wasser zu verstehen und zu beeinflussen ist letztlich auch für die Haltbarkeit von Baumaterialien wie etwa Zement von großem Interesse.

Um dies zu untersuchen wird Wasser in der Regel stark abgekühlt und das Kristallisationsverhalten in Abhängigkeit des Volumens untersucht. Dabei wurde beobachtet, dass Mikro- bzw. Nanometer große Volumina erst ab -38 °C bzw. -70 °C kristallisieren. Wasser unterliegt dabei in der Regel dem Prozess der homogenen Nukleation. In der Regel gefriert Wasser aber bei höheren Temperaturen, da durch Verunreinigungen eine vorzeitige, heterogene Nukleation eintritt.

Die vorliegende Arbeit untersucht die sachdienlichen Phasendiagramme von kristallisierbaren Polymeren und Wasser unter räumlich eingeschränkten Bedingungen. Selbst ausgerichtetes Aluminiumoxid (AAO) mit Porengrößen im Bereich von 25 bis 400 nm wurden als räumliche Einschränkung sowohl für Polymere als auch für Wasser gewählt. Die AAO Nanoporen sind zylindrisch und parallel ausgerichtet. Außerdem besitzen sie eine gleichmäßige Porenlänge und einen gleichmäßigen Durchmesser. Daher eignen sie sich als Modellsystem um Kristallisationsprozesse unter wohldefinierter räumlicher Einschränkung zu untersuchen.

Es wurden verschiedene halbkristalline Polymere verwendet, darunter Poly(ethylenoxid), Poly(ϵ -Caprolacton) und Diblockcopolymere aus PEO-b-PCL. Der Einfluss der Porengröße auf die Nukleation wurde aus verschiedenen Gesichtspunkten untersucht: (i) Einfluss auf den Nukleationsmechanismus (heterogen gegenüber homogener Nukleation), (ii) Kristallorientierung und Kristallinitätsgrad und (iii) Zusammenhang zwischen Kristallisationstemperatur bei homogener Kristallisation und Glasübergangstemperatur.

Es konnte gezeigt werden, dass die Kristallisation von Polymeren in Bulk durch heterogene Nukleation induziert wird und dass die Kristallisation in kleinen Poren hauptsächlich über homogene Nukleation mit reduzierter und einstellbarer Kristallinität verläuft und eine hohe Kristallorientierung aufweist. Durch die AAOs konnte außerdem die kritische Keimgröße für die Kristallisation der Polymere abgeschätzt werden. Schließlich wurde der Einfluss der Polydispersität, von Oligomeren und anderen Zusatzstoffen auf den Nukleationsmechanismus untersucht.

Die Nukleation von Eis wurde in den selben AAOs untersucht und ein direkter Zusammenhang zwischen dem Nukleationstyp (heterogen bzw. homogen) und der gebildeten Eisphase konnte beobachtet werden. In größeren Poren verlief die Nukleation heterogen, wohingegen sie in kleineren Poren homogen verlief. Außerdem wurde eine Phasenumwandlung des Eises beobachtet. In den größeren Poren wurde hexagonales Eis nachgewiesen und unter einer Porengröße von 35 nm trat hauptsächlich kubisches Eis auf. Nennenswerter Weise handelte es sich bei dem kubischem Eis nicht um eine metastabile sondern eine stabile Phase. Abschließend wird ein Phasendiagramm für räumlich eingeschränktes Wasser vorgeschlagen. Dieses Phasendiagramm kann für technische Anwendungen von Bedeutung sein, so z.B. für Baumaterial wie Zement. Als weiteres Beispiel könnten AAOs, die die heterogene Nukleation unterdrücken (Porendurchmesser ≤ 35 nm) als Filter für Reinstwasser zum Einsatz kommen.

Nun zur Anfangs gestellten Frage: Wie unterschiedlich sind Wasser und Polymerkristallisation voneinander unter räumlicher Einschränkung? Durch Vergleich der beiden Phasendiagramme kommen wir zu dem Schluss, dass beide nicht fundamental verschieden sind. Dies ist zunächst verwunderlich, da Wasser ein kleines Molekül ist und wesentlich kleiner als die kleinste Porengröße ist. Wasser verfügt allerdings über starke Wasserstoffbrückenbindungen und verhält sich daher wie ein Polymer. Daher auch der Name „Polywasser“.

Abstract

The aim of this study is to understand *how*, *why* and *when* diverse soft materials, such as polymers and water, crystallize under confinement. This is not only a fundamental problem in condensed matter physics but has also important technological applications. For example, the fabrication of polymeric materials with pre-determined crystallinity can result in materials with controlled mechanical and optical properties. On the other hand, confined water exists in globular proteins, cloud nuclei, and icy interstellar particles with respective implications to molecular biology, atmospheric chemistry and interstellar physics and chemistry. Furthermore, controlling ice formation is essential for the durability of building materials like cement. In this respect, efforts to study highly supercooled water are based on decreasing the available sample volume. For example, in micrometer or nanometer volumes water can be supercooled down to $-38\text{ }^{\circ}\text{C}$ or even down to $-70\text{ }^{\circ}\text{C}$ respectively. Under these conditions it will crystallize via *homogeneous* nucleation. In most cases, however, water will freeze at higher temperatures by *impurities* via *heterogeneous* nucleation.

In this work we focus on the pertinent phase diagrams of crystallizable polymers and of water under confinement. As confining medium we employ self-ordered aluminum oxide (AAO) templates with pore diameters ranging from 400 nm to 25 nm. AAO templates contain arrays of discrete, parallel and cylindrical nanopores with uniform pore length and diameter. As such they can be considered as model systems in studying the effect of confinement on crystallization.

We employ different semicrystalline polymers, (poly(ethylene oxide) (PEO), poly(ϵ -caprolactone) (PCL) as well as diblock copolymers of PEO-*b*-PCL) and investigate the effect of confinement on (i) the nucleation mechanism (*heterogeneous* vs. *homogeneous*), (ii) the degree of crystallinity and crystal orientation and (iii) the relation of the homogeneous nucleation temperature to the liquid-to-glass temperature.

We find that polymers crystallize via heterogeneous nucleation in the bulk and predominantly via homogeneous nucleation in the smaller pores with reduced crystallinity (that can be precisely controlled) and exhibit strong crystal orientation effects. AAOs provide an estimate of the critical nucleus size for polymer crystallization. Lastly, we explore the effect of polydispersity, additives and oligomers on the nucleation mechanism.

With respect to ice nucleation within the same AAOs, we find a direct connection between the crystallization pathway and the ice phase that is formed. Ice formation proceeds via heterogeneous nucleation in larger pores and by homogeneous nucleation in the smaller pores. Furthermore, there is a phase transformation from the usual hexagonal ice in the larger

pores to predominantly cubic ice below about 35 nm pores. Interestingly, cubic ice is not metastable to its hexagonal form but a stable phase under confinement at ambient pressure. We further suggest that the stability of cubic ice on confinement reflects on a critical nucleus size being smaller than the pore size. Lastly, we construct the phase diagram of confined water. This can have possible technological applications in various research areas where water exists in confined space including construction materials like cement. In addition, complete suppression of heterogeneous nucleation in AAO pores having diameters ≤ 35 nm opens up the possibility of employing AAO templates as filters for ultrapure water.

Now back to the question: how different is water crystallization from polymer crystallization under confinement? By comparing the two phase diagrams we come to the conclusion that they are not fundamentally different! This, at first site, is surprising, since water is a small molecule much smaller than the smaller pore. However, because of the extended network of hydrogen bonds it behaves similar to a polymer (*i.e.* “polywater”).

Table of contents

Abstract	5
1. INTRODUCTION.....	9
1.1 Crystallization vs. vitrification	9
1.2 Homogeneous/heterogeneous nucleation	10
1.3 Gibbs-Thomson equation	11
1.4 Polymer crystallization.....	13
1.5 Polymer crystallization under confinement.....	19
1.6 From polymer crystallization to water crystallization under confinement	30
1.7 Ice structures	31
1.8 Kinetics of homogeneous nucleation	33
1.9 Ice structures at ambient pressure	34
1.10 Dynamics of bulk ice.....	36
1.11 Design of this study.....	39
2. Experimental Section	42
2.1 Sample preparation and method of infiltration	42
2.2 Materials.....	43
2.3 Infiltration method.....	45
2.4 Etching of aluminum and surface modification	47
2.5 Scanning electron microscopy	47
2.6 Polarizing optical microscopy	49
2.7 Wide-angle X-ray scattering	50
2.8 Differential scanning calorimetry.....	51
2.9 Dielectric spectroscopy	52
3. Results and discussion.....	57
3.1. Crystallization of Poly(ethylene oxide).....	57
3.2. Crystallization of Poly(ϵ -caprolactone)	64
3.3. Origin of heterogeneous nuclei: effects of additives, polydispersity and of a free top layer	78
3.4. Effect of confinement on the crystallization of double-crystalline diblock copolymers composed from PEO and PCL.....	82
3.5. Structure of Ice under confinement	96

3.6. Nucleation mechanism of ice in confinement	99
3.7. Kinetics of ice nucleation confined in AAO	108
3.8. Dynamics of water/ice under confinement.....	114
4. Conclusion.....	118
5. References	120
Appendix A: Abbreviations and acronyms	127
Appendix B: Symbols used in equations.....	130
Appendix C: Derivation of equation (1.4) based on ref [132], [133].....	132

1. INTRODUCTION

1.1 Crystallization vs. vitrification

When materials are cooled from their molten state, they either solidify to a crystal or form a glass [1]. While a crystal is a solid possessing long periodicity, a glass is a disordered solid or a solid with short periodicity. The first path is called crystallization and the second path is called vitrification. Thermodynamically, the most stable state below the equilibrium melting temperature (T_m^0) is that of a crystal. When a material is cooled below T_m^0 , at least some undercooling is required in order to crystallize at some crystallization temperature (T_c). This is because the system needs to overcome an activation energy for nucleation. On the other hand, if the cooling speed is sufficiently fast, crystallization can be avoided [2]. In this case, a glass is formed at the liquid-to-glass temperature (T_g). Figure 1 shows schematically the volume (V) change as a function of temperature for a glass-forming material and for a crystalline material. Vertical axes can also be enthalpy (H) or entropy (S), all being first derivatives of the Gibbs free energy ($V = (\partial G/\partial P)_T$, $-S = (\partial G/\partial T)_P$, $H = -T^2(\partial(G/T)/\partial T)_P$). In principle, crystallization may occur at any temperature below T_m^0 as far as a nucleation event takes place. Below T_g , however, molecular motion is practically frozen and crystallization will not occur at least in a usual experimental time scale.

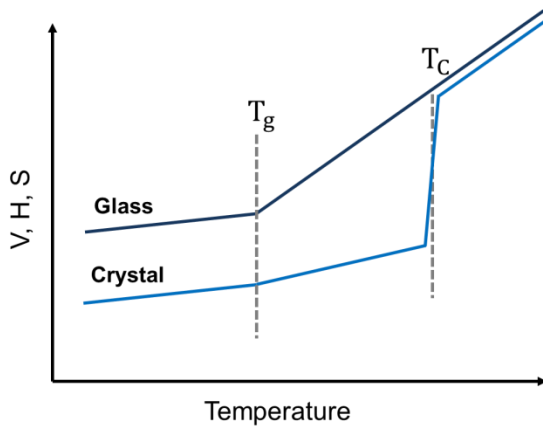


Figure 1. Schematic of the volume (V), enthalpy (H) or entropy (S) change as a function of temperature for (i) a glass-forming material and (ii) a crystalline material.

Although the vitrification phenomenon has been known for a very long time, the molecular origin of glass is not fully understood. It was Philip W. Anderson, a Nobel Prize winner in physics, who wrote *“The deepest and most interesting unsolved problem in solid state theory is probably the theory of the nature of glass and the glass transition”* in 1995 [3]. He continued, *“This could be the next breakthrough in the coming decade.”* Although more than

20 years have passed since then, still the molecular mechanism of glass formation is unsolved. The formation of glass differs from a normal phase transition. First, the liquid-to-glass “transition” is not a well-defined transition in a thermodynamic sense. It strongly depends on sample history and cooling speed. Hence, it has a kinetic origin. Second, at the vicinity of liquid-to-glass temperature, the dynamics of the system are heterogeneous. Dynamic heterogeneity refers to temporally and spatially varying dynamics in the vicinity of T_g [4] [5]. This idea motivated studies of vitrification upon confinement [6] [7]. Much less is known on this issue of crystallization under confinement.

Both crystallization and vitrification are of great importance in material science because all material properties, such as mechanical, optical and electrical are all controlled by the crystal or amorphous states. Although the present study deals mainly with crystallization, it will become evident that there is always a connection between crystallization and vitrification. The discussion of vitrification in the amorphous phase is kept at a minimum, however, it cannot be omitted.

1.2 Homogeneous/heterogeneous nucleation

Most materials crystallize via heterogeneous nucleation. *Heterogeneous* nucleation can be initiated by external surfaces (like dust or bubbles), by additives (such as remaining catalyst, solvent, other chemicals, polymer tacticity and chain polydispersity), external nucleating agents (like graphite, carbon black, titanium oxide) and rough container surfaces, interfaces and possibly interphases. Since these nuclei are already present at the beginning of nucleation, heterogeneous nucleation is athermal and either secondary or tertiary. All these factors can, in principle, catalyze the formation of heterogeneous nuclei and give rise to crystallization at low undercoolings. On the other hand, *homogeneous* nucleation involves the spontaneous clustering of several molecules or segments, the dissolution of small unstable nuclei and the formation and growth of larger stable nuclei above a critical size. In contrast to heterogeneous, *homogeneous* nucleation is primary (*i.e.*, 3-dimensional) and thermal (or sporadic).

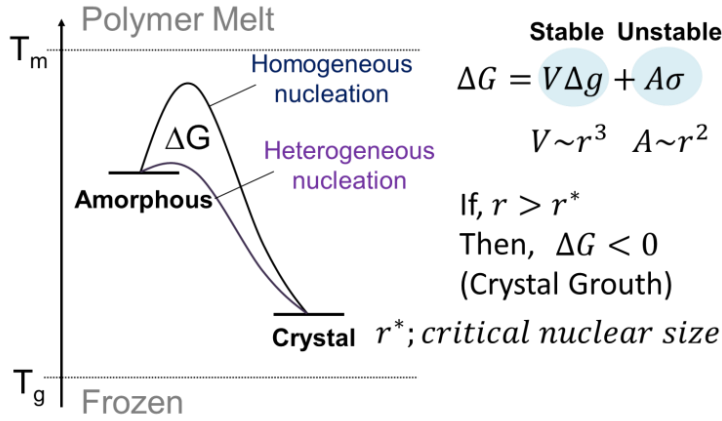


Figure 2. The concept of homogeneous vs heterogeneous nucleation in a highly schematic way. r^* indicates the critical nucleus size.

1.3 Gibbs-Thomson equation

The so-called, Gibbs-Thomson (G-T) equation relates the equilibrium phase transition temperature to the interface surface energy [3]. The total Gibbs free energy, ΔG , for a solid particle, with a volume V and surface area A , submerged in its own liquid is the sum of the volume and interfacial terms

$$\Delta G = V\Delta G_V + A\sigma \quad (1.1)$$

where ΔG_V is the Gibbs free energy difference between the liquid and the solid per unit volume and σ is the solid/liquid surface energy.

At thermodynamic equilibrium

$$d(\Delta G)/dV = 0 \quad (1.2)$$

i.e.,

$$\Delta G_V + \frac{dA}{dV}\sigma = 0 \quad (1.3)$$

The Gibbs free energy difference per unit volume ΔG_V can be described by (see Appendix C.)

$$\Delta G_V = -\Delta S_f \Delta T \quad (1.4)$$

Where, ΔS_f , is the entropy of fusion per unit volume, $\Delta T = T - T_M$ is the difference between the actual interface temperature T and the equilibrium transition temperature, T_M , of a planar

interface. Since for a reversible process, $\Delta S_f = L/T_M$, with L being the volumetric latent heat of fusion, the above equation can be written as

$$\Delta G_V = -L \Delta T/T_M \quad (1.5)$$

and with equation (1.3) yields

$$\Delta T = -\frac{\sigma_{TM}}{L} \frac{dA}{dV} \quad (1.6)$$

In the case of surfaces with principal radii of curvature r_1 and r_2 , the mean curvature K is defined as

$$K = (1/r_1 + 1/r_2) = dA/dV \quad (1.7)$$

so that

$$\Delta T = -\frac{\sigma_{TM}K}{L} = -\frac{\sigma_{TM}}{L} \left(\frac{1}{r_1} + \frac{1}{r_2} \right) \quad (1.8)$$

The above equation is the general form of the Gibbs-Thomson equation. The point of this equation is that the change in temperature of a phase transition is proportional to surface energies and the mean curvature K . Therefore, upon confinement, the smaller the pore size of the confining media is, the lower the phase transition temperature. In addition, K depends on the shape of the confining medium. G-T equation is applied only for the melting process since it is only valid for the equilibrium state.

Jackson and McKenna [8] applied the G-T formalism to the melting behavior of organic materials confined in porous solids. They used *cis*-decalin, *trans*-decalin, cyclohexane, benzene, chlorobenzene, naphthalene, and heptane. The confinement medium was pore glasses and the pore diameter, d , was in the range of 4-73 nm. They employed the G-T equation in the following form:

$$\Delta T_m = T_{bulk} - T_{confinement}(d) = 4\sigma_{sl}T_m/(d\Delta H_f\rho_s) \quad (1.9)$$

where σ_{sl} is the surface energy of the solid-liquid interface, T_{bulk} is the normal (bulk) melting point, $T_{confinement}(d)$ is the melting point for crystals of size d , ΔH_f is the bulk enthalpy of fusion (per g of material), and ρ_s is the density. The following assumptions were made: (a) the crystal size is identical to the pore size, (b) σ_{sl} is isotropic, and (c) the crystal size is sufficiently large so that the material retains its bulk properties for ΔH_f and ρ_s .

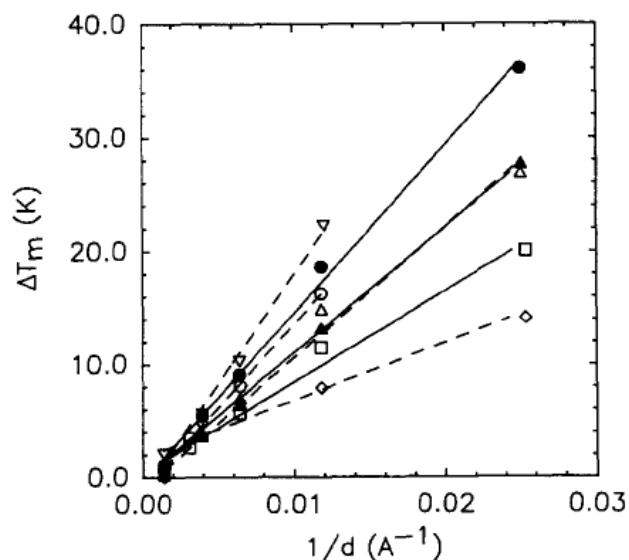


Figure 3. Experimental values of $\Delta T_m = T_{bulk} - T_{confinement}$ for different organic materials plotted as a function of the reciprocal pore diameter. The lines through the data are linear regressions fits. (Figure is taken from ref. [8].)

Figure 3 depicts the change in melting temperature, ΔT_m , for different organic materials as a function of reciprocal pore diameter [8]. It shows a linear dependence of ΔT_m for all organic materials on reciprocal pore diameter. Subsequently, from the slope the σ_{sl} was evaluated.

G-T equation can be applied for the melting of semi-crystalline polymers as well. In this case, it is assumed that lamellar thickness corresponds to the pore diameter.

1.4 Polymer crystallization

It is known that polymers with certain tacticity and high symmetry can crystallize under certain conditions. However, even highly crystalline polymers contain some amount of amorphous segments between the crystalline parts (*i.e.*, they are semi-crystalline). Polymer crystallization has been studied for more than 60 years, however several issues/areas remain open. It was Keller [9] and Fischer [10] who first proved that polymer chains are folded back and forth forming a lamellar structure. Keller, for example, successfully made polyethylene single crystals from a dilute solution of xylene and observed them by TEM. The lamellar thickness was around 110 to 140 Å, *i.e.*, much shorter than the contour length of a single

polymer chain ($\sim 2000 \text{ \AA}$). Based on these observations, he proposed the folded-chain model that also satisfies the density of amorphous and crystalline parts being different by $\sim 15\%$. [11] The general shape of the single crystals and the chain axis orientation was also reported by Fischer and Till in the same year [10,12]. In 1960, Lauritzen and Hoffman proposed a theory of crystal growth that formed the dominant picture for several decades (LH theory). In more recent years there have been experimental observations that contradict some of the LH predictions. In an effort to account for these new experimental data, Strobl proposed a model of polymer crystallization (2009) [13]. The details of Strobl's theory will also be discussed later.

Lauritzen and Hoffman (LH) (1960) established a theory of polymer crystallization that has been widely accepted for several decades. It was already known from experimental observations that polymer crystallization can occur only within a temperature range, *i.e.*, below the equilibrium melting temperature (T_m^0) and above the glass temperature (T_g). Figure 4 provides with experimental data of growth rates from a polymer crystal as a function of temperature obtained by polarizing optical microscopy (POM). Lauritzen and Hoffman defined an upper limit for the growth rate located at the equilibrium melting temperature (T_m^0), corresponding to the melting temperature of an “ideal” polymer crystal (*i.e.* a crystal composed of fully extended polymer chains). Subsequently, they proposed an equation to describe the growth rate (u) of polymer crystals:

$$u = u_0 \exp\left(-\frac{E}{R(T_c - T_0)}\right) \exp\left(-\frac{K_g}{T_c(T_m^0 - T_c)}\right) \quad (1.10)$$

Here, u_0 is the initial growth rate, E is the activation energy for segmental motion, T_m^0 is the equilibrium melting temperature, T_c is the crystallization temperature, T_0 is the “ideal” glass temperature (located $\sim 50 \text{ K}$ below the kinetic glass temperature) and K_g is a constant. Eq. (1.10) captures the basic characteristics of crystal growth with a minimum growth rate near T_m^0 and T_0 . Notice the opposite dependence on T_c of the first term (diffusion term) as compared to the second term (nucleation term). This dependence produces a maximum growth rate at an intermediate temperature T : $T_0 < T_g < T < T_m^0$. Figure 4 (left) [14] provides the experimental proof for the existence of the two limiting temperatures from calorimetry. It depicts linear growth rate as a function of temperature. The maximum growth rate is observed in between T_m^0 and T_g . This experimental result is in a good agreement with Eq. (1.10). Recent development by fast calorimetry enabled the detailed investigation of the

growth rate. Figure 4 (right) reveals that nucleation half-time has two processes that correspond to *heterogeneous* and *homogeneous* nucleation at low and high supercooling respectively [15]. In addition, they suggest a relation of homogeneous nucleation to the polymer segmental relaxation (the α -process).

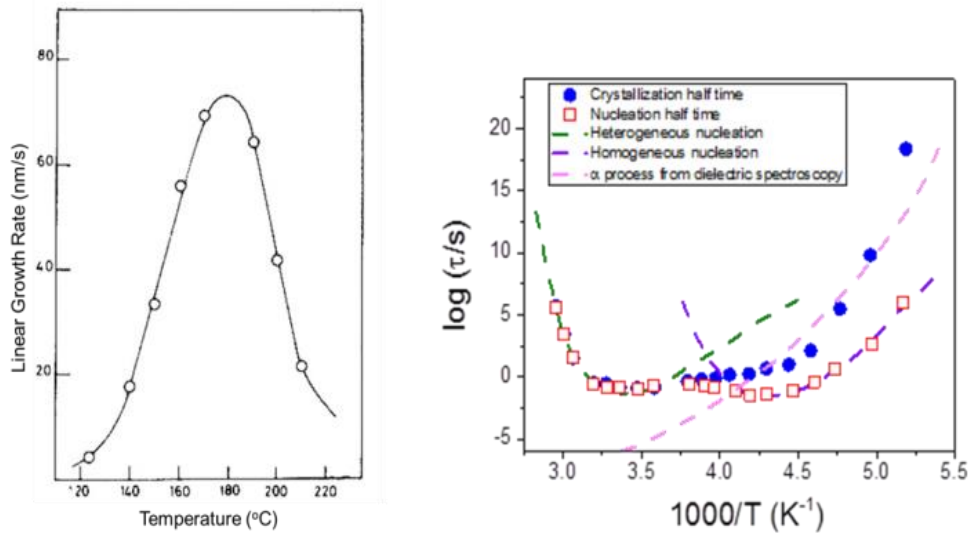


Figure 4. (left) Plot of the linear growth rate versus crystallization temperature for poly(ethylene terephthalate) (PET) [14] [Palys *et al.*, 1980] (right) Activation diagram for polymer crystallization of poly(ϵ -caprolactone) obtained by very fast cooling with calorimetry (5000 K/s). Crystallization half-time (filled blue) and nucleation half-time (empty red) is plotted. Heterogeneous nucleation and homogeneous nucleation times as well as α -relaxation times corresponding to the polymer segmental process obtained from dielectric spectroscopy (dashed pink line) are included [15] [Zhuravlev *et al.*, 2011].

In order to physically explain Eq. (1.10), LH proposed a model of polymer growth depicted in Figure 5 (left). The main assumption is that a single parameter, namely $\Delta = T_m^0 - T_c$, determines the crystal thickness and controls the crystal growth rate.

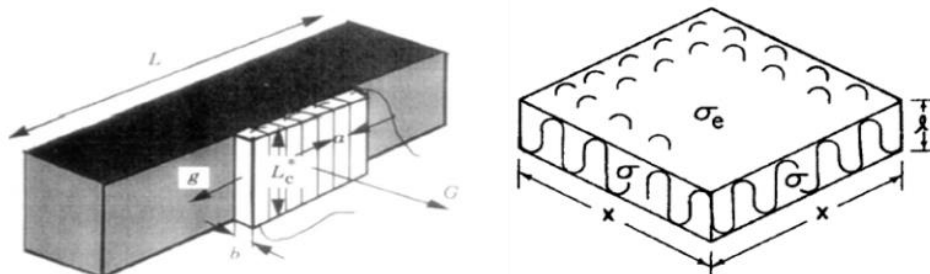


Figure 5. (left) Growth of a polymer crystallite as described by the Lauritzen and Hoffman model [134][Lauritzen *et al.*, 1960] (right) The chain-folded crystal showing surfaces dominated by folds and by extended chains characterized, respectively, from σ and σ_e . [135] [Hoffman *et al.*, 1976]

They further assumed that the apparent melting temperature ($T'_m(d)$) can be described by an extended form of the Gibbs-Thomson equation. They further employed two surface energies: the lateral surface free energy (σ) and fold surface free energy (σ_e) as shown in Figure 5. Under the constraint that the fold surface free energy is much higher than the lateral surface free energy ($\sigma \gg \sigma_e$), the equation reads:

$$T'_m(d) \cong T_m^0 - \frac{2\sigma_e T_m^0}{\Delta H_m} \frac{1}{d} \quad (1.11)$$

In Equation 1.11, $T'_m(d)$ is the apparent melting temperature for a crystal of finite size. The equilibrium melting temperature can be obtained by SAXS by recording the crystal thickness as a function of crystallization temperature. Following LH theory, a plot of $T'_m(d)$ vs $1/d$ provides both the fold surface free energy (σ_e) from the slope and the equilibrium melting temperature (T_m^0) from the intercept. The critical nucleus size of homogeneous nucleation is given by

$$l^* = \frac{4\sigma_e T_m^0}{\Delta T \Delta H_m \rho_c} \quad (1.12)$$

Here, $\Delta T = T_m^0 - T_c$, ΔH_m is the latent heat of fusion and ρ_c is the crystal density.

Although the LH theory has been for “standard” theory in discussing polymer crystallization, there exist some phenomena that cannot be fully explained. For example, Kaji *et al.* in 1990s, observed a SAXS peak prior to the appearance of the crystalline peaks at wider angles (WAXS) [16]. Related articles were published later by his co-workers [17] [18] [19]. They interpreted this weak peak as reflecting long-range density fluctuation prior to crystallization. Cheng *et al.* also studied the same topic and discussed primary nucleation [20]. Long-range density fluctuations were first discussed by E.W. Fischer and co-workers, as characteristic of all amorphous materials in relation to the liquid-to-glass temperature. Subsequently, Hauser *et al.*, measured SAXS of sPP ((s-)polypropylene) and sPPcO_x (copolymers of sPP, chains that included a fraction x of statistically distributed octane co-units) [21]. Figure 6 shows crystallization and melting temperatures as a function of inverse lamellar thickness ($1/d$) for sPPcO_x measured by SAXS. In this system, octane co-units are excluded from the crystal being displaced in the amorphous part. A single “crystallization” line was found for all systems independent from the number of octane co-units. Despite this the melting line was strongly depended on the copolymer. As a result,

crystals of the same thickness could melt at a different temperature. This result contradicts the main assumption of LH theory, namely that the crystal thickness is controlled only by the degree of supercooling (*i.e.*, by the value of ΔT alone). These results imply that there must be another state of crystallizable polymers with some additional characteristic temperatures.

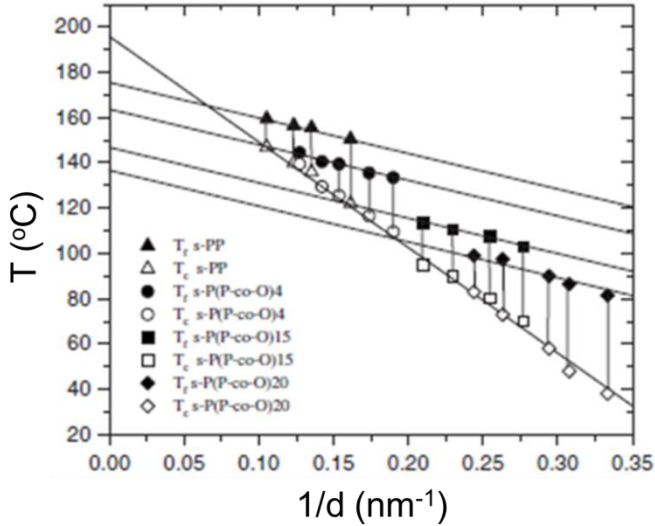


Figure 6. SAXS measurements of sPP ((s-) polypropylene) and sPPcO_x (copolymers of sPP, chains that include a fraction x of statistically distributed octane co-units). Lamellar thickness (d) is plotted as a function of temperature. Empty symbols denote crystallization line and filled symbols denote melting line [21] [Data from Hauser *et al.*, 1998].

In an effort to explain the above results, **Strobl (2009)** proposed a modified theory of polymer crystallization suggesting an intermediate state in the crystallization process. He observed (Figure 6) that the thickness of crystals formed at relatively high temperature was in agreement with the LH theory. However, lamellar thickening occurred for polymers with lower crystallization temperatures. Lamellar thickening refers to a process where the crystalline lamellar thickness increases at the expense of the amorphous part on heating. He then proposed three characteristic temperatures that control polymer crystallization. In agreement with the LH theory, the equilibrium melting temperature was one of them. A second characteristic temperature was obtained from extrapolation of the crystallization temperatures to $1/d \rightarrow 0$ (T_c^0). For this, he assumed that the crystallization temperature had the same relation to lamellar thickness as the Gibbs-Thomson equation. This temperature was also obtained by the “recrystallization line” assuming that there is a critical temperature at which lamellar thickening takes place:

$$\begin{aligned}
 d_c^{-1} &= C_r(T_c^0 - T) \\
 d_c^{-1} &= C_m(T_m^0 - T) \\
 d_c^{-1} &= C_c(T_c^0 - T)
 \end{aligned}
 \tag{1.13}$$

These temperatures and their relation to the crystal thickness are plotted schematically in Figure 7. Lastly, he analyzed crystal growth rates from POM. Although in LH theory it is assumed that zero growth temperature is identical with the equilibrium melting temperature, he suggested that the zero growth temperature (T_{zg}^0) is slightly lower than the equilibrium melting temperature (that was in agreement with several experimental observations by different authors). Subsequently, he corrected the equation for the growth rate (Eq. (1.10)) taking into account the new zero growth temperature:

$$u = u_0 \exp\left(-\frac{E}{R(T_c - T_\infty)}\right) \exp\left(-\frac{K_g}{T_c(T_{zg}^\infty - T_c)}\right) \quad (1.14)$$

Hence, in the latter model, there are three characteristic temperatures instead of one in the LH theory. These temperatures also imply intermediate stages of polymer crystallization. In order to explain all 3 characteristic temperatures, he proposed a mechanism that is shown in Figure 8. The model is based on a multistage phase crystallization processes. The characteristic lines can be explained by transitions among these states. The model is also in agreement with the observation of long-range density fluctuations corresponding to the mesomorphic “phase”.

We should mention here, that recent attempts to identify the mesomorphic phase by AFM were unsuccessful probably because of the fast time scales involved (fast scanning AFM may be helpful in identifying this mesophase in the future). Nevertheless, the model is a valuable extension of the classical LH theory that accounts for the new experimental observations.

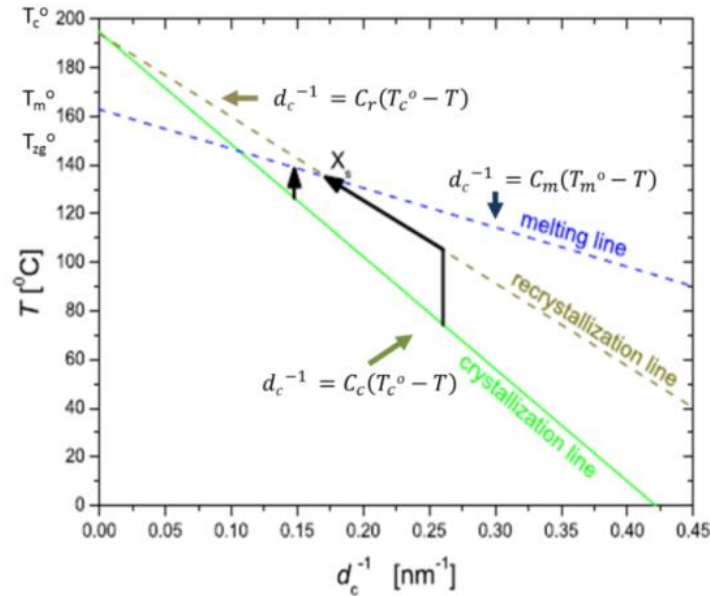


Figure 7. Schematic of crystallization, recrystallization and melting temperatures plotted as a function of inverse lamellar thickness. The latter obtained by SAXS. It is assumed that these data can be fitted linearly. Colored line indicates crystallization line (continuous), recrystallization line (dot), melting line (dash), and transition line (dot and dash). T_c^o , T_m^o and T_{zg}^o are three characteristic temperatures proposed by Strobl [13] [Strobl *et al.*, 2009].

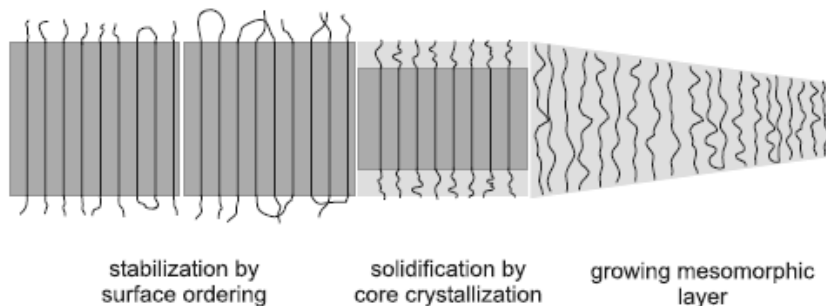


Figure 8. Multistage model of polymer crystal growth proposed by Strobl. First, chain segments from the melt are incorporated in a thin layer with a mesomorphic structure. The mesomorphic layer thickens spontaneously. At critical thickness, a crystal block forms by a first-order transition. Finally, the excess energy of the fold surface is reduced [13] [Strobl *et al.*, 2009].

1.5 Polymer crystallization under confinement

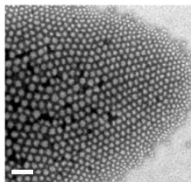

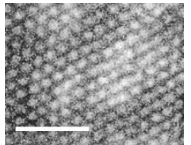
Polymer crystallization under confinement can be fundamentally different from the bulk. Since material properties such as mechanical and optical properties are affected by the degree of crystallinity and crystal orientation, controlling these properties has wide technological applications. In this respect, previous studies [22] of polymer crystallization and peptide

secondary structure perfection [23] under confinement revealed that the degree of crystallinity and α -helical correlation length is decreased under confinement.

The idea of studying crystallization of small amount of material was first developed by Vonnegut [24] who studied crystallization of tin and water in 1948. It is generally assumed that the number of nucleation events is proportional to the volume. Hence, by reducing the sample volume, the probability of nucleation becomes smaller and larger supercooling is required for crystallization. For example, small water droplets can be supercooled down to -70 °C [25]. In early 2000, several studies of polymer crystallization were conducted and the main systems are listed in Table 1. As for confinement media, miniemulsions [26], droplets [27,28] and nanodomains of block copolymers[13]– [34], were employed.

(A) **Miniemulsions:** Taden and Landfester (2003) studied crystallization of the PEO confined in stable nanodroplets with a size of about 100 nm as obtained by the miniemulsion process. One of the main findings was that nucleation in these PEO droplets occurs only at large supercooling. For example, Figure 9 shows DSC measurement of bulk PEO with molecular weight of 8600 g/mol and of the same PEO confined to miniemulsions. While bulk PEO crystallize at 42.8 °C, PEO confined to miniemulsions crystallized at -23.3 °C. In other words, confined PEO requires larger supercooling for nucleation. Judging from the crystallization temperature, it was concluded that homogeneous nucleation took place upon confinement.

Table 1. List of confined systems from earlier studies. TEM image of microdomains in block copolymer (top), TEM image of miniemulsions (middle) and schematic of droplets created by dewetting (bottom). Images are from refs. [26] [27] [31]. White scale bars are 200 nm.

Author (Year)	System	Image
(A) Taden, Landfester (2003)	Miniemulsions	
(B) Massa, Carvalho, Dalnoki-Veress (2003)	Dewetting	
(C) Loo, Register, Ryan (2002)	Block copolymer microdomain	

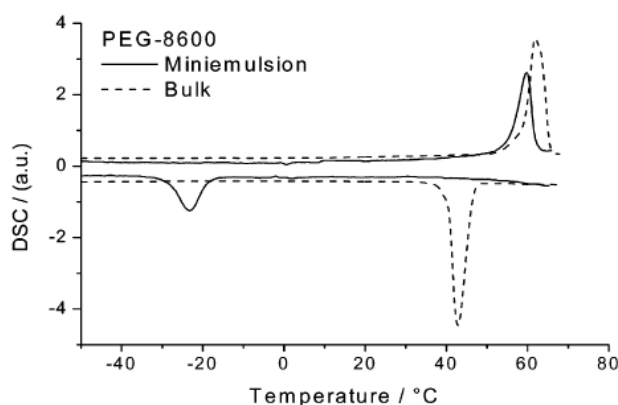


Figure 9. Comparison of DSC data of bulk PEO (dashed line) and PEO confined to miniemulsion (solid line). Typical diameters of miniemulsions are in the order of 100 μm with a broad distribution. Figure is taken from ref. [26].

(B) **Droplets:** Massa *et al.* (2003) studied crystallization of PEO droplets prepared by dewetting (Figure 10). They prepared a sample consisted of a clean Si substrate with a bilayer of PEO on top of PS. The molecular weight of PEO was 27000 g/mol. The thus prepared sample was annealed in vacuum for more than 24 hours at 90 °C which is above the melting temperature of PEO (~ 64 °C) and below the glass temperature of the PS substrate (~ 98 °C). Under these conditions, the PEO film dewets the PS substrate and forms small PEO droplets. Subsequently, they observed the crystallization behavior of PEO droplets by polarized optical microscopy (POM). With nearly crossed polarizers, when an amorphous droplet nucleated and become semi-crystalline, the color of the droplet changed from black to white. The

number of crystalline droplets was counted as a function of temperature. While nucleation temperature of bulk PEO was at 55 °C, the nucleation temperature in small droplets was -5 °C. In addition, they repeatedly measured the crystallization of the same sample. Based on the large supercooling required for small droplets, they concluded that small droplets crystallized via homogeneous nucleation.

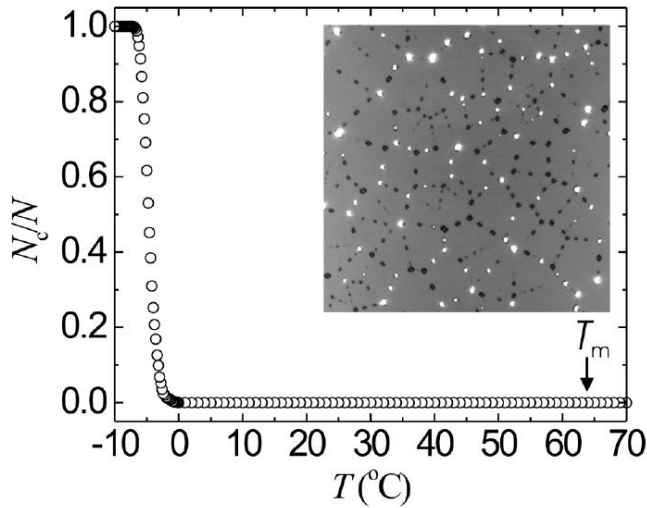


Figure 10. Optical microscopy image of small droplets (insert). White particles indicate crystallized droplets and black ones indicate amorphous droplets. Based on the images, the number of crystallized and amorphous droplets were counted. The fraction of crystallized droplets is shown on the left axis [28].

(C) **Block copolymer nanodomains:** Polymer crystallization within the nanodomains of block copolymers was also studied. Because of the nanophase separation of block copolymers [35], the minority phase is spatially confined. Within mean-field theory, three important parameters control the state of block copolymers: the segment-segment Flory-Huggins interaction parameter, χ_{AB} , the total degree of polymerization, N , and the volume fraction, f . The definition of χ_{AB} is $\chi_{AB} = (Z/k_B T)[\epsilon_{AB} - (\epsilon_{AA} + \epsilon_{BB})/2]$, where ϵ_{AB} is the interaction energy per monomer units between A and B monomers and Z is the number of nearest neighbor monomers to a copolymer configuration cell. Hence, positive value of χ_{AB} correspond to repulsion between the A and B monomers, whereas a negative value signifies mixing of unlike monomers. When the value of N is large, the loss of translational and configurational entropy leads to a reduction of the A-B monomer contracts and thus to local ordering. The entropic and enthalpic contributions to the free energy scale as N^{-1} and χ , respectively. Hence, it is the product χN that determines the phase state of block copolymers. Depending on χN and f , they form different nanophases as schematically shown in

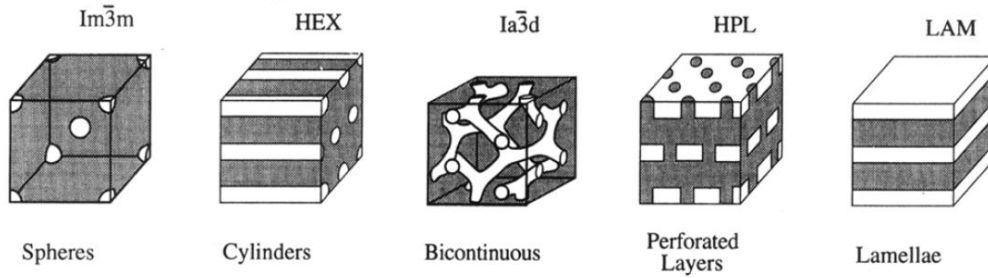


Figure 11. Schematic of five typical block copolymer morphologies. From the left: spheres, cylinders, bicontinuous, perforated layers and lamellae are shown. The figure is taken from ref. [37].

Figure 11. From the left, spheres, cylinders, bicontinuous, perforated layers and lamellae nanophases are shown. Figure 12 depicts theoretical phase diagrams as a function of χN and the volume fraction, f . The left is a mean-field phase diagram of a block copolymer in a weakly segregated limit ($\chi N \sim 10$) showing the different nano-phases [35]. This phase diagram captures the three “classical” phases but fails to account for more complex phases. It was Matsen *et al.*, who employed self-consistent field theory (SCFT) in calculating a more precise phase diagram [36] in calculating a more precise phase diagram. Figure 12 depicts a mean field phase diagram within the SCFT approximation at the intermediate segregation limit ($10 < \chi N < 100$). This phase diagram now captures also the bicontinuous cubic phase with the $Ia\bar{3}d$ symmetry.

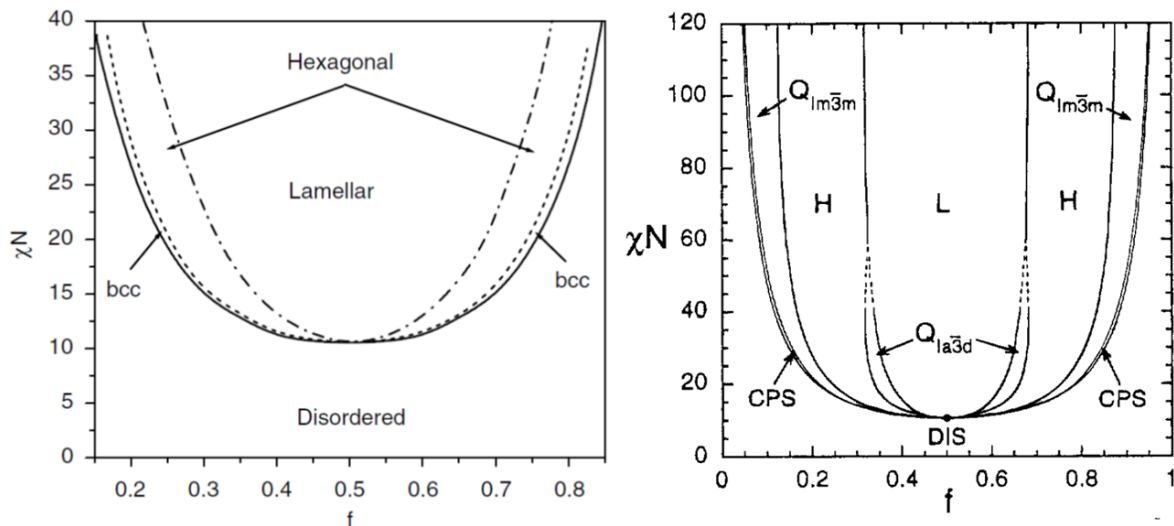


Figure 12. (Left) Theoretical phase diagram for diblock copolymers calculated by Leibler (mean field theory). The phase diagram assumes equal monomer volumes and equal statistical segment lengths for the two blocks [35]. (Right) Mean-field phase diagram within the SCFT approximation for conformationally symmetric diblock copolymers constructed by Matsen. L: lamellar, C: hexagonally packed cylinders, S: spheres packed in a bcc lattice, G: bicontinuous $Ia\bar{3}d$ cubic (double gyroid), S_{cp} : closed packed spheres [36].

A real (*i.e.*, experimental) phase diagram of diblock copolymers is more complex. As an example, Figure 13 describes the phase diagram of the PI-*b*-PS diblock copolymer by Khandpur *et al.* [37]. Here both blocks are amorphous. The asymmetry in the phase diagram originates from the differences in monomer volume and backbone flexibilities of the blocks.

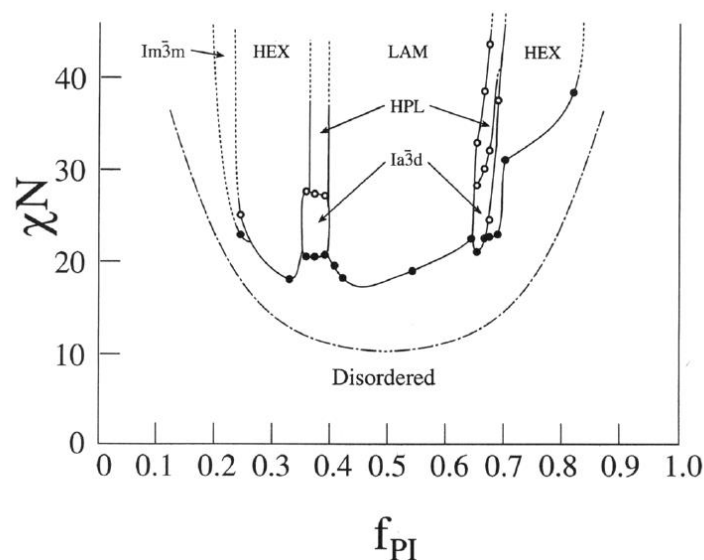


Figure 13. The PI-*b*-PS diblock copolymer experimental phase diagram. The solid curves indicate the approximate boundaries between the ordered phases, and the dash-dot line is the MFT prediction for the order-to-disorder transition temperature (TODT). The figure is taken from ref. [37].

When at least one of the blocks is a semi-crystalline polymer, crystallization strongly affects the phase behavior of the block copolymer. As an example, Figure 14 depicts the phase diagram of PI-*b*-PEO, where PEO is a semi-crystalline block. The main difference between the phase diagrams of PI-*b*-PS and PI-*b*-PEO is the existence of a crystalline lamellar (L_c). For example, when $f = 0.5$, PI-PS forms lamellar (Lam) and this nanophase stays at high χN (*i.e.*, low temperatures). At the same composition, PI-*b*-PEO first forms an amorphous lamellar but at lower temperatures crystallization of PEO leads to crystalline lamellar (L_c). In addition, intermediate phases like the hexagonal phase (Hex) of PI-*b*-PEO can be destroyed at the onset of PEO crystallization resulting in a crystalline lamellar (L_c). These changes in nanodomain morphology upon PEO crystallization are very evident in the phase diagram of Figure 14.

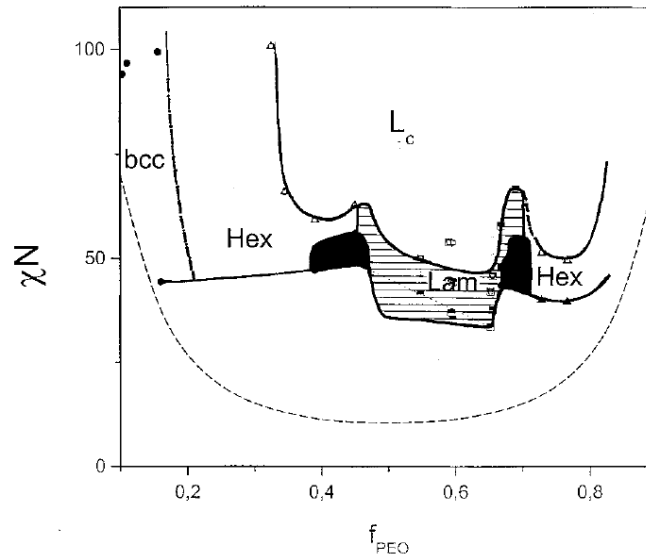


Figure 14. Phase diagram for the system PEO-PI based on 25 PEO-PI diblock copolymers spanning the composition range $0.05 < f_{PEO} < 0.8$. The phase notation is as follows: L_c , crystalline lamellar; Lam, amorphous lamellar; Hex, hexagonal packed cylinders; G, bicontinuous cubic structure with $Ia\bar{3}d$ space group symmetry (gyroid-shadowed areas). Only the equilibrium phase are shown which are obtained on cooling from high temperatures. The dashed line gives the spinodal line in the mean-field prediction. Figure is taken from ref. [136].

An important question here is the conditions under which the crystallization of one block destroys the equilibrium nanophase of the block copolymer. Loo *et al.*, studied diblock copolymers containing polyethylene as the minority block surrounded by a majority phase of a hydrocarbon block. Confinement by block copolymers can be categorized into two different types. First, when the surrounding matrix is glassy, the confinement is “hard”. Second, when the matrix is not glassy, then it is relatively a soft confinement. In this case, upon crystallization the minority block might break the surrounding structure. Loo *et al.* subsequently have shown that polymer crystallization can be classified into the following three different regimes depicted in Figure 15. *Confined* means polymer crystallizes within the nano-domain. *Templated* means that the basic nano-structure is kept but the minority phase can be partially connected. Lastly, “*breakout*” means that because of the polymer crystallization, the nano-domain structure is completely destroyed.

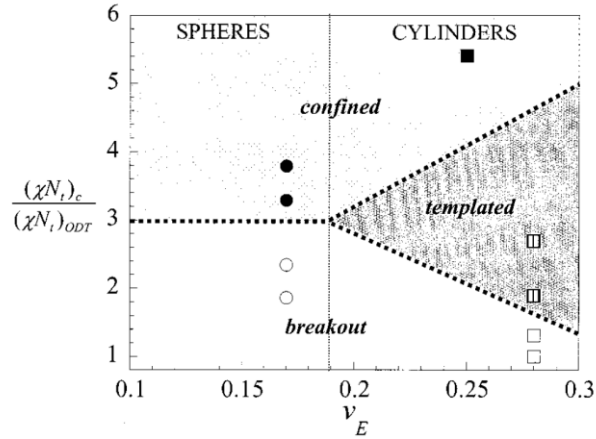


Figure 15. Classification map of crystallization modes in semicrystalline diblocks with rubbery matrices. Open symbols represent samples where the melt mesophase was completely destroyed on cooling (breakout) or where the melt was homogeneous (unconfined); symbols with vertical hatch represent templated crystallization; and filled symbols represent confined crystallization. Circles represent diblocks forming spheres of E; squares represent cylinders. The bold dashed lines are guides to the eye, approximately dividing the region of breakout (bottom) from the region of confinement (top, light hatch) and the region of templated crystallization (right center, heavy hatch) [31].

As an example of confined polymer crystallization in the above mentioned different media, we show, in Figure 16, the crystallization and melting temperatures of confined poly(ethylene oxide) (PEO) within miniemulsions, droplets and microphase separated block copolymers. It is reasonable to assign bulk crystallization to heterogeneous nucleation because bulk polymers almost always contain several impurities. On the other hand, upon confinement homogeneous nucleation with larger supercooling is observed. This result can be understood by the following argument about the volume per heterogeneous nuclei. A typical size of a PEO spherulite is around $300 \mu\text{m}$ giving a volume per heterogeneous nucleus of $\sim 1 \times 10^{-2} \text{mm}^3$. In comparison with this volume, volumes of single droplets, nanodomains and miniemulsions are much smaller (*i.e.*, order of 10^{-12}mm^3). Hence the probability of heterogeneous nucleation is negligibly small upon confinement. Hence, PEO cannot crystallize heterogeneously and crystallize predominantly homogeneously at much lower temperatures.

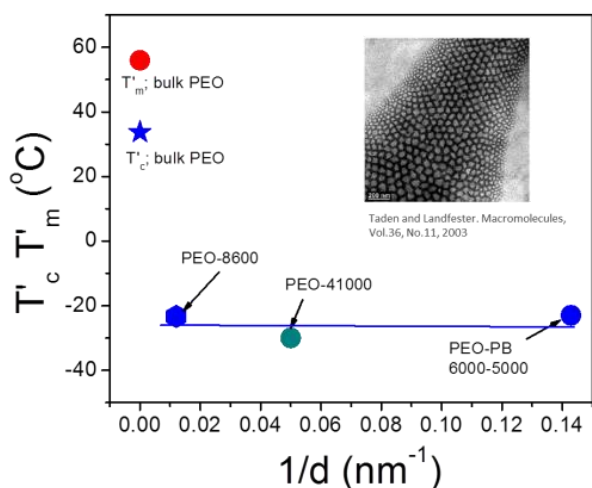


Figure 16. Crystallization temperature of bulk PEO and PEO under confinement in different confinement media ranging from nanodomains of block copolymers, in miniemulsions and in nanodroplets as a function of inverse diameter of confinement. Bulk PEO crystallize at around 30 °C with heterogeneous nucleation. On the other hand, PEO under confinement crystallize at around - 30 °C with homogeneous nucleation.

Apart from these confining media, more recent efforts studied polymer crystallization within well-defined pores of self-ordered anodic aluminum oxide (AAO). The first two such studies were made on polyethylene (PE) and isotactic polypropylene (iPP). Woo *et al.* [38] used AAO templates as a confining media to study crystallization of polyethylene (PE) ($\bar{M}_W = 32100$ g/mol). AAO provides harder confinement in comparison to the above mentioned systems. DSC traces of bulk PE and PE confined to AAO with pore diameters from 110 nm to 15 nm is shown in Figure 17 (left). Upon confinement, sharp exotherms are observed at lower temperatures (75~85 °C) than in the bulk (~117 °C). The low temperature peaks were attributed to homogeneous nucleation. In addition to this, broad features (60~110 °C) were observed in the smaller pores. According to the authors, this is due to the suppression of homogeneous nucleation upon confinement. Hence, they concluded that homogeneous nucleation dominates in 110 nm and 62 nm pores, whereas heterogeneous nucleation prevails in pores having diameters below 48 nm. Duran *et al.* [39] studied the crystallization of isotactic poly(propylene) (iPP) ($\bar{M}_W = 108000$ g/mol) confined to the same AAO templates. Figure 17 (right) provides cooling thermograms of bulk iPP and of iPP confined to AAO with diameters from 380 nm down to 25 nm. Similar to the study by Woo *et al.*, they found 3 different peaks on cooling. However their interpretation was fundamentally different. First, the peak located at nearly the same temperature as with the bulk crystallization temperature was attributed to bulk-like iPP remaining on top of the AAO as thin surface layer (denoted as S in the Figure 17). Second, the peak located at slightly lower temperature than bulk crystallization temperature was attributed to heterogeneous nucleation of confined iPP (denoted as E). Third, the low temperature was assigned to homogeneous nucleation. These,

apparently controversial results call for further studies of confined polymer crystallization in the same AAOs. One objective of the current Thesis is to clarify this picture.

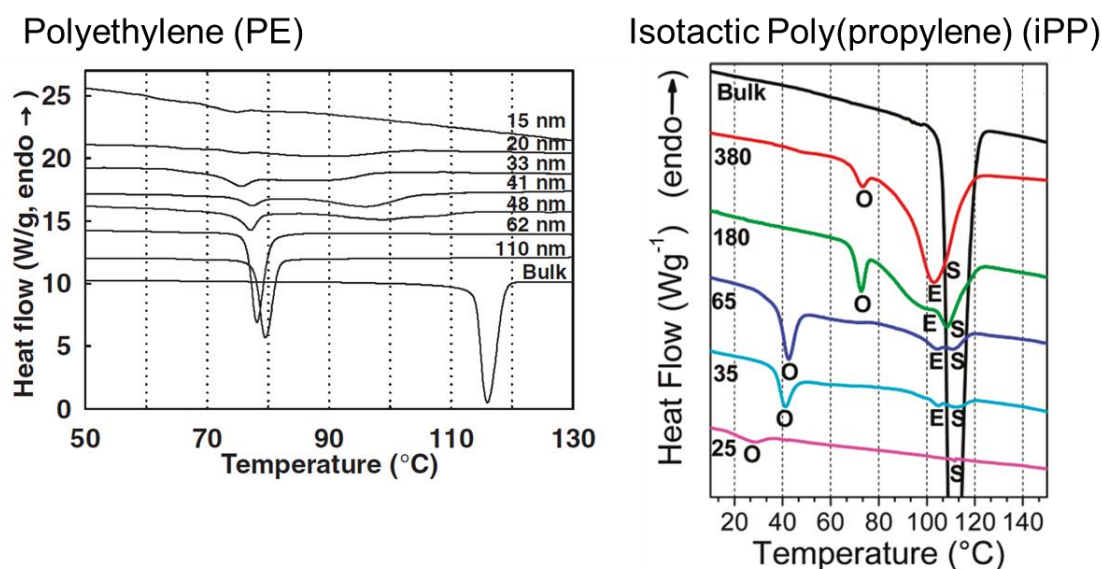


Figure 17. Cooling thermograms of PE (left) and iPP (right), respectively. Bulk trace and traces from respective polymers confined to AAO with diameters ranging from 15 nm to 110 nm (left) [38] and from 25 nm to 380 nm (right) [22] respectively are compared.

Some other recent studies of the effect of confinement within AAOs are summarized below. In parallel with our study on PEO another group reported on the homogeneous nucleation of PEO located in AAO [40]. The same group found that PEO crystal located in AAO with a pore diameter of 20 nm is highly oriented and they reported the kinetics of the unidirectional crystal growth [41]. The influence of gold nanoparticles on PE crystallization in AAO was also studied [42]. While Au nanoparticles only moderately influence bulk crystallization, they significantly affect the crystallization temperature under confinement. They discussed that Au crystals act as heterogeneous nucleation sites. Another study on the self-assembly of nylon-12 nanorods revealed that in small pores, the hydrogen bonding direction of γ -form crystal tend to be aligned parallel to the AAO wall [43]. Another study reported the polymerization of styrene in AAO [41] as well as the kinetics of a fluorinated acrylic monomer [45].

Other studies investigated the effect of confinement on the dynamics of amorphous polymers. In one study a double glass temperature was reported in poly(methyl methacrylate) located inside AAO templates. This was discussed in terms of a two-layer model. Near the pore walls, the strongly confined polymer vitrified at a higher T_g whereas the remaining

polymer in the center of AAOs vitrified at a lower T_g [46]. Other studies of polymer dynamics in amorphous polymers include an investigation of polybutadiene with ^1H NMR [47], of poly(dimethylsiloxane) (PDMS) with neutron spin echo [48], poly(methyl metacrylate) (PMMA) [49], polystyrene-*b*-poly(4-vinylpyridine) [50] and of cis-1,4-polyisoprene using dielectric spectroscopy [51].

1.6 From polymer crystallization to water crystallization under confinement

To our surprise nucleation of ice in confinement bears many similarities to polymer crystallization. Actually, as will be discussed later, this is the main conclusion from this work. Our interest in water stems from several cases where it is found in confined space. Confined water for example exists on earth and even in interstellar space [52,53]. One practical example where water creates severe problems is crack formation in construction materials. Bager *et al.*, for example, studied ice formation in hardened cement paste [54]. Water tends to condense in small space such as cracks because of capillary condensation. Hence, most of the construction materials contain water confined with a variety of length scales. The problem with water in construction materials is that it expands when it freezes. This potentially damages construction materials by inducing further cracks. Figure 18 displays calorimetry data from water confined within hardened cement paste. The graph on the top corresponds to crystallization and the graph at the bottom corresponds to melting. An interesting feature is that while the melting peak is single –albeit asymmetrically broadened–, on cooling there exist multiple discrete crystallization peaks. The authors mentioned that the peaks correspond to characteristic pore size ranges in the pore structure without providing a solid explanation of the feature. At the end of this work, the origin of these multiple peaks will be clarified.

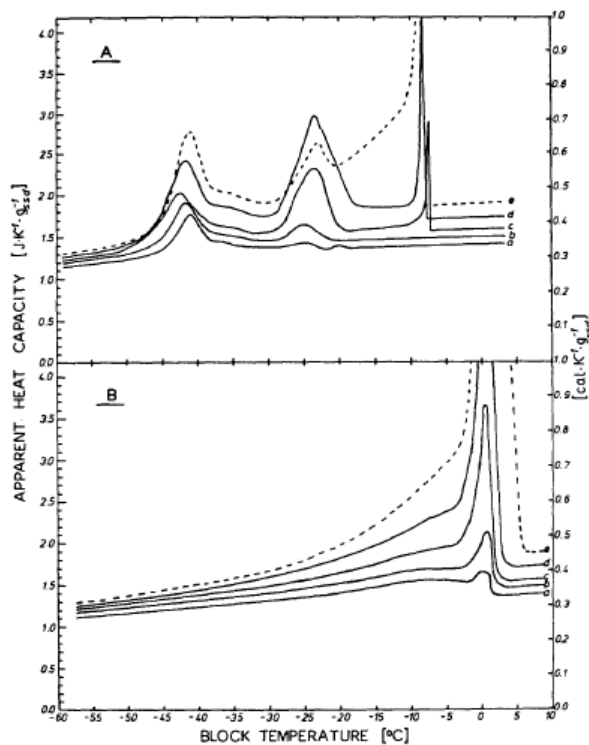


Figure 18. Apparent heat capacity curves for water in cement. A: Cooling and B: Heating. a,b,c,d,e represent water/cement ratios of 0.35, 0.40, 0.45, 0.50, and 0.60, respectively The figure is taken from ref. [54].

1.7 Ice structures

The crystalline forms of bulk ice have been the subject of a long discussion [55]. Figure 19 provides an example of the phase diagram of ice. Under high pressure, many different structures of ice exist; in 2014 the 16th ice structure was declared [56]. Simulations predicted the formation of a metastable structure prior to homogeneous nucleation. The new structure was named Ice 0. [57] This structure is similar to the supercooled liquid with mainly five-membered hydrogen bond rings together with 6- and 7- membered rings as second and third motifs. We recall here that crystalline ice contains only 6-membered rings. Although Ice 0 is not the most stable state, it is the one whose free energy is closest to the liquid water. Subsequently, ice nucleation is triggered by the 6- membered rings in the structure of ice 0. In this sense, the ice 0 acts as a precursor of ice nucleation.

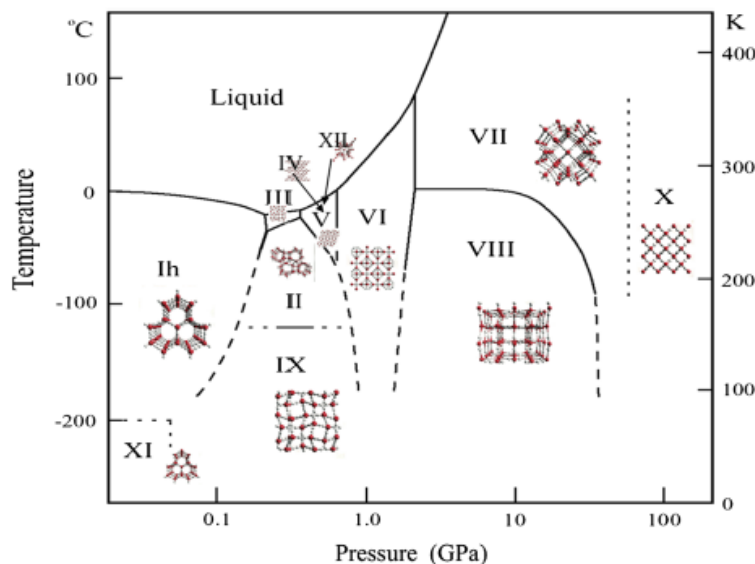


Figure 19. The solid-liquid phase diagram of ice (the triple point and liquid-gas coexistence line lie off the diagram to the left) [137].

In addition to the crystalline structures, amorphous ice can also be formed under certain conditions. Figure 20 illustrates in a schematic way the *amorphous* states of water [58]. At ambient pressure, water is stable below 100 °C and above 0 °C. Liquid water can be supercooled down to the limit of homogeneous nucleation line (-38 °C or below). Amorphous ice can be made by depositing water molecules on a cooled substrate below T_g , a method known since 1913 [59]. In 1984, a new method of making amorphous ice was reported [60]. This method is based on compressing hexagonal ice at a pressure of 10 kbar. The density of amorphous ice made in this way is higher than the vapor deposited amorphous ice. Hence, amorphous ices are categorized into low density amorphous ice (LDA) ($\rho_{\text{LDA}} = 0.94 \text{ g/cm}^3$) and high density amorphous ice (HDA) ($\rho_{\text{HDA}} = 1.19 \text{ g/cm}^3$). In 1985, the same group confirmed that the transition from high density amorphous ice to low density amorphous ice is discontinuous and thus suggested a 1st order phase transition [61].

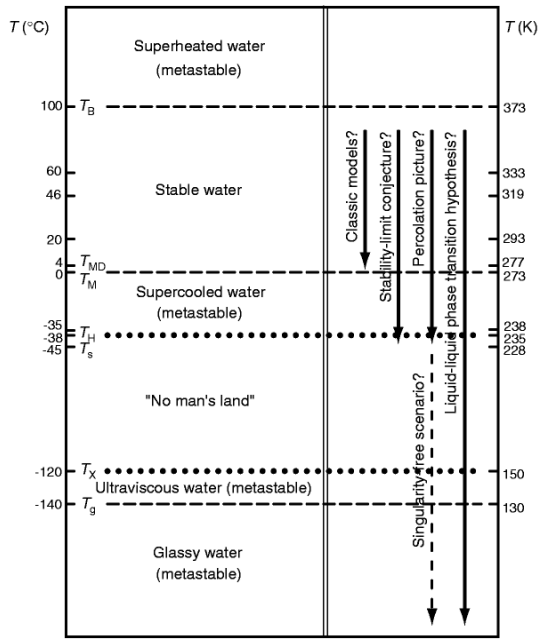


Figure 20. Schematic illustration of different temperature domains, at atmospheric pressure, of amorphous states of H_2O . The temperature range from $-120\text{ }^\circ\text{C}$ to $-38\text{ }^\circ\text{C}$, is known as “No man’s land” because of fast crystallization. Despite this, water confined to nanodroplets can be supercooled well within the “No man’s land”. Figure is taken from ref. [58].

In addition, the diagram of Figure 20 contains another stable state called “glassy water”. The existence of “glassy” water and, more importantly, the detection of the liquid-to-glass temperature is a highly debated issue in literature. Mayer *et al.* [62], for example, prepared hyperquenched glassy water by vapor deposition and recorded a DSC trace on heating starting from temperatures below 120 K. They observed small changes in the DSC signal at 136 K and 138 K. Based on earlier findings, 136 K is widely accepted as the T_g of low density amorphous ice [63]. It should be noted that in order to experimentally obtain T_g , extreme quenching rates are needed. This could potentially affect the properties of the obtained glass. Recently, a second liquid-to-glass temperature corresponding to the T_g of high density amorphous ice (HDA) was proposed at 116 K by Amann-Winkel *et al.* [64]. They prepared HDA by pressurizing hexagonal ice at 77 K. Subsequently, they isobarically annealed the sample at $P \sim 1.1\text{ GPa}$, $T \sim 160\text{ K}$ forming expanded forms of HDA. Subsequently, the thermal and dielectric properties were studied. Upon heating, it first transforms to LDA ice and upon further heating transforms to I_c . However, prior to the transition to LDA, a liquid-to-glass temperature was found at 116 K. Heating from LDA, it shows a conventional T_g at 136 K. The result is confirmed both by DSC and dielectric spectroscopy. This result provided some support to the hypothesis of two distinct supercooled liquid phases of water each with each own T_g [65].

1.8 Kinetics of homogeneous nucleation

Efforts to study highly supercooled water are based on decreasing the available sample volume [24]. For example, water can be supercooled down to $-38\text{ }^{\circ}\text{C}$ or even down to $-70\text{ }^{\circ}\text{C}$ by confinement, respectively, to micrometer or nanometer volumes. Under these conditions, it will crystallize via homogeneous nucleation.

Hagen *et al.* [66,67], for example, used an expansion cloud chamber to create water droplets and analyzed the kinetics. The droplets were photographed and the number of nucleation events was counted. Subsequently, the number of events per unit time and unit volume of liquid was calculated. Figure 21 depicts the obtained nucleation rate as a function of temperature (the units on the vertical axis is $\text{cm}^{-3}\text{s}^{-1}$). The obtained rate provides insights to the process of homogeneous nucleation. First, the smaller the volume is, the less probable the nucleation event to occur. This suggests that by decreasing the sample volume to some nm the homogeneous nucleation temperature will shift to below $-38\text{ }^{\circ}\text{C}$. Second, the slope of the data is very steep in a small temperature range. This is the main reason that the limiting temperature of homogeneous nucleation in samples with sizes in the range from $1\text{ }\mu\text{m}$ to $\sim 100\text{ nm}$ is reported at $-38\text{ }^{\circ}\text{C}$. This also suggests that by decreasing the sample volume to few nm the homogeneous nucleation temperature will shift to temperatures below $-38\text{ }^{\circ}\text{C}$.

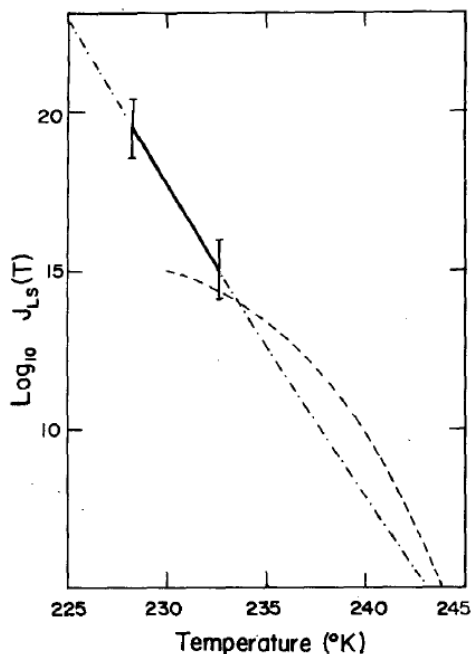


Figure 21. The nucleation rate of homogeneous nucleation of water as a function of temperature. The unit of the vertical axis is $\text{cm}^{-3}\text{s}^{-1}$. The original data is the solid line. The diagonal line is the linear fitting of the original data. The dashed line is the rate from ref [138]. The figure is taken from ref [66].

1.9 Ice structures at ambient pressure

Different ice structures were discussed with respect to Figure 20. These structures form only at very high pressures. On the other hand, when freezing bulk water at ambient pressure, it almost always solidifies to hexagonal ice (I_h) [68]. In fact, until around 1980, it was believed that the only ice structure at ambient pressure is I_h . Indications for naturally formed I_c have only been found in the upper atmosphere. Whalley [69], for example, suggested that the well-known Scheiner's halo around the sun or the moon is caused by light passing at an angle of minimum deviation through octahedral crystals of I_c . Later, a partial I_c phase was reported by rapid quenching of water droplets [70], by condensation of vapor in a supersonic flow [71] and during the homogeneous freezing of aqueous droplets suspended in an oil matrix [72]. Partial I_c has also been reported by annealing the amorphous phase [73], by recrystallization from high-pressure phases [74] [75] and by freezing of water in nanoporous silica [76–81]. More recently, Malkin *et al.* claimed that all cubic ices reported so far are actually not perfect I_c but contain some I_h . They further suggested that this metastable I_c phase, is a stacking – disordered phase containing cubic sequences interlaced with hexagonal sequences, a structure termed stacking-disordered ice (*i.e.*, ice I_{sd}) [68] [82].

As it is shown in Figure 22, the structure of I_h and I_c bear some similarities. They are both composed of hexagonal rings. On each vertex, an oxygen atom exists and between two neighboring oxygen atoms, one hydrogen atom is placed. The hydrogen atom is connected to an oxygen via a covalent bond and to the other oxygen via a hydrogen bond. The only difference between the two structures being that the planes of I_h alternate in an ABAB…… patterns whereas, the planes of I_c alternate in an ABCABC…… repeating structure (Figure 23) [83].

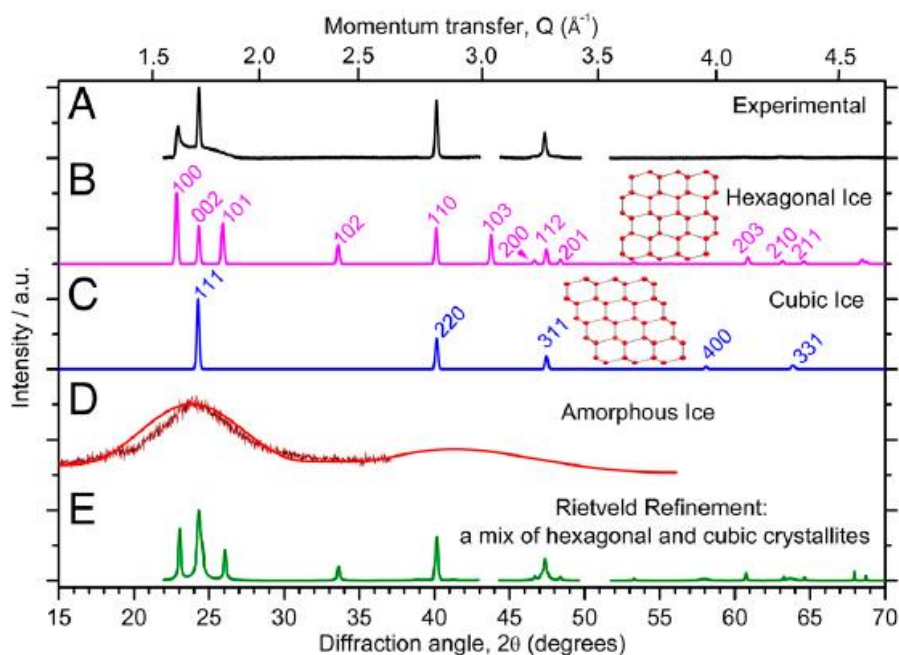


Figure 22. Experimental and calculated X-ray diffraction patterns. (A) An experimental diffraction pattern for water droplets (volume median diameter = 0.9 μm) that were frozen homogeneously with a median freezing temperature of 231.7 K on cooling at 30 Kmin^{-1} recorded at ca. 173 K. (B and C) Simulated diffraction patterns using DIFFaX of fully ordered ice I_h and ice I_c , respectively. (D) The literature diffraction patterns of amorphous ice from Dowell and Rinfret [139] below 113 K (bright red) and Shilling *et al.* [73] at 90 K (dark red). (E) The result of a Rietveld refinement to the experimental pattern, assuming a mixture of well-crystallized ice I_c and ice I_h . The gaps in the experimental pattern correspond to diffraction peaks from the sample support. Figure taken from ref. [68].

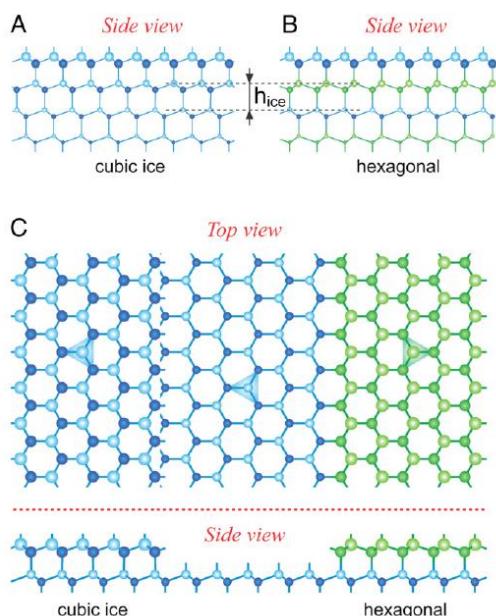


Figure 23. Schematic comparison of the lattices of the two crystalline low pressure ice structures: cubic and hexagonal ice. The oxygen atoms (circles) are connected via H bonds (lines). Higher-lying atoms are represented by larger circles. (A and B) Side views of four bilayers of cubic and hexagonal ice. (C) (Upper) Top view of an ice bilayer (Middle, blue, small circles) that is covered by a partial bilayer according to hexagonal-ice stacking (Right, green, large circles). (Lower) Side view of this arrangement. Within each bilayer the higher oxygen atoms are surrounded by three lower-lying oxygen atoms forming triangles (green or blue) representing the intra-bilayer stacking. The orientation of these stacking triangles alternates from layer to layer in hexagonal ice but not in cubic ice. Taken from Figure [83].

1.10 Dynamics of bulk ice

Despite many attempts, the precise mechanism of ice relaxation, as obtained for example by dielectric spectroscopy, remains unclear [84]. Very few experimental data as a function of frequency exist and even so, these spectra are not in full agreement [85]. In other words, different sources of ice exhibit different relaxation mechanisms. This is most probably because, intrinsic defects of ice and/or impurities may contribute to the dynamics. Unfortunately, nothing is known about the nature of the impurities and their relation to the orientational defects [85]. Second, the relaxation behavior of ice is not simple. As an example, Figure 24 depicts the dynamics of hexagonal ice as reported by Johari and Jones [86]. The data clearly show a change in the relaxation time behavior around $-35\text{ }^{\circ}\text{C}$ and around $-130\text{ }^{\circ}\text{C}$. Based on the activation energy, the relaxation time behavior can be categorized into three temperature regimes: high temperature, intermediate temperature and low temperature regimes (Table 2). It should be noted that the structure of ice measured in this experiment was hexagonal ice and that no phase transition took place in the whole temperature range. Hence, these *dynamical crossovers* cannot be correlated with structural changes.

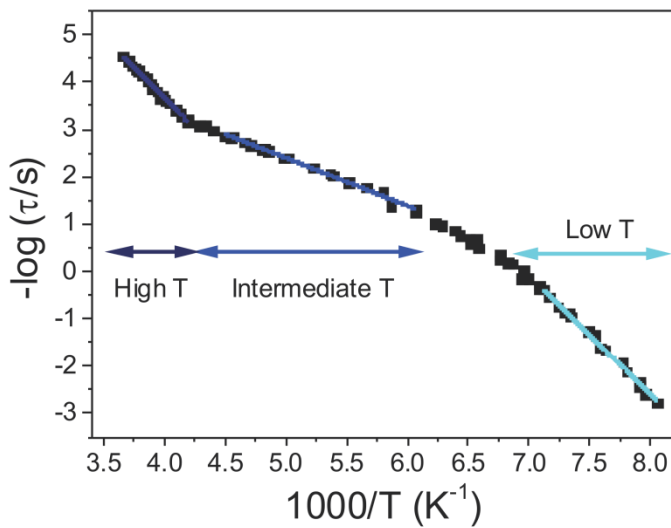


Figure 24. Arrhenius plot of the relaxation times of the ice I_h according to Johari and Jones. The original data was digitized from the ref. [85] and are plotted here.

Table 2. Temperature regimes and associated activation energies for bulk ice.

	Temperature ($^{\circ}\text{C}$)	Activation energy (kJ/mol)
High T	$-35 < T$	49.7
Intermediate T	$-100 < T < -35$	19.1
Low T	$T < -130$	47.8

Johari and Whalley attempted to explain the dynamical crossover between the first two regimes [85]. At the high temperature regime, there was agreement with earlier studies by Auty and Cole [87], and Gough and Davidson [88]. In this temperature regime, the generally accepted mechanism is the production and motion of intrinsically generated defects according to:



where N is a normal O-H bond with one covalent bond and one hydrogen bond while D and L are bonds doubly occupied and unoccupied, respectively, by hydrogen atoms. Schematic representation of L- and D- defects are provided in Figure 25. In the defects, all oxygen atoms keep two hydrogens but the orientation of the water molecules is different.

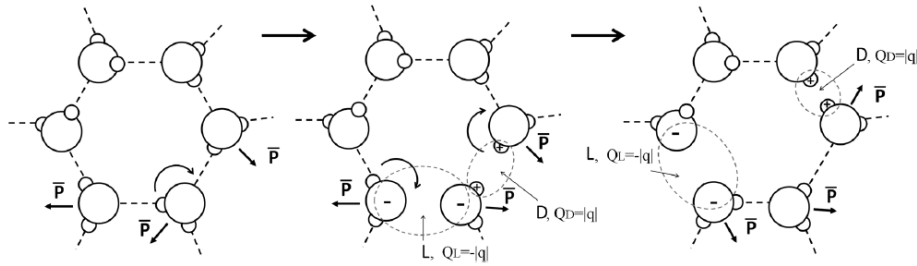


Figure 25. Schematic representation of the generation and migration of a pair of orientational L- and D- defects in ice I_h that result in a change in the direction of the dipole moment of water molecules. Figure is taken from ref. [84].

In order to explain the intermediate and low temperature regimes, the same authors assumed external impurities which generate L- or D- defects with lower energy as



where R_2 and R_3H are chemical or physical impurity centers for L- and D- defects, respectively. Assuming such external impurities, all three equilibria from eq. (1.15) to eq. (1.16) contribute to ice dynamics. If the dominant process changes with temperature, then a dynamic crossover can be obtained. Their explanation can be summarized as follows. At high temperatures, creation and migration of intrinsic L- and D- defects is the dominant mechanism. The sharp transition from high to intermediate temperatures occurs because intrinsically generated defects are suppressed with decreasing temperature and impurity-

generated defects become dominant. On the other hand, the transition from intermediate temperature range to low temperature range is gradual. It is because the dynamics in these temperature ranges originate from 3 different equilibria. Although their explanation captures the general $\tau(T)$ dependence, it relies on unknown sources of external impurities.

Recently, Popov *et al.* [84], studied theoretically the dynamical crossover in the dielectric relaxation behavior of ice I_h . In addition to the L- and D- (orientational) defects, they suggested ionic defects.

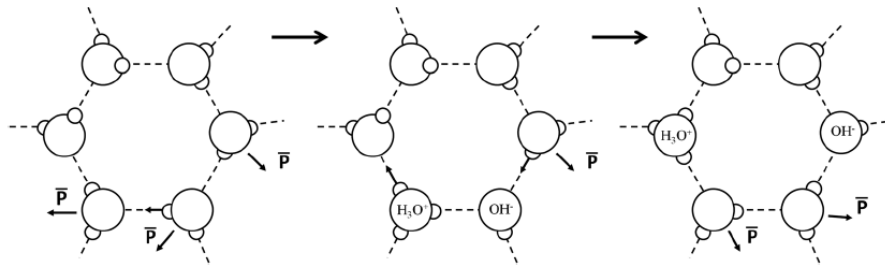


Figure 26. Schematic representation of the generation and migration of an ionic pair of H_3O^+/OH^- defects in ice I_h with a change in the dipole moment of water molecules. The figure is taken from ref [84].

Figure 26 gives a schematic representation of the ionic defects. While in the orientational defects all the oxygen molecules keep two hydrogens, in the ionic defects water molecules exist as H_3O^+ or OH^- . The model takes into account both orientational and ionic defects and successfully captures the dynamic crossover from high temperature range to the intermediate temperature range. As with the model by Johari and Whalley, L- and D- defects dominate the dynamics over the high temperature range. At intermediate temperatures, ionic defects dominate the relaxation. Without introducing unknown external impurities, their model follows the first dynamic crossover. However, the second dynamic crossover at lower temperatures could not be explained. Additional experimental data in this range are needed to address the influence of sample preparation methods on the dynamics.

As described earlier, the existence of a second glass temperature of water has been proposed [64] [89]. The authors first prepared an expanded form of high density amorphous ice (eHDA) and studied its properties. Upon heating, eHDA changed into low density amorphous ice (LDA) and subsequently LDA transformed into cubic ice (I_c). Figure 27 shows the relaxation times of eHDA, LDA and I_c measured by dielectric spectroscopy. Interestingly upon heating, discontinuous changes of the relaxation times were reported at the respective phase transformation temperatures. The same phenomenon was observed for the transition

from LDL to I_c . Using the time of 100 s as representing for the dynamics of the respective glass temperature, they obtained 126 K and 110 K for the T_g for LDA and eHDA, respectively. We will compare these data with our dynamic data of ice relaxation under confinement.

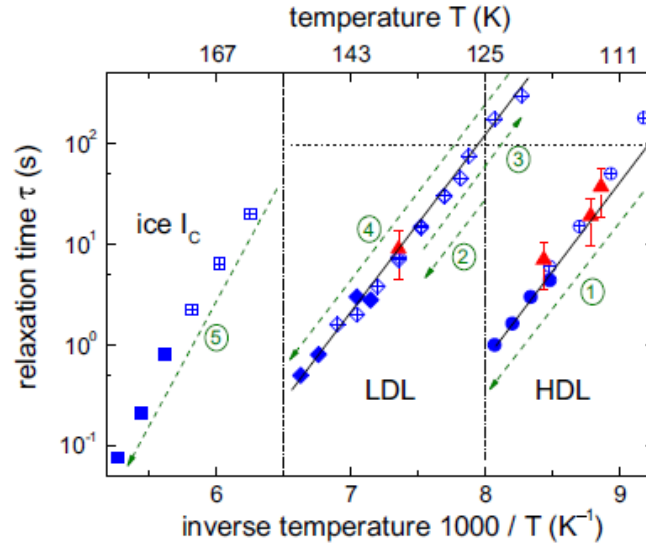


Figure 27. Relaxation map of H_2O phases obtained from eHDA. Blue circles, diamonds, and squares refer to dielectric measurements. The numbered green arrows indicate the thermal history of the samples – that is, the temperature program used. The filled symbols were determined directly from peak frequencies, while the crossed symbols were obtained by applying time-temperature superposition. The dash-dotted lines correspond to temperatures at which transitions occur; the dotted line marks a time scale of 100 s, which is usually associated with the glass transition temperature. Red triangles correspond to the calorimetric relaxation times τ_{cal} , calculated $\tau_{cal} = k_B T_g^2 / (q \Delta E)$, where ΔE is an activation energy obtained from the fitting with Arrhenius equation of the blue data ($\Delta E_{LDL} = 34$ kJ/mol and $\Delta E_{HDL} = 34$ kJ/mol), for heating rates of $q = 5, 10$ and 30 K/min. The obtained values agree excellently with the dielectric time constants (Figure taken from ref. [64]).

1.11 Design of this study

The aim of the present study is to understand *how*, *why* and *when* soft materials such as polymers and water crystallize under confinement. This is not only a fundamental problem in condensed matter physics but has also important technological applications in materials science. For example, the fabrication of polymeric materials with predetermined crystallinity can result in materials with controlled mechanical and optical properties. Of central importance to this discussion is the origin of heterogeneous and homogeneous nucleation and their possible relation to the freezing of the local segmental dynamics at the liquid-to-glass temperature.

In our studies, we employ a model confining medium composed of self-ordered anodic aluminum oxide (AAO). These templates contain arrays of parallel, cylindrical nanopores with uniform geometrical features (pore length and diameter). The main advantage of AAO

templates in comparison to other confining media stems from their quality. The pore depth of the pore used is 100 μm and pore diameters are in the range from 25 nm to 400 nm. Hence, AAO provides 2-dimensional hard confinement with a high aspect ratio. Our interest in this study includes nucleation, structure and dynamics as well as their interrelations. As experimental methods we employ, differential scanning calorimetry (DSC) for studying the mechanism of nucleation, SEM, AFM and X-ray scattering for revealing the structure and dielectric spectroscopy (DS) for the dynamics.

As a model system, we chose poly(ethylene oxide) (PEO). PEO is a polyether with many applications from industrial manufacturing to medicine. Melting temperature ($\sim 70\text{ }^\circ\text{C}$) as well as the glass temperature ($\sim -60\text{ }^\circ\text{C}$) are easily accessible in experiment. In addition, PEO is known to form very large spherulites ($\sim 300\text{ }\mu\text{m}$) in the bulk. The large size of a single spherulite implies that only single nucleation event occurred within the volume at least in the time scale of crystal growth. Based on the huge difference between the volume per heterogeneity in bulk PEO ($\sim 10^{-2}\text{ mm}^3$) and the volume of a single AAO pore ranging from 10^{-8} to 10^{-11} mm^3 , a drastic effect of confinement on PEO crystallization is expected.

Subsequently, we investigate the crystallization of poly(ϵ -caprolactone) (PCL) upon confinement. PCL is also a model biodegradable polymer with a low melting point of $\sim 60\text{ }^\circ\text{C}$ and a glass temperature of about $-60\text{ }^\circ\text{C}$. Despite of the similar melting and glass temperatures to PEO, PCL forms much smaller spherulites ($\sim 50\text{ }\mu\text{m}$) than PEO. This practically implies that PCL contains many more impurities that are expected to act as heterogeneous nuclei.

Having studied both PEO and PCL crystallization under hard confinement, double crystalline block copolymers of PEO-*b*-PCL were subsequently investigated. As discussed before with respect to section 1.5, semi-crystalline block copolymers show different behavior depending on the stiffness of the surrounding media. In the present system, the blocks are confined by both the majority phase and the hard AAO template. We have investigated the effect of double confinement on the nucleation, crystal structure and segmental dynamics under conditions of double confinement. We find that double confinement suppresses the crystallization of one of the blocks.

Finally, water under confinement was investigated. Water is a small molecule with a length of only $\sim 2\text{ \AA}$, *i.e.*, much smaller than the smallest AAO pore diameter. Nevertheless, water molecules are connected by hydrogen bonds forming a network with supramolecular order. Hence, a comparison of the effect of confinement on polymer crystallization as well as on ice formation is still meaningful. Actually a major conclusion from this study is that ice formation under confinement is not fundamentally different from polymer crystallization. We

construct the respective phase diagrams and discuss similarities and differences in their crystallization behavior.

2. Experimental Section

2.1 Sample preparation and method of infiltration

1. Self-ordered anodic aluminum oxide (AAO) templates

Of key importance to the current study is the confining medium. This is provided by self-ordered AAO templates consisted of precisely and homogeneously controlled pores. AAOs were first realized in 1995 by Masuda and Fukuda [90] by the electrochemical oxidation of aluminum. Nowadays it is possible to precisely control the pore diameter by ranging the anodization voltage and the kind of oxidation acids [91]. Figure 28 depicts the diameter of AAO pores as a function of the anodization voltage for different kinds of acids.

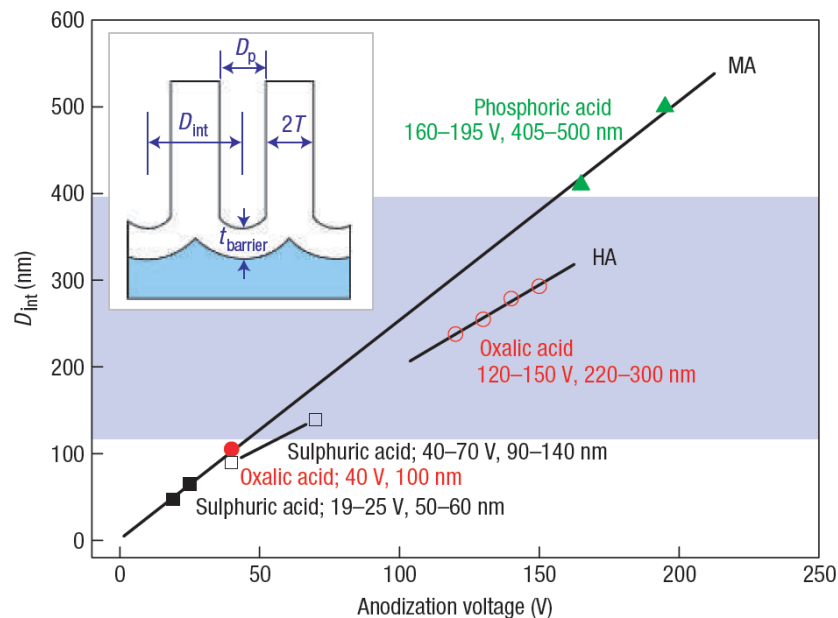


Figure 28. Summary of self-ordering voltages and corresponding inter-pore distance (D_{int}) in conventional MA (mild anodization) in sulphuric (filled black squares), oxalic (filled red circle) and phosphoric acid (filled green triangle), together with recently reported results by Chu *et al.* (open black squares). The open red circles denote HA (hard anodization) in oxalic acid. The figure is taken from ref. [91].

In this study, AAOs with pore diameters 400, 200, 65, 35, and 25 nm and depth of $\sim 100 \mu\text{m}$ were prepared following the procedure above (templates were provided by [redacted]).

2.2 Materials

1. Poly(ethylene oxide)

Poly(ethylene oxide) (PEO) with different molecular weights (Table 3) were synthesized by [REDACTED] ([REDACTED]).

Table 3. Molecular weights and equilibrium melting temperatures of PEO homopolymers. The subscript gives the number-averaged degree of polymerization.

Sample	\overline{M}_w (g/mol)	\overline{M}_n (g/mol)	T_m^0 (K)
PEO ₂₄	1330	1070	331
PEO ₄₆	2460	2005	334
PEO ₁₈₇	9250	8230	344

2. Poly(ϵ -caprolactone)

Poly(ϵ -caprolactone) (PCL) samples with different molecular weights were purchased from Polymer Source Inc. and used as received.

Table 4. Molecular weights and equilibrium melting temperature of the PCL homopolymers. The subscript gives the number-averaged degree of polymerization.

Sample	\overline{M}_w (g/mol)	\overline{M}_n (g/mol)	$\overline{M}_w/\overline{M}_n$	T_m^0 (K)
PCL ₆₈	8900	7700	1.16	348
PCL ₃₁₆	42800	36000	1.19	358

3. Diblock copolymers of poly(ethylene oxide)-*b*-poly(ϵ -caprolactone)

Diblock copolymers of poly(ethylene oxide)-*b*-poly(ϵ -caprolactone) (PEO-*b*-PCL) with three different molecular weights were obtained from Polymer Source Inc.

Table 5. Molecular characteristics and degrees of crystallinity from DSC for the PEO-*b*-PCL block copolymers. The subscript gives the number-averaged degree of polymerization.

Sample	$\overline{M}_{n,PEO}$ (g/mol)	$\overline{M}_{n,PCL}$ (g/mol)	PDI_{PCL}	f_{PEO}^a	$X_c^{PEO}{}^b$ (%)	$X_c^{PCL}{}^c$ (%)
PEO ₁₁₄ - <i>b</i> -PCL ₈₈	5000	10000	1.19	0.32	41	37
PEO ₁₁₄ - <i>b</i> -PCL ₁₅₈	5000	18000	1.48	0.21	37	47
PEO ₁₁₄ - <i>b</i> -PCL ₃₂₅	5000	37000	1.80	0.11	25	27

^a f_{PEO} is the PEO volume fraction based on PEO and PCL densities of 1.239 and 1.187 g/cm³, respectively. ^bFrom DSC based on $\Delta H_0 = 200$ J/g. ^cFrom DSC based on $\Delta H_0 = 148$ J/g

4. Water

Purified water (Satorius arium 611VF) was used primarily in this study. As described in the introduction, impurities play an important role in ice nucleation. In order to examine the effect of water purity, different sources of water were tested: Distilled water (single distillation and double distillation), water purified with Satorius arium 611VF from different location at MPI-P, water from MilliQ purification system from MPI-P and from Frankfurt (MPI-biophysics) as well as commercially available water sources (Roth, Wasser-Ultra-Qualität and VWR, Water Nuclease Free). The different sources of water employed herein are summarized in Table 6.

Table 6. List of different sources of water employed in this study

Water sources	
1	Satorius arium 611 VF purified water (Mainz), MPI-Polymer, lab 2.125
2	Distilled water of No. 1
3	Double distilled water of No. 1
4	MilliQ purified water (Mainz), MPI-Polymer, lab 2.507
5	MilliQ purified water (Mainz, different lab), MPI-Polymer, lab 2.416
6	MilliQ purified water (Frankfurt), MPI-Biophysics
7	Seralpur Delta purified water (Frankfurt), MPI-Biophysics
8	Wasser-Ultra-Qualität (Roth), Commercially available pure water
9	Water Nuclease Free (VWR) , Commercially available pure water

2.3 Infiltration method

1. PEO, PCL, and PEO-*b*-PCL

Infiltration of PEO was performed by two different ways as described below. Typically, 1.5 mg to 10 mg of PEO was infiltrated into the AAO templates. In Table 7, the expected sample masses for complete infiltration of the different AAO pores are listed. The porosity data in Table 7 are based on a water calibration method.

Melt infiltration.

Neat PEO was placed on top of the self-ordered AAO at 373 K for 12 h. Subsequently, polymer/AAO was kept in a vacuum oven (200 mbar) at 373 K overnight. Following this, the infiltrated polymer was brought to RT.

Table 7. Expected mass of sample required for complete infiltration of the different AAOs

	400 nm	65 nm	35 nm	25 nm
Total Area (m ²)	3.1×10 ⁻⁴	3.1×10 ⁻⁴	3.1×10 ⁻⁴	3.1×10 ⁻⁴
Porosity (%)	17.3	17.5	7.3	11.1
Empty volume (m ³)	5.3×10 ⁻⁹	5.4×10 ⁻⁹	2.3×10 ⁻⁹	3.4×10 ⁻⁹
Expected weight (mg)	5.3	5.4	2.3	3.4
Typical weight (mg)	3.0 - 6.0	3.0 - 6.0	1.5 - 3.5	1.5 - 3.5

* Porosity was obtained from the permittivity value of empty AAO and AAO infiltrated with water. As for the density, $\rho = 1 \text{ g/cm}^3$ was used for the estimation.

Solution infiltration.

PEO was dissolved in 50 ml of chloroform (Sigma-Aldrich) and the solution was dropped on top of the AAO membranes. Subsequently, AAO was placed in a vacuum oven (200 mbar) at 373 K for 1 hour. Solution deposition and solvent evaporation were repeated several times (typically 10 times).

In both cases, prior to the DSC and DS experiments, excess PEO was removed from the surface of the AAO membranes with sharp razor blades and soft polishing paper (Buehler Microcloth). Furthermore, to completely remove any remaining polymer, the surface was wiped with a tissue containing small amount of chloroform.

For PEO, no significant effect due to the method of infiltration was observed. For PCL and PEO-*b*-PCL studies, only the solution infiltration method was used because sample removal from the top with this method is the easiest.

2. Water infiltration

A droplet of water was placed on top of the AAO for 10 seconds. Then, the droplet was wiped with a paper. Based on simple experiment with a sensitive balance (Mettler Toledo AX205 balance), it is confirmed that water infiltration takes less than 1 second in accord with the Lucas-Washburn relation (LW):

$$h(t) = \sqrt{\frac{\gamma R \cos\theta}{2\eta}} \quad (2.1)$$

where h is the imbibition length (the pore length in this case), γ is the surface tension, θ is the equilibrium contact angle, R is the pore radius and η is the viscosity. Employing, $h = 100 \mu\text{m}$, $R = 100 \text{ nm}$, $\eta(20^\circ\text{C}) = 0.001 \text{ Pa} \cdot \text{s}$ and $\gamma = 0.071 \text{ N/m}$, results in ms filling times that broadly agrees with our experience of fast infiltration.

Furthermore water evaporates following an exponential decay in around 5–10 minutes. For example, Figure 29 shows the evaporation behavior of water from AAO with different diameters. Typical behavior is that within ~3 min half of the water evaporates and almost all water evaporates in 5 min, at ambient temperature and for the smaller pores.

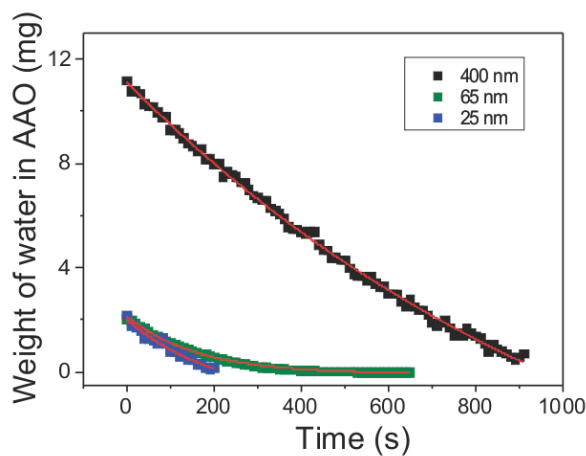


Figure 29. Weight loss of water during evaporation in different AAOs as a function of time. The solid lines represent the result of a fit to an exponential decay $y = A \cdot \exp(-x/t) + y_0$, where A is a constant and y_0 is the initial weight.

2.4 Etching of aluminum and surface modification

1. Etching of aluminum bottom

In dielectric spectroscopy, the bottom aluminum is used as an electrode. However, there are cases (for example, in DSC measurements) where it needs to be removed. In this case, the aluminum substrate is etched away chemically. After the removal of aluminum bottom, the AAO templates are fragile so that they can be easily milled into powder and used in DSC. The etching procedure was as follows: As an etchant, 6.8 g of CuCl_2 powder were dissolved into the mixture of 200 ml of HCl (37%) and 200 ml of H_2O . The top side of AAO was covered with Teflon tape in order to avoid direct contact of sample to the etchant. Then the covered side of AAO was fixed to a glass slide using nail polish. The rim of the bottom side was also protected with nail polish. The remaining rim makes sample handling easier. The glass slide with AAO template was immersed in the etchant for ~1 hour. When etching is completed, the bottom side becomes transparent. Following this, the template was washed with distilled water. The etched template was removed from the glass slide using a sharp razor blade. The template was washed again with distilled water and dried at ambient condition overnight.

2. Surface modification of the AAO walls

Pore walls of AAO were activated in 35% aqueous H_2O_2 (Sigma Aldrich) solution for 2 hour at 318 K and dried at 393 K for 15 minutes. Subsequently, AAO templates were immersed into 4.2 mM solution of octadecylphosphonic acid ($\text{C}_{18}\text{H}_{39}\text{O}_3\text{P}$: ODP) (Alfa Aesar) in n-heptane-2-propanol (Sigma Aldrich) (v/v/5:1). Following this procedure, substrates were washed with copious amounts of n-heptane-2-propanol (v/v/5:1) and sonicated to remove any physisorbed ODP. ODP-modified AAO was washed with ethanol several times and dried overnight under 200 mbar at room temperature.

2.5 Scanning electron microscopy

1. Polymers/AAO

Scanning electron microscopy (SEM) studies were performed using a LEO Gemini 1530 SEM, operated at acceleration voltages from 0.75 to 6 kV. AAO samples infiltrated with polymers were mounted on the sample holder and images of the templates from the top were obtained.

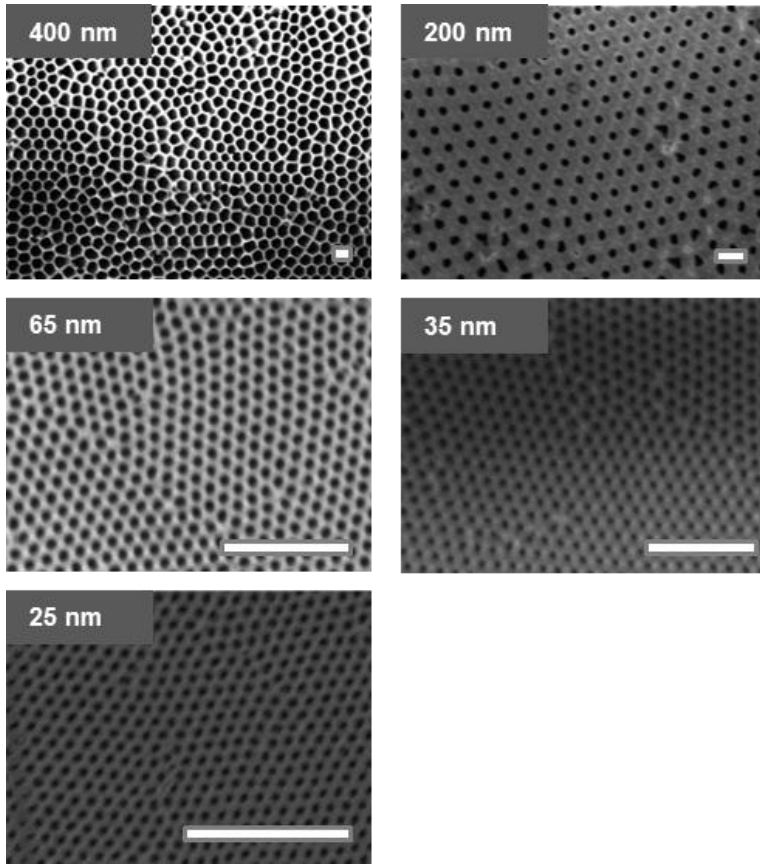


Figure 30. Scanning electron microscopy images of empty AAO with different pore diameters. The white scale bars are 1 μm .

In addition to the top view, cross sectional images were also obtained. For this purpose, AAO samples were frozen to liquid nitrogen and immediately cut using metal cutter. From cross sectional images, it is obvious that polymers filled the AAO pores over their entire length.

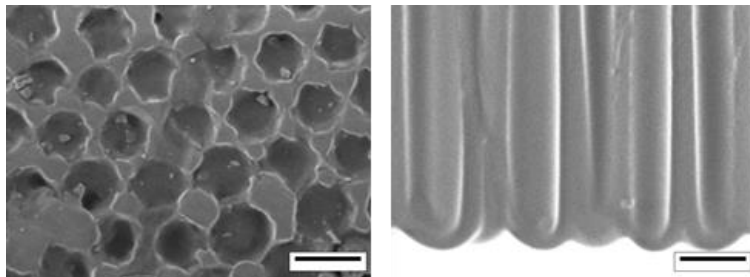


Figure 31. Scanning electron microscopy images of PEO infiltrated inside AAO. Surface (left) and cross-section (right) of infiltrated AAO with a pore diameter of 400 nm. The scale bars correspond to 500 nm.

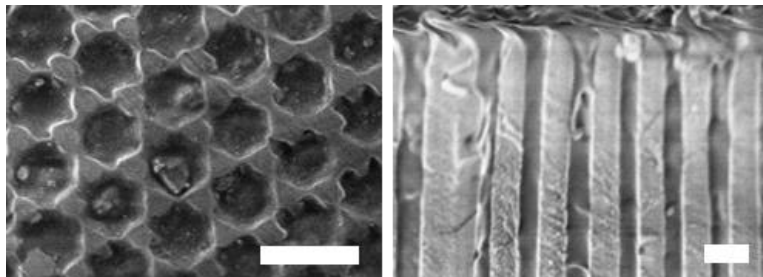


Figure 32. Scanning electron microscopy images of PCL infiltrated inside AAO. Surface (left) and cross-section (right) of AAO/PCL with a pore diameter of 200 nm. The scale bars correspond to 500 nm.

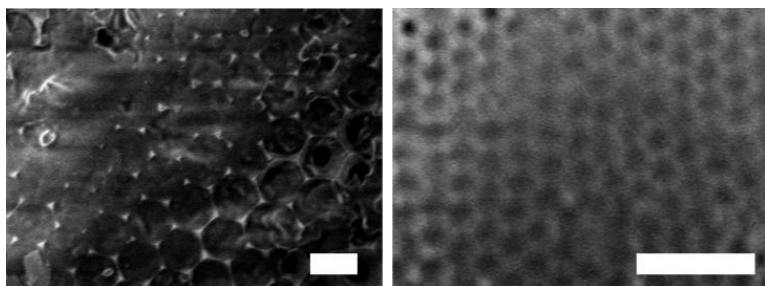


Figure 33. Scanning electron microscopy images of PEO-*b*-PCL infiltrated inside AAO. Surfaces with a pore diameter of 200 nm (left) and a pore diameter of 35 nm (35 nm). The white scale bars correspond to 500 nm.

2. Water/AAO

Low-temperature SEM images were acquired with a Nova600 NanoLab-Dualbeam SEM/focused ion beam (FIB) system equipped with a cryogenic preparation chamber (Quorum Technologies) using a “through the lens” secondary electron detector. In order to increase the contrast between water and the AAO templates, 20 wt% CsCl was added into water. Due to the high electron density of Cs, water becomes “visible” to electrons.

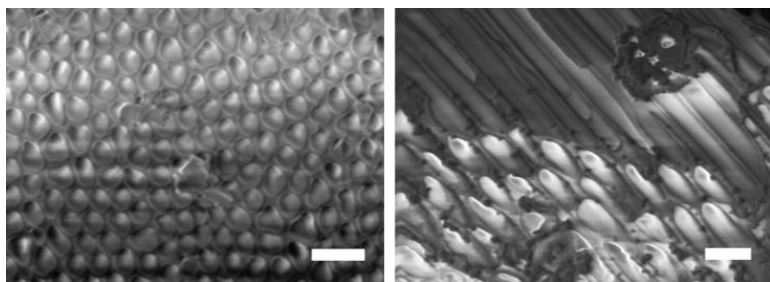


Figure 34. SEM images of water infiltrated to AAO. (Left) and (Right) are top view and cross-sectional image of 400 nm of AAO, respectively. 20 wt% CsCl was added for the better contrast of water and AAO. The scale bars correspond to 1 μm .

2.6 Polarizing optical microscopy

The real-time crystallization and melting of polymers were monitored by polarizing optical microscopy (POM). A 50 mm thick film of the corresponding material was placed between glass slides and mounted on a Linkam THMS 600 hotplate under Axioskope 40 FL optical microscope. Spherulitic growth rates were determined at different crystallization temperatures. Subsequent slow heating yielded the apparent melting temperatures. The corresponding apparent melting temperatures are obtained from the complete loss of birefringence. The equilibrium melting temperatures were estimated from the procedure described on refs [92] [93]. The obtained apparent melting temperature was plotted as a function of the crystallization temperature. In this approach, the temperature sets can be rewritten as

$$M = \gamma \left(\frac{\sigma_e^l}{\sigma_e} \right) (X + a) \quad (2.2)$$

where $M = T_m^0 / (T_m^0 - T_m')$, $X = T_m^0 / (T_m^0 - T_c)$, γ is the thickening coefficient, σ_e^l and σ_e refer to the fold surface free energies, and $a = \Delta H_f C_2 / 2\sigma_e^l$ where ΔH_f is the latent heat of fusion at the equilibrium melting temperature and C_2 is a constant. In the analysis, γ and σ_e^l / σ_e were taken equal to unity. Based on the fitting, equilibrium melting temperatures were obtained. As an example, the original data points and fitting based on equation (2.1) is provided in Figure 35. These values were included in Tables 3 and 4.

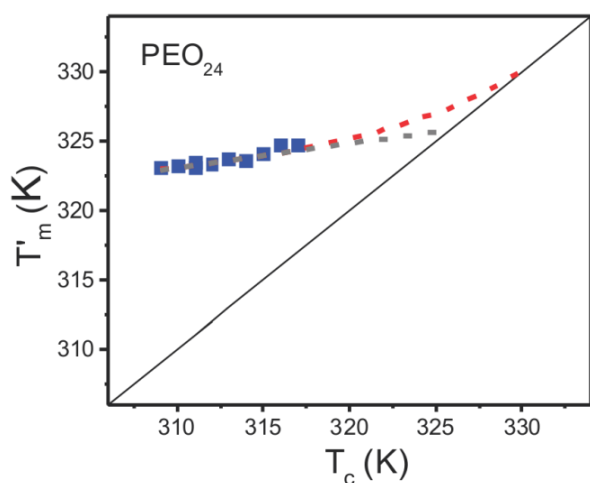


Figure 35. Plot of the apparent melting temperature (T'_m) versus the crystallization temperature (T_c) for PEO₂₄. The solid line has a slope of one. Gray dashed line is a linear fit and the red dashed line is the result of a fit based on equation (2.2).

2.7 Wide-angle X-ray scattering

$\theta/2\theta$ scans were made with a D8 Advance X-ray diffractometer (Bruker). The X-ray tube generator (KRISTALLOFLEX 780) equipped with a Cu anode was operated at a voltage of 40 kV and a current of 30 mA. A 0.3 mm wide aperture (divergence) slit, a 0.3 mm wide scattered-radiation (antiscatter) slit, a 0.1 mm wide monochromator slit and a 1 mm wide detector slit were used. A diffracted beam monochromator was inserted between the detector slit and the detector to suppress fluorescence radiation and the unwanted $K\beta$ radiation. The monochromator contained a graphite crystal ($2d^* = 0.6714$ nm, for the 002 reflection). The $K\alpha_1$ and $K\alpha_2$ peaks could not be separated and an average wavelength of 0.154184 nm was used based on a powder silicon standard of high purity. A scintillation counter with 95 % quantum yield for Cu $K\alpha$ radiation was employed as the detector. In all WAXS experiments surfaces of the AAO membranes were oriented perpendicularly and the AAO nanopore axes were oriented parallel to the plane of the incident and scattered X-ray beam. Thus, only crystals having the corresponding lattice planes oriented parallel to the AAO surface (normal

to the AAO pore axes) contributed to the detected intensity of a specific reflection. Scans in the 2θ -range from 1 to 40° in steps of 0.01° were made following fast cooling (50 K/min) from ambient temperature.

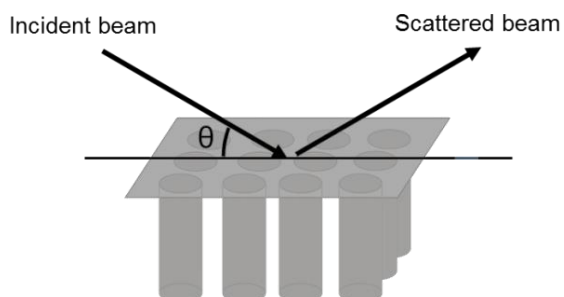


Figure 36. Schematic of the WAXS geometry. The AAO nanopore axes are oriented parallel to the plane of the incident and scattered X-ray beam.

For water infiltrated membranes, in addition to the normal geometry, powder diffraction measurements were performed to exclude crystal orientation effects. In this case the water infiltrated AAOs were frozen to liquid nitrogen and immediately milled to powder. Subsequently, they were inserted in 2 mm capillaries and measured. Scans in the 2θ -range from 20 to 45° in steps of 0.05° were made following fast cooling (50 K/min) from ambient temperature.

2.8 Differential scanning calorimetry

Thermal analysis was carried out using a Mettler Toledo differential scanning calorimeter (DSC-822). Differential Scanning Calorimetry (DSC) traces of bulk polymers were acquired using an empty pan as reference. The polymer mass infiltrated in AAO was estimated from the mass difference between polymer-infiltrated and empty AAO. Samples were weighted with a Mettler Toledo AX205 balance. Prior to DSC measurements, the aluminum substrate was etched away as described in section 2.4. Subsequently, the AAO membranes were milled into powder. Following this, 0.9-8.0 mg sample material was sealed in aluminum pans (100 μl). DSC traces of polymer-infiltrated AAO were recorded using reference pans containing empty AAO pieces of the same pore diameter. All samples were first cooled at a rate of 10 K/min from ambient temperature to 173 K and then heated to 393 K at the same rate under a nitrogen atmosphere. The same cycle was repeated two times. Melting and crystallization points as well as heats of fusion/crystallization were determined from the second heating and cooling thermographs.

Following the above described standard measurements, the rate dependence of the melting and crystallization temperatures was investigated. In this experiment, samples were heated to 373 K and cooling /heating curves were obtained with rates of 10, 5, 2 and 1 K/min.

In addition, isothermal crystallization kinetics of bulk PCL and PCL under confinement were made. In these experiments the samples were first heated to 393 K and held there for 10 min in order to erase any thermal history, followed by rapid cooling (50 K/min) to different final crystallization temperatures where they could crystallize. Due to the limit of rapid cooling rate, only the heterogeneous nucleation was investigated. At the end of the crystallization process, samples were heated to 393 K with a rate of 1 K/min to obtain the corresponding apparent melting temperatures. From the isothermal crystallization experiments, the crystalline mass fraction, $W(t)$, was estimated as

$$w(t) = \frac{\int_0^t \left(\frac{dH_c}{dt}\right) dt}{\int_0^\infty \left(\frac{dH_c}{dt}\right) dt} \quad (2.3)$$

where the numerator and denominator refer to the respective heats generated as times t and at the end of the crystallization process ($t \rightarrow \infty$).

The same DCS setup was used for thermal analysis of water infiltrated AAOs. Prior to DSC measurements, the Al substrates were etched away by using a mixture of HCl, CuCl₂, and H₂O. The water mass in water-infiltrated AAO was estimated from the mass difference between water-infiltrated AAO and empty AAO. Samples were weighed with a Mettler Toledo AX205 balance. The mass of water in AAOs were in the range from 1.2 mg to 4.4 mg. After cleaning the top of the templates, the samples were immediately immersed into liquid N₂ to freeze and avoid evaporation. Subsequently, samples were milled into powder and sealed in DSC aluminum pans (100 µl). DSC traces of water infiltrated AAOs were recorded using reference pans containing empty AAO pieces of the same pore diameter. All samples were first cooled at a rate of 50 K/min from ambient temperature to 173 K and then heated to 303 K at the same rate under a nitrogen atmosphere.

2.9 Dielectric spectroscopy

Dielectric spectroscopy (DS) probes the interaction of electromagnetic waves with matter in the frequency regime between 10⁻² and 10¹² Hz. In this regime, molecular and collective dipolar fluctuations, charge transport and polarization effects at inner and outer boundaries

take place that determine the dielectric properties of the material. Hence, it is possible to obtain the information on dipolar relaxation arising from the reorientational motions of molecular dipoles and electrical conduction arising from the translational motions of electric charges (ions, electrons). [94]

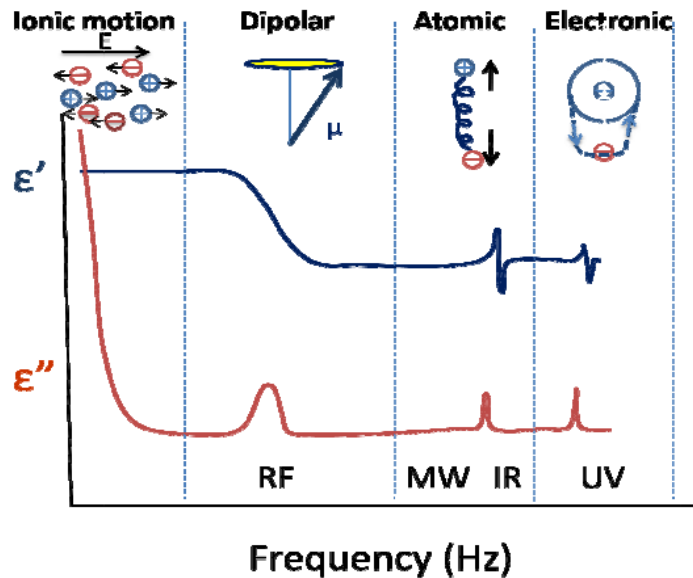


Figure 37. Schematic of the dielectric function plotted over a broad range of frequencies. The real, ϵ' , and imaginary, ϵ'' , parts of the permittivity are shown and various processes are depicted: ionic and dipolar relaxations at lower frequencies, followed by atomic and electronic resonances at higher frequencies taken from ref [94].

Prior to dielectric measurements, all the AAO templates were annealed at 523 K for overnight to remove any adsorbed water. As an example, Figure 38 depicts dielectric loss curves of empty AAO with diameter of 400 nm before (left) and after annealing (right) as a function of frequency at different temperatures as indicated. Clearly, before annealing a relaxation peak attributed to bound water is observed. In addition, this data confirms that the relaxation process observed in this study comes from the infiltrated materials.

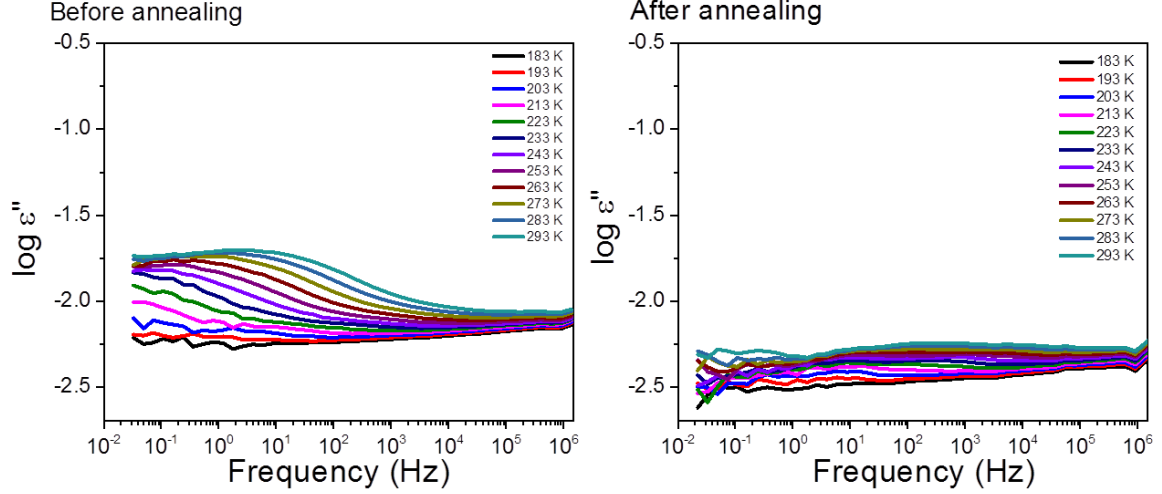


Figure 38. Dielectric loss curves of an empty AAO with diameter of 400 nm before (left) and after annealing (right) as a function of frequency. Annealing was conducted at 523 K overnight. The different temperatures are indicated with different colors.

Dielectric measurements were performed at temperatures in the range of 183-348 K, at atmospheric pressure, and for frequencies in the range from 10^{-2} to 10^6 Hz using a Novocontrol Alpha frequency analyzer as a function of temperature. For the bulk samples, the DS measurements were carried out in the usual parallel plate geometry with electrodes of 20 mm in diameter and sample thickness of 50 μm maintained by Teflon spacers. For polymers confined to AAO, a 10 mm electrode was placed on top of the templates whereas the Al at the bottom of the templates served as the second electrode. The measured dielectric spectra were corrected for the geometry by using two capacitors in parallel (composed of $\epsilon_{polymer}^*$ and ϵ_{AAO}^* and the measured total impedance was related to the individual values through $1/Z^* = 1/Z_{polymer}^* + 1/Z_{AAO}^*$). This allows the calculation of the real and imaginary parts of the dielectric permittivity as a function of the respective volume fractions [23]. The latter were obtained by comparing permittivity of empty AAO and AAO infiltrated with water as described later. In all cases, the complex dielectric permittivity $\epsilon^* = \epsilon' - i\epsilon''$, where ϵ' is the real and ϵ'' is the imaginary part, was obtained as a function of frequency ω and temperature T , *i.e.*, $\epsilon^*(T, \omega)$ [94] [95]. The analysis was made using the empirical equation of Havriliak and Negami [96].

$$\epsilon^*(\omega, T) = \epsilon_{\infty}(T) + \sum_{k=1}^2 \frac{\Delta\epsilon_k(T)}{[1+(i\omega\tau_{HN}(T))^{m_k}]^{n_k}} + \frac{\sigma(T)}{i\epsilon_f\omega} \quad (2.4)$$

Here, $\Delta\varepsilon(T)$ is the relaxation strength of the process under investigation, τ_{HN} is the relaxation time of the equation and m, n ($m > 0, mn \leq 1$) describe the symmetrical and asymmetrical broadening of the distribution of relaxation times, ε_∞ is the dielectric permittivity at the limit of high frequencies, σ is the dc conductivity and ε_f the permittivity of free space. From τ_{HN} , the relaxation time at maximum loss, τ_{max} , is obtained analytically following

$$\tau_{max} = \tau_{HN} \left[\frac{\sin\left(\frac{\pi m}{2+2n}\right)}{\sin\left(\frac{\pi mn}{2+2n}\right)} \right]^{-1/m} \quad (2.5)$$

DS was employed both for PEO and PCL. PEO has a weaker dipole moment (1.04 D) [97] and provides weaker signal as compared to PCL. Nevertheless, the results were qualitatively similar. Henceforth, here only the PCL result will be presented. DS is capable, in principle, to follow the local and global PCL chain dynamics by recording dielectric spectra as a function of frequency at different temperatures. However, a strong contribution from ionic conductivity and the presence of crystalline/amorphous domains and the associated Maxwell-Wagner-Sillars [98] polarization precludes the investigation of the slower chain dynamics in the bulk state. We are thus focusing our attention on the local dynamics below and above the glass temperature (T_g).

In the diblock copolymers of PEO-*b*-PCL, the small volume fraction of the minority component PEO, together with its smaller dielectric strength make PEO invisible in the dielectric spectra. Thus, the local dynamics of PCL in the three copolymers are discussed.

For the water crystallization studies, both isothermal and isochronal experiments were performed. Isothermal measurements were conducted in the same way as with the polymers. For bulk water, DS measurements were carried with a Novocontrol cylindrical cell (BDS 1308) with electrodes of 20 mm in diameter and a sample thickness of ~1 cm.

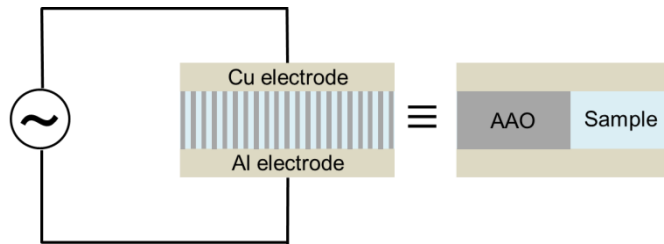


Figure 39. Schematic of the actual geometry used in the dielectric measurements and of the equivalent geometry.

Isochronal measurements were employed to detect the nucleation regimes. Earlier studies have shown that the dielectric permittivity as a function of temperature under isochronal

conditions can be used as a sensitive probe of phase transitions in soft materials [99,100]. The high dielectric permittivity of water can be used as a finger print of the crystallization. In all cases, the complex dielectric permittivity ε^* was obtained at 1 MHz. This allows calculating the real and imaginary parts of the dielectric permittivity as a function of the respective volume fractions by using: $\varepsilon_M^* = \varepsilon_W^* \varphi_W + \varepsilon_A^* \varphi_A$. We employed this relation and obtained the porosity φ_W . For this purpose the measured permittivity values of water infiltrated nanoporous alumina at 293 K were used ($\varepsilon' = 16.3, 16.5, 8.4,$ and 11.4 for 400 nm, 65 nm, 35 nm and 25 nm pores, respectively) together with the AAO value of $\varepsilon_A = 2.6$ [101]. This resulted in porosities of 17.3, 17.5, 7.3 and 11.1 %, respectively for 400 nm, 65 nm, 35 nm and 25 nm pores.

3. Results and discussion

Effect of confinement on crystal orientation

3.1. Crystallization of Poly(ethylene oxide)

Poly(ethylene oxide) (PEO) was chosen for this first study on confinement because it is known to form very large spherulites in the bulk suggesting only few heterogeneous nuclei. Actually the origin of the absence of impurities from bulk PEO is not known and this deserves its own attention. Nevertheless, the effect of confinement should be very strong in this case. Furthermore, it carries a dipole moment that facilitates a study of the segmental dynamics under confinement.

The real-time crystallization and melting of bulk PEO was investigated by POM. The equilibrium melting temperature for PEO₂₄ was estimated at $T_m^0=331$ K (Table 1). Wide-angle X-ray $\theta/2\theta$ scans for bulk PEO₂₄ and of PEO₂₄ inside self-ordered AAO with pore diameters in the range from 200 to 25 nm were made at 298 K following slow cooling from the melt and annealing at ambient temperature for 1 day (Figure 40). For bulk PEO₂₄ several peaks appear at 2θ angles of 14.6, 15.0, 19.5, 23.2, 26.1, 26.7 and 32.9 degrees that correspond to the (021), (110), (120), (032), (024), (131) and (114) reflections from a monoclinic unit cell with interplanar spacing, d_{hkl} , of the (hkl) reflection planes given by

$$\frac{1}{d_{hkl}^2} = \frac{1}{\sin^2\beta} \left(\frac{h^2}{a^2} + \frac{k^2 \sin^2\beta}{b^2} + \frac{l^2}{c^2} - \frac{2hlc\cos\beta}{ac} \right) \quad (3.1)$$

In the above equation, $a=0.81$ nm, $b=1.30$ nm, $c=1.95$ nm and $\beta=125.4^\circ$ are the unit cell parameters. The unit cell consists of four helical chains each composed from seven monomeric units incorporated in two turns, *i.e.*, a 7/2 helix [102]. For PEO₂₄ inside AAO, the (120) reflection remains as the most prominent feature down to the 25 nm pore size, suggesting that polymer crystallization persists upon confinement. In the scattering geometry, with the AAO surface oriented perpendicularly and the AAO nanopore axes oriented parallel to the scattering plane, only sets of lattice planes oriented normal to the AAO pore axes and parallel to the AAO surface contribute to the scattered intensity. In PEO, the (120) direction is parallel to the extended chain direction and is known as the fastest growth direction of the crystalline structure. From this we can infer that the (120) direction coincides with the pore axis. Thus WAXS provided a clear evidence of oriented lamellar crystal under confinement.

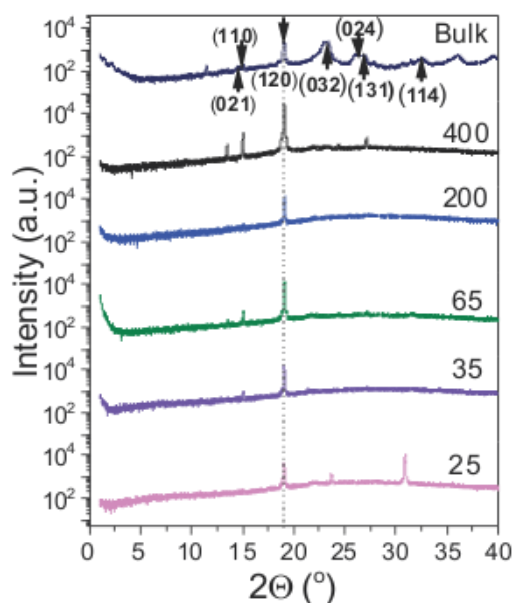


Figure 40. $\theta/2\theta$ X-ray scans for bulk PEO₂₄ and for PEO₂₄ located inside self-ordered AAO with pore diameter ranging from 400 to 25 nm with the template surface oriented perpendicularly to the plane of the incident and scattered X-ray beam at 298 K following 1 day annealing. The main diffraction peaks of bulk and confined PEO are indicated.

“Transition” from heterogeneous to homogeneous nucleation

Figure 41 shows DSC traces of bulk PEO₂₄ and PEO₂₄ located inside AAO with different pore diameters measured with a heating/cooling rate of 10 K/min. On cooling, bulk PEO₂₄ shows a strong exothermic crystallization peak at 25.8 °C. In the cooling trace of PEO-infiltrated within AAO with a pore diameter of 200 nm, the main exothermic peak is shifted by 55 K to a significantly lower temperature of -29 °C. The smaller the AAO pore diameter is, the lower are the temperatures to which the exothermic crystallization peak is shifted. The exothermic crystallization peak of PEO located in AAO with a pore diameter of 25 nm appears at a temperature as low as -38.8 °C. Hence, in AAO crystallization of PEO occurs at pronounced supercooling ΔT (ΔT is the difference between the apparent melting temperature T'_m and apparent crystallization temperature T'_c : $\Delta T = T'_m - T'_c$).

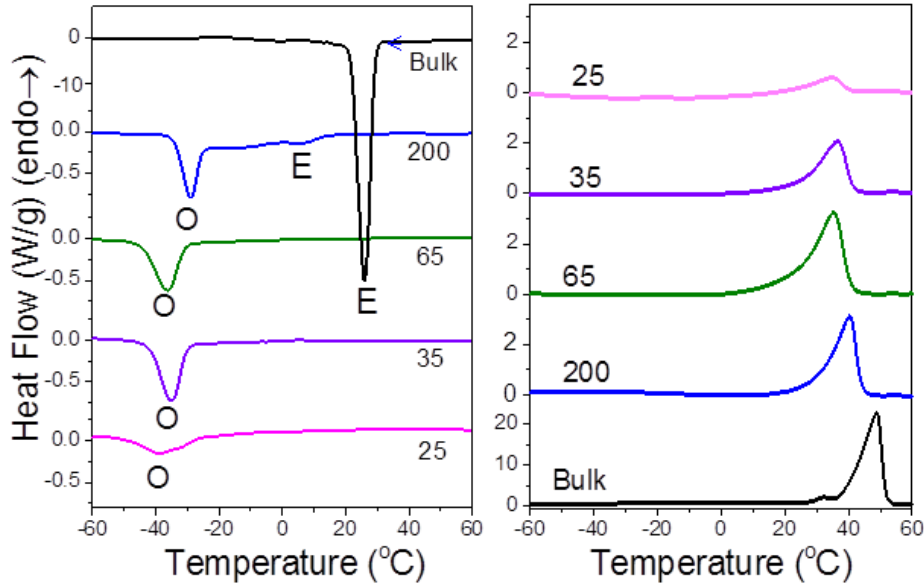


Figure 41. Cooling (left) and subsequent heating (right) thermograms of bulk PEO₂₄ and of PEO₂₄ located inside AAO with pore diameters ranging from 200 nm to 25 nm. Heating and cooling rates were 10 K/min. The letters E and O denote crystallization peaks originating from heterogeneous and homogeneous nucleation, respectively.

This outcome can be rationalized by comparing the AAO pore volume with the volume per nucleus in bulk PEO. Heterogeneous nucleation typically occurs at low supercooling because the formation of nuclei is catalyzed by impurities. If no heterogeneous nuclei are present, homogeneous nucleation initiates crystallization at larger supercooling, that is, at lower crystallization temperatures where the critical size of homogeneous nuclei is sufficiently small. Bulk PEO crystallizes via *heterogeneous nucleation*. A typical PEO spherulite has a diameter of $\sim 300 \mu\text{m}$. The resulting volume per impurity per nucleus is $\sim 10^{-2} \text{mm}^3$. Within AAO, the PEO is located in discrete cylindrical pores. Therefore, crystallization has to be initiated separately in each AAO pore. However, the volumes of 100 μm deep AAO pores amount to $\sim 10^{-8} \text{mm}^3$ for a pore diameter of 400 nm, to $\sim 3 \times 10^{-9} \text{mm}^3$ for a pore diameter of 200 nm and to $\sim 3 \times 10^{-10} \text{mm}^3$ for a pore diameter of 65 nm. Since these pore volumes are many orders of magnitude smaller than the volume per heterogeneous nucleus in bulk PEO, only a small portion of the AAO pores contains heterogeneous nuclei. These heterogeneous nuclei will initiate crystallization at low supercooling. Hence, crystallization of only a negligible volume fraction of the PEO inside AAO, namely of the PEO located in pores containing heterogeneous nuclei, will be initiated by heterogeneous nucleation at low supercooling. PEO in AAO with a pore diameter of 200 nm exhibits, in contrast to smaller pores, an additional weak exothermic peak at $+5.3 \text{ }^\circ\text{C}$. We ascribe this crystallization peak to

crystallization in the small fraction of AAO pores containing heterogeneous nuclei.

The vast majority of AAO pores are free from impurities, thus crystallization of PEO can only be initiated by *homogeneous* nucleation at high supercooling. Thus, the exothermic low-temperature peaks in the cooling runs of PEO confined to AAO represent crystallization initiated by homogeneous nucleation at high supercooling (in Figure 41, O denotes crystallization initiated by homogeneous nucleation, E crystallization initiated by heterogeneous nucleation). As obvious from the subsequent heating runs, the melting temperatures of PEO confined to AAO are significantly lower than that bulk PEO. This reflects the smaller lamella thickness of PEO crystals formed inside AAO related to the lower crystallization temperatures. Strikingly, crystallization of PEO located in AAO is drastically different from crystallization of iPP located in the same type of AAO membranes. In the latter case, the volume per nucleus of $\sim 5 \times 10^{-7} \text{ mm}^3$ is much smaller and was comparable to the pore volume for the larger AAO pores. Owing to the higher concentration of nuclei, most of the larger pores contained impurities that initiated crystal growth via heterogeneous nucleation at low supercooling.

Cooling speed dependence on nucleation mechanism

The effect of cooling rate dependence on the type of nucleation under confinement has not been studied earlier. Nevertheless, it proved to be of key importance. Figure 42 displays the DSC traces of PEO₂₄ located inside AAO with pore diameters of 200 and 65 nm measured at different cooling rates. The cooling rate dependence is pronounced for the 200 nm pores and smaller for the 65 nm pores. PEO₂₄ located inside 200 nm pores exhibits a transformation from predominantly homogeneous nucleation to predominantly heterogeneous nucleation when cooling rates are reduced from 10 K/min to 1 K/min. At intermediate cooling rates, both types of nucleation events take place. In contrast, for PEO₂₄ located inside AAO with a pore diameter of 65 nm nucleation is always homogeneous, independent of the cooling rate. Nucleation of PEO₂₄ within the 65 nm pores is representative of the nucleation processes within the 35 and 25 nm pores. As soon as homogeneous nucleation is the sole process at all cooling rates for a given AAO pore diameter, it will also be homogeneous for all smaller pore diameters. Heterogeneous nucleation in larger pores, on the other hand, can be amplified at the expense of homogeneous nucleation under conditions of slow cooling or annealing at higher temperatures where heterogeneous nucleation prevails.

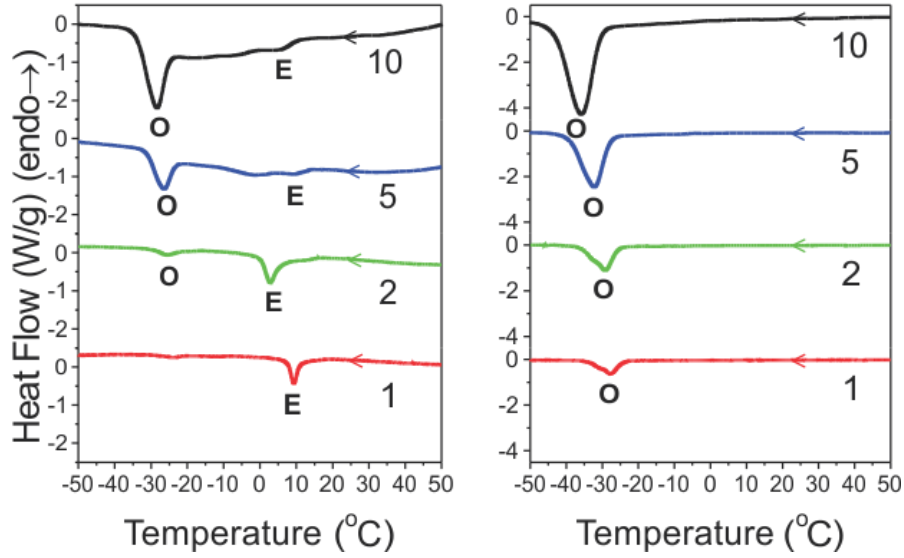


Figure 42. DSC thermograms of PEO₂₄ located inside self-ordered AAO with pore diameters of 200 nm (left) and 65 nm (right) obtained at different cooling rates. The letters E and O denote crystallization initiated by heterogeneous and homogeneous nucleation, respectively.

Pore diameter dependence on crystallization and melting temperatures

The crystallization and apparent melting temperatures of PEO₂₄ obtained from calorimetry as a function of pore diameter are illustrated in Figure 43. They both depend on the pore diameter. As mentioned earlier, the dependence of melting temperature on inverse pore diameter follows the Gibbs-Thomson equation. Since the Gibbs-Thomson equation predicts a linear dependence of the transition temperature to the inverse pore diameter, both melting and cooling temperatures were fitted with a linear function according to

$$T'_m = -\frac{198}{d} + 41.4 \quad (3.2)$$

$$T'_c = -\frac{204}{d} + (-30.4), (T \text{ in } ^\circ\text{C}), (d \text{ in nm}) \quad (3.3)$$

where d is the pore diameter. Assuming this linear dependence, equation 3.2 enables an estimation of the homogeneous nucleation temperature in the limit of $d \rightarrow \infty$.

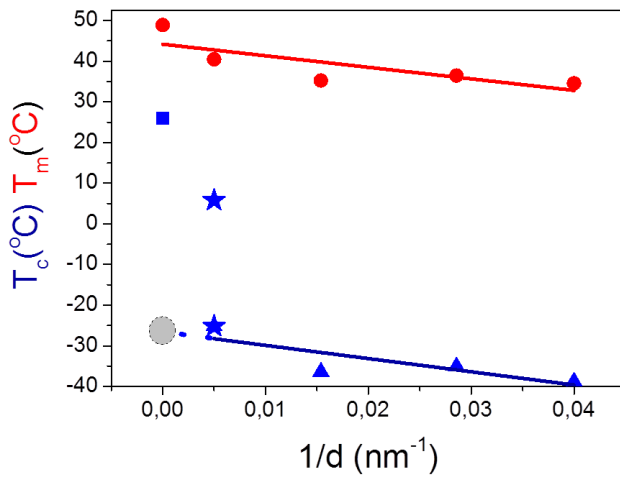


Figure 43. Apparent melting (red symbols) and crystallization (blue symbols) temperatures of PEO₂₄ inside AAO as a function of inverse pore diameter obtained at a heating/cooling rate of 10 Kmin⁻¹. The solid lines are linear fits to the melting/crystallization temperatures of PEO₂₄. The gray dot is the temperature of homogeneous nucleation of bulk PEO₂₄.

Molecular weight dependence of the homogeneous nucleation temperature and its relation to the liquid-to-glass temperature

Figure 44 shows the dependence of the apparent crystallization temperatures at which crystallization initiated by *homogeneous* nucleation extrapolated to $d \rightarrow \infty$ (d = pore diameter) on the PEO molecular weight. For comparison, the crystallization temperatures of PEO in droplets with sizes of $\sim 10 \mu\text{m}$ cooled from the melt at 0.4 K/min [27] and of high molecular weight PEO crystallized under finite dimensions ($d=400 \text{ nm}$) [40] are also included.

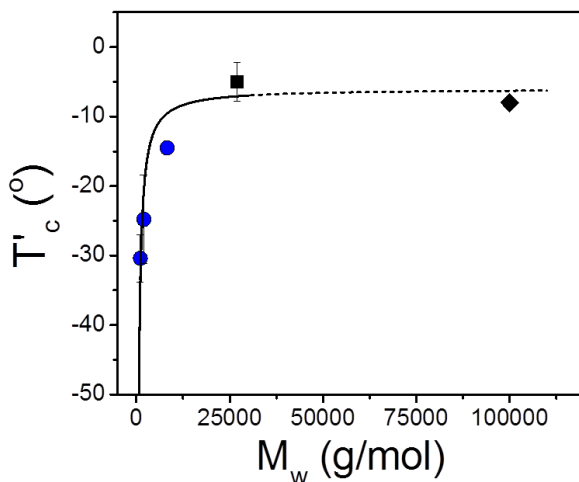


Figure 44. Dependence of the crystallization temperature T'_c of crystallization processes initiated by homogeneous nucleation at high supercooling on the molecular weight of PEO in the limit $d \rightarrow \infty$ (d = AAO pore diameter). Spheres: T'_c obtained by extrapolation of the $T'_c(d)$ profiles seen in Figure 43 to infinite pore diameters. The $T'_c(d)$ profiles were obtained from DSC scans of PEO inside AAO at a cooling rate of 10 Kmin⁻¹. Squares: PEO crystallized at a cooling rate of 0.4 K/min in droplets of $\sim 10 \mu\text{m}$ size prepared by dewetting of a PEO film [27]. The solid line is a fit to the experimental data. In the same plot we include literature data [40] (rhombus) of PEO crystallization under finite diameters ($d = 400 \text{ nm}$) at a cooling rate of 20 Kmin⁻¹.

The obtained results conform to

$$T'_c = T_c^\infty - \frac{A}{M_w} \quad (3.4)$$

where $T_c^\infty = -6$ °C is the apparent crystallization temperature if crystallization is initiated by homogeneous nucleation in the limit of very high molecular weights and $A = 29200$ K·g/mol is a fitting parameter. The strong molecular weight dependence of T'_c for the lower molecular weights is reminiscent of the dependence of the liquid-to-glass temperature $T_g(M_w)$, represented by the Fox-Flory equation. This suggests that molecular weight affects the mobility/diffusion term ($B/T-T_0$, where B is the activation parameter and T_0 the “ideal” glass temperature located below T_g) entering the equation for the nucleation rate (equation 1.14). Hence, a strong effect is expected for the lower molecular weights as observed experimentally.

Effect of oligomer on homogeneous nucleation temperature

In order to support the hypothesis presented in the previous section (correlation between liquid-to-glass temperature and homogeneous nucleation temperature), the effect of an oligomer on the homogeneous nucleation temperature was investigated. If the liquid-to-glass and homogeneous nucleation temperatures are coupled, then a shift of the former should produce a concomitant shift in the latter. It is well-known that oligomers impart mobility and as a result lower the liquid-to-glass temperature. Figure 45 shows DSC curves of PEO₄₆ in the absence and presence of 20 wt% of oligomer (PEO₃). A clear shift of the homogeneous nucleation temperature was observed. On average, 5 °C lowering of homogeneous nucleation temperatures due to the addition of oligomer were observed (Figure 46). This experiment revealed that it is possible to control the homogeneous nucleation temperature by adding small amounts of an oligomer. Thus, this experiment strongly supports the proposed correlation between homogeneous nucleation temperature and liquid-to-glass temperature.

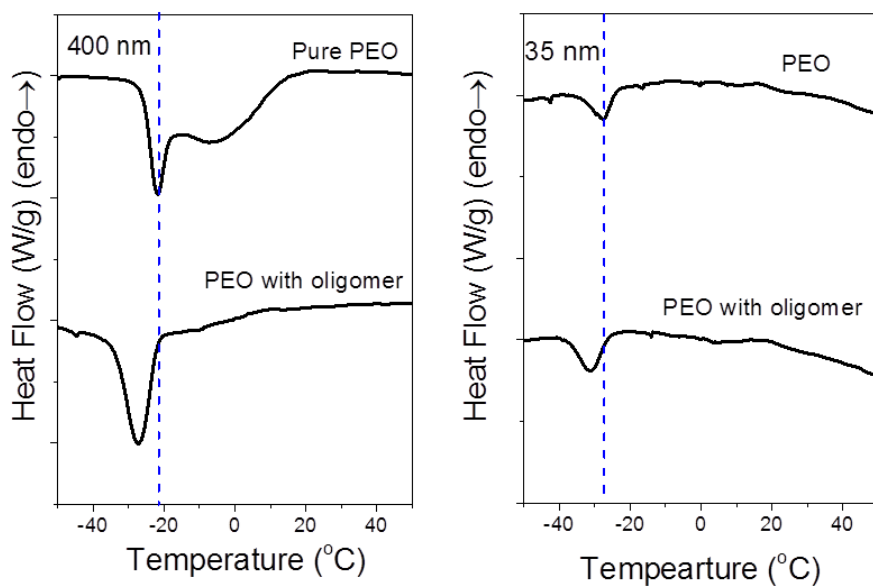


Figure 45. The comparison of DSC thermograms of PEO₄₆ located inside AAO in the absence and presence of oligomer (PEO₃) with pore diameters of 400 nm (left) and 35 nm (right). The cooling speed was 10 K/min.

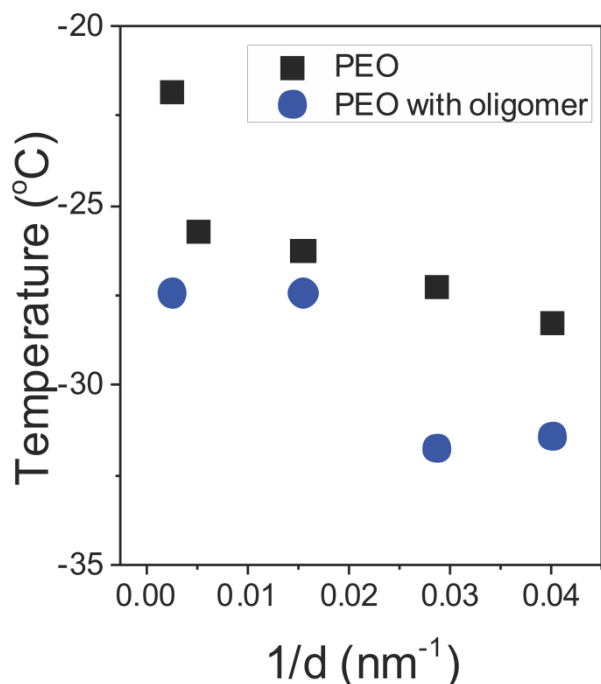


Figure 46. Homogeneous nucleation temperatures of pure PEO₄₆ (black square) and PEO₄₆ in the presence of oligomer (blue circle) located inside AAO as a function of inverse pore diameters. On average, -5 °C shift of homogeneous nucleation temperatures was observed.

3.2. Crystallization of Poly(ϵ -caprolactone)

Motivation of this study

Poly(ϵ -caprolactone) (PCL) is a polymer that is chemically similar to PEO. It has a similar glass temperature and a similar melting temperature. Yet, it crystallizes in a different unit cell

(PEO: monoclinic, PCL: orthorhombic). But a more importance differences in the context of the present study is that it forms much smaller spherulites in the bulk (size $\sim 30 \mu\text{m}$) as compared to PEO. We have argued that the spherulitic size and hence the number of heterogeneous nuclei is a decisive parameter that controls the nucleation mechanism. Hence, this system can be useful to better understand the origin of heterogeneous nucleation. Upon confinement of PCL to AAO, heterogeneous nucleation in addition to homogeneous nucleus is to be expected.

Multiple nucleation processes under confinement

DSC traces on cooling and subsequent heating were shown to contain important information on the type of nucleation processes. Figure 47 shows the DSC traces of bulk PCL₆₈ and of PCL₆₈ located inside AAO obtained with a cooling rate of 10 K/min. Bulk PCL₆₈ shows a strong exothermic peak at 32 °C. All traces of PCL₆₈ located inside AAO contain a shallow peak at about 34 °C. Depending on the pore size, traces exhibit significant differences. PCL₆₈ located inside AAO with a pore diameter of 200 nm exhibits two exothermic peaks at 21 °C and at 6 °C. On the other hand, PCL in pores with a diameter of 25 nm exhibits a broad exothermic peak at -35 °C. PCL in 35 nm pores exhibits a similar exothermic processes at -34 °C but has some additional – albeit weak- exothermic processes at 20 °C and 6 °C. PCL in 65 nm pores contains some intermediate features. The DSC traces of PCL₃₁₆ inside the same templates revealed similar features.

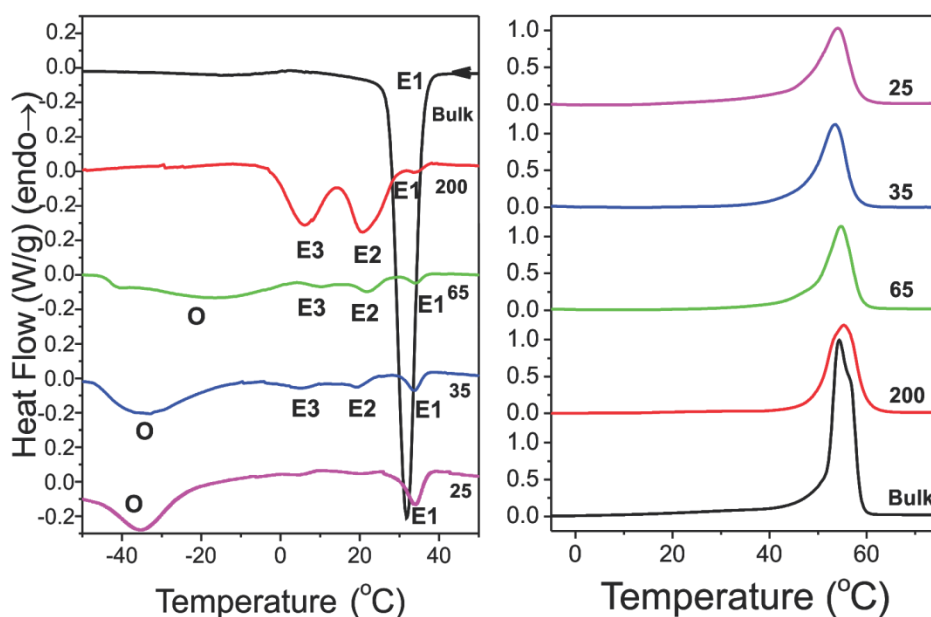


Figure 47. Cooling (left) and subsequent heating (right) thermograms of bulk PCL₆₈ located inside AAO with pore diameters ranging from 200 nm to 25 nm (heating/cooling rate 10 Kmin⁻¹.) The letters E and O denote crystallization peaks originating from heterogeneous and homogeneous nucleation, respectively.

The multiple peaks of PCL₆₈ located inside AAO with a pore diameters of 200 nm at 34, 21 and 6 °C are attributed to heterogeneous nucleation and indicate them as E1, E2 and E3, respectively. Heterogeneous crystallization is the sole mechanism for PCL located inside AAO with 200 nm pores but is a minor crystallization mechanism in the smaller pores. The former constitutes a large difference from the PEO case whereas the latter is similar to PEO. For PCL located inside AAO with pore diameters below 65 nm, the main peaks appear at lower temperatures, *i.e.*, at higher undercooling. From the study of PEO, it was clearly shown that homogeneous nucleation prevails for temperatures in the vicinity of liquid-to-glass temperature. Hence, these peaks for PCL at -35 °C are attributed to homogeneous nucleation. The critical nucleus size for homogeneous nucleation, l^* , is given by $l^* = 4\sigma_e T_m^0 / \Delta T \Delta H_m \rho_c$, where σ_e (106 mJ m⁻²) is the fold surface free energy, $T_m^0 = 348$ K the equilibrium melting temperature, $\Delta H_m = 148$ J g⁻¹ the latent heat of fusion at the equilibrium melting temperature, $\Delta T = T_m^0 - T_c$ the undercooling and $\rho_c = 1.187$ g cm⁻³ the crystal density. ΔT is 43 K in bulk PCL₆₈ but it increases to 110 K for PCL inside AAO with pore sizes of 35 nm and 25 nm. At such undercoolings in the smaller pores, the critical nucleus size for homogeneous PCL nucleation is about 8 nm and is, therefore, smaller than the diameter of the smallest pores. Thus, PCL (like PEO) is able to crystallize even within 25 nm pores.

The cooling rate dependence of the transition temperatures is indicated in Figure 48 for PCL₆₈ inside AAO with two pore sizes and displays some unanticipated features. In general, reducing the scan speed results in higher crystallization temperatures both for heterogeneous and homogeneous nucleation in agreement with the earlier study on PEO/AAO. Within the 200 nm pores, PCL nucleation events are solely heterogeneous and the crystallization temperatures display strong rate dependence. In addition, under the quasi-static conditions corresponding to the lower rates (1 and 2 K/min), there is a splitting of the peaks suggesting a complex heterogeneous nucleation scenario. On the other hand, within the 35 nm pores nucleation is predominantly (but not solely) homogeneous. In addition to the minor heterogeneous nucleation processes at low undercoolings (processes E1, E2 and E3) the homogeneous nucleation process becomes very asymmetric and can be decomposed into at least two distinct processes (both indicated as O). One possible explanation of this phenomenon is the effect of another kind of heterogeneity at the vicinity of T_g ; namely, spatial and temporal heterogeneity of the dynamics [103]. Nevertheless, the meaning of the dual processes associated with homogeneous nucleation is unclear at present.

On heating (Figure 47) bulk PCL melts at ~328 K as compared to the equilibrium melting temperature (at 348 K). Such a reduction suggests finite size effects as described by the Gibbs-Thomson equation:

$$T_m' = T_m^o \left[1 - \frac{2}{\Delta H_m^o \rho_c} \left(\frac{\sigma_1}{l_1} + \frac{\sigma_2}{l_2} + \frac{\sigma_e}{l_3} \right) \right] \quad (3.5)$$

where σ_1 and σ_2 are the lateral surface free energies, σ_e is the fold-surface free energy, l_1 , l_2 and l_3 the respective crystal dimensions, T_m' and T_m^o are the apparent and equilibrium melting temperatures, ΔH_m^o is the heat of fusion (in J/g) and ρ_c the crystal density. An estimate of the crystal size for bulk PCL can be obtained by using the following values [104–107], $\sigma_1 \sim \sigma_2 = 6$ mJ/m², $\sigma_e = 106$ mJ/m², $\Delta H_m^o = 148$ J/g, $\rho_c = 1.187$ g/cm³ and the experimentally observed apparent melting temperature (327.6 K). Further assuming $\sigma_e/l_3 \gg \sigma_1/l_1 \sim \sigma_2/l_2$ gives $l_3 \sim 21$ nm. For PCL confined within self-ordered AAO pores with diameters below 65 nm we notice that the melting peak becomes very asymmetric especially towards lower temperatures. Within the smaller pores, homogeneous nucleation takes place at larger undercoolings. In this nucleation-dominated regime all crystal orientations occur and crystals grow along the pores until they are blocked by neighboring competing crystals. As a result, random crystalline orientation prevails giving rise to spherical-like crystalline stems, *i.e.* $l_1 \sim l_2 \sim l_3$. If a crystal size of ~15 nm is assumed, melting is expected to occur at ~319 K, *i.e.*, some 9 K below the bulk sample as observed experimentally.

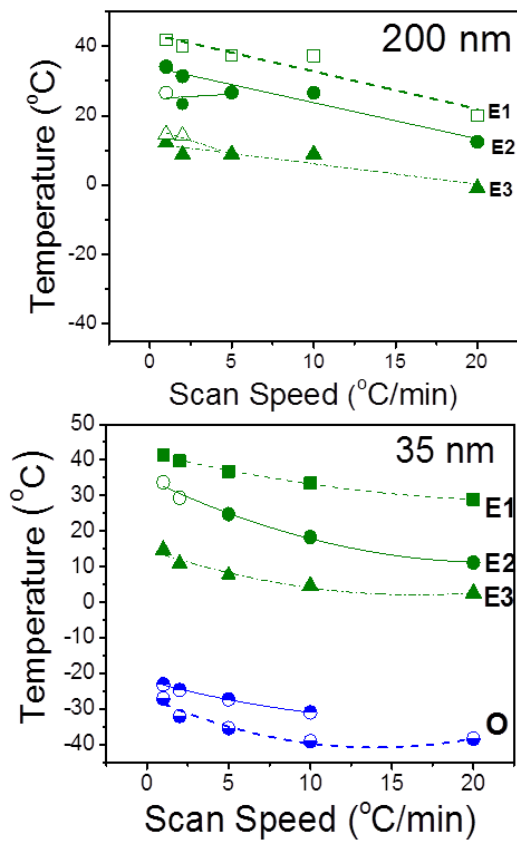


Figure 48. Transition temperatures for PCL₆₈ located inside AAO with pore diameters of 200 nm (top) and 35 nm (bottom) obtained on cooling with different rates (in Kmin⁻¹) as indicated. The letters E and O stand for crystallization initiated by heterogeneous and homogeneous nuclei, respectively. Lines are guides to the eye.

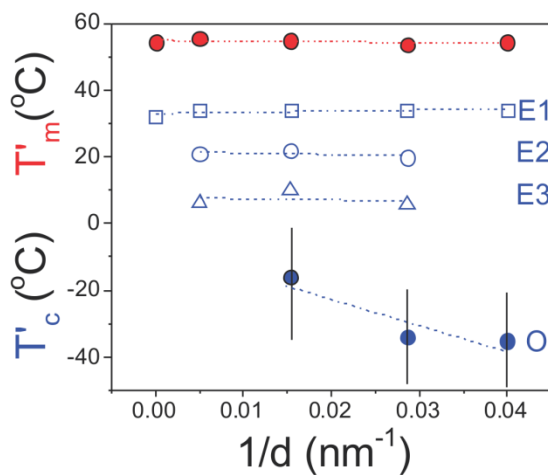


Figure 49. Apparent melting (red symbols) and crystallization (blue symbols) temperatures of PCL₆₈ inside self-ordered AAO as a function of inverse pore diameter (obtained at a heating/cooling rate of 10 K/min). The dashed lines represent linear fits. The vertical lines are not error bars but give the temperature range for the homogeneous nucleation process.

The corresponding apparent melting and crystallization temperatures for the same PCL inside AAO are plotted in Figure 49. The figure displays the single – albeit broad – melting temperature and the multiple nucleation processes (heterogeneous E1, E2, E3, and homogeneous O) obtained on cooling with a rate of 10 K/min.

Origin of multiple nucleation events for PCL

More insight into the origin of the different nucleation processes can be obtained by the surface modification of pore walls with ODPA. The DSC traces for PCL₆₈ inside surface-treated AAO are summarized in Figure 50.

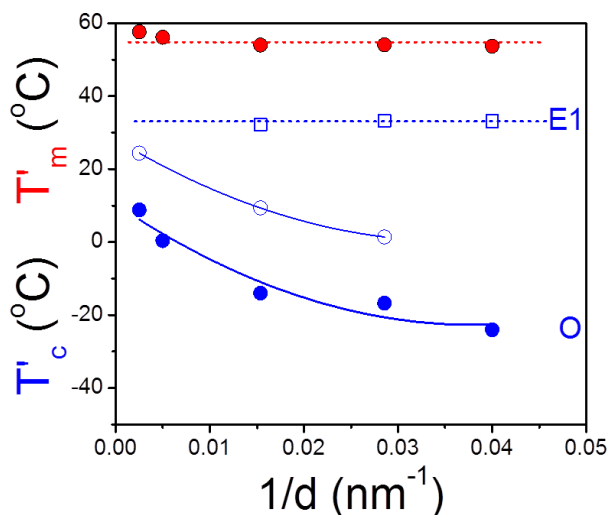


Figure 50. Apparent melting (red symbols) and crystallization (blue symbols) temperatures of PCL₆₈ inside surface-treated with ODPA self-ordered AAO as a function of inverse pore diameter obtained at a heating/cooling rate of 10 K/min.

The main effect of surface modification is the suppression of the E2 and E3 heterogeneous nucleation mechanisms. This suggests that the latter two mechanisms are induced by the AAO surface. On the other hand, a new nucleation process appears at temperatures between E1 and O. This intermediate process could reflect nucleation initiated by the grafted ODPA alkyl chains, but its characterization requires further investigation.

Effect of confinement on the degree of crystallinity and crystal orientation

The degree of crystallinity and crystal orientation determines the mechanical and optical properties of materials. The degree of crystallinity was extracted from the heat of fusion (DSC) and the crystal orientation was studied by WAXS and AFM. The heats of fusion, ΔH_m , and corresponding degrees of crystallinity, X_c , are plotted in Figure 51 as a function of inverse pore diameter. The overall degree of crystallinity is reduced upon confinement to about half of the bulk value (from 80% to 35%). This is independent of the fact that within the larger (smaller) pores crystallization is initiated via heterogeneous (homogeneous) nucleation. This reflects the lateral restriction on the crystal growth by the pore walls that can lead to structural defects.

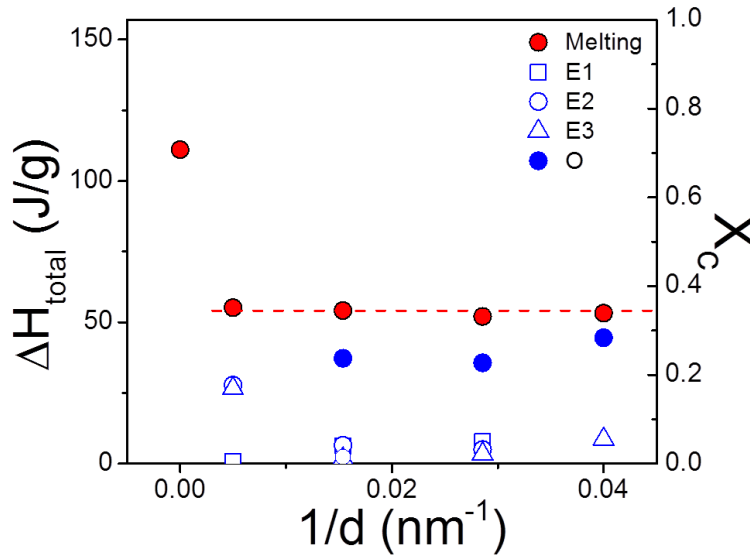


Figure 51. (Left axis) Heat of fusion of PCL₆₈ plotted as a function of inverse pore diameter obtained on cooling (blue symbols) and subsequent heating (red circles). (Right axis) Degree of crystallinity as a function of inverse pore diameter.

Figure 52 displays WAXS measurements of bulk PCL and PCL confined to AAO. For bulk PCL, intense peaks appear at 2θ angles of 15.5° , 21.3° , 21.9° , 23.6° , 29.7° , 30.1° , and 36.1° . These correspond to the (102), (110), (111), (200), (210), (211) and (020) reflections from the orthorhombic unit cell with interplanar spacings d_{hkl} of the (hkl) lattice planes given by

$$\frac{1}{d_{hkl}^2} = \frac{h^2}{a^2} + \frac{k^2}{b^2} + \frac{l^2}{c^2} \quad (3.6)$$

The unit cell parameters are $a = 0.749$ nm, $b = 0.497$ nm, and $c = 1.729$ nm. This unit cell has been discussed as comprising an extended planar chain conformation of the molecule involving two monomer residues related by a two-fold screw axis in the chain direction. Furthermore, the space group ($P2_12_12_1$) and density 1.146 g/cm³ indicated that the unit cell comprises two chains with opposite orientation, *i.e.*, up and down. Interestingly, an earlier electron diffraction study of solution-grown PCL crystals indicated that the fastest crystal growth occurs normal to the {110} and {200} faces. Similarly, a real-time crystallization of PCL from the melt by atomic force microscopy also suggested a mechanism involving {110} growth faces. Therefore, in bulk PCL, crystallization proceeds along directions normal to the {110} and {100} faces.

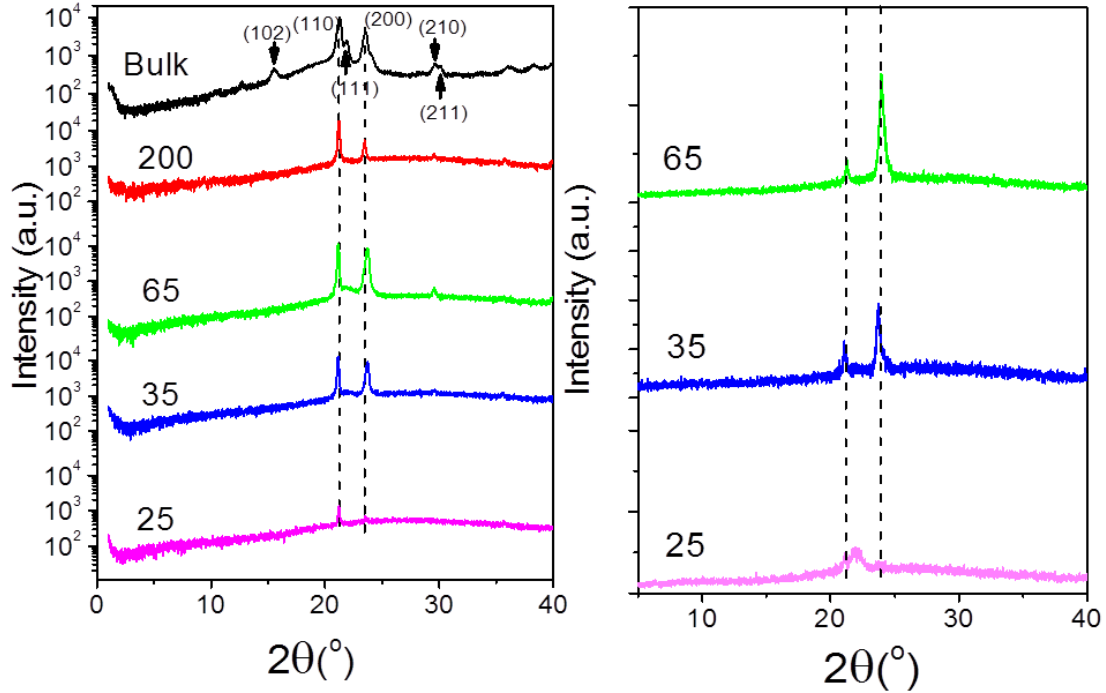


Figure 52. $\theta/2\theta$ X-ray scans for bulk PCL and PCL located inside AAO with pore diameters ranging from 200 to 25 nm. (Left) Measurements are conducted at 298 K following slow cooling from the melt (363 K) and 1 day annealing. (Right) Measurements are conducted at 243 K following fast cooling from 363 K. In both cases, the template surface was oriented perpendicularly to the plane of the incident and scattered X-ray beams (described in chapter 2). The main diffraction peaks of bulk and confined PCL are indicated with vertical lines.

Subsequently, the PCL crystal orientation inside self-ordered AAO was studied either by slow cooling from the melt (3 Kmin^{-1}) following annealing at 298 K, or by fast cooling to 243 K (at -50 Kmin^{-1}). As discussed earlier, this thermal treatment emphasizes different nucleation mechanisms (*homogeneous* vs. *heterogeneous*). For PCL in AAO following the former treatment most of the bulk reflections are suppressed with the exception of the (100) and (200) reflections. This suggests preferred orientation of the $\{110\}$ and $\{200\}$ faces normal to the AAO pore axes. To further investigate the crystal orientation of PCL in AAO, we measured Schulz scans and presented in Figure 53. Schulz scans were measured with fixed θ and 2θ angles by tilting the AAO about the Ψ axis by a tilt angle Ψ . The Ψ axis lies in the scattering plane (normal to the AAO pore axes) and was oriented perpendicular to the $\theta/2\theta$ axis. The Schulz scans yielded intensity profiles $I(\Psi)$ representing orientation distributions of sets of lattice planes belonging to the reflection at the selected 2θ angles relative to the AAO surface. Hence, the obtained $I(\Psi)$ profiles corresponded to azimuthal intensity profiles along the Debye ring belonging to the fixed scattering angle θ . The Schulz scan for the (110) peak of PCL in AAO with a pore diameter of 65 nm crystallized at a cooling rate of -3 K/min

indicated pronounced alignment of the $\{110\}$ crystal faces with the AAO surface (corresponding to the preferred orientation of the $\{110\}$ faces perpendicular to the AAO pore axes). The Hermans orientation parameter amounted to ≈ 0.95 , suggesting a nearly uniform orientation.

On the other hand, following the latter treatment (fast cooling to 243 K) gives rise to crystal growth along the same directions. However, in the case of 65 nm or 35 nm pores, preferentially the $\{100\}$ faces appear to be oriented normal to the AAO pore axes.

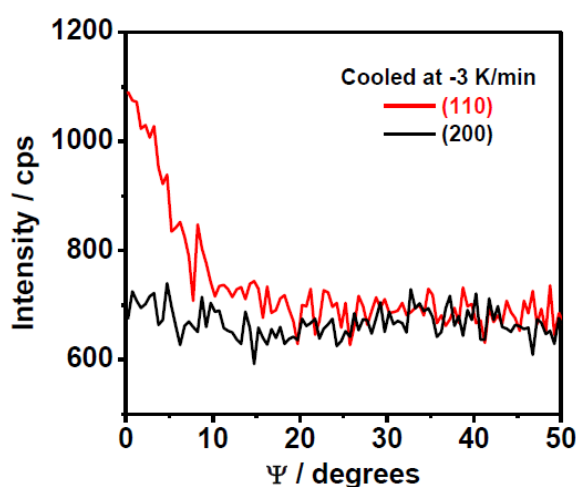


Figure 53. Schulz scan belonging to the (100) and (200) peaks of PCL in AAO with a pore diameter of 65 nm. The sample was cooled at -3 K/min from the melt. Schulz scans were measured with fixed θ and 2θ angles by tilting the AAO about the Ψ axis by a tilt angle Ψ . The Ψ axis lay in the scattering plane (normal to the AAO pore axes) and was oriented perpendicular to the $\theta/2\theta$ axis. The Schulz-Scans yielded intensity profiles $I(\Psi)$ representing orientation distributions of sets of lattice planes belonging to the reflection at the selected 2θ angles relative to the AAO surface. Hence, the obtained $I(\Psi)$ profiles corresponded to azimuthal intensity profiles along the Debye ring belonging to the fixed scattering angle θ .

Direct observation of lamellar orientation was obtained with AFM (Figure 54). After the infiltration of PCL into AAO, the sample was frozen into liquid N_2 and cut with a metal cutter. Subsequently, the sample was mounted vertically on the sample holder. AFM images were obtained with tapping mode AFM. The phase image provides a clear view of an oriented crystalline lamellar. The lamellar is parallel to the pore walls, in agreement with the X-ray data. In addition to the main crystals, there exist some smaller structures originating from the pore walls. These structures could be related to the multiple heterogeneous nucleation observed with PCL.

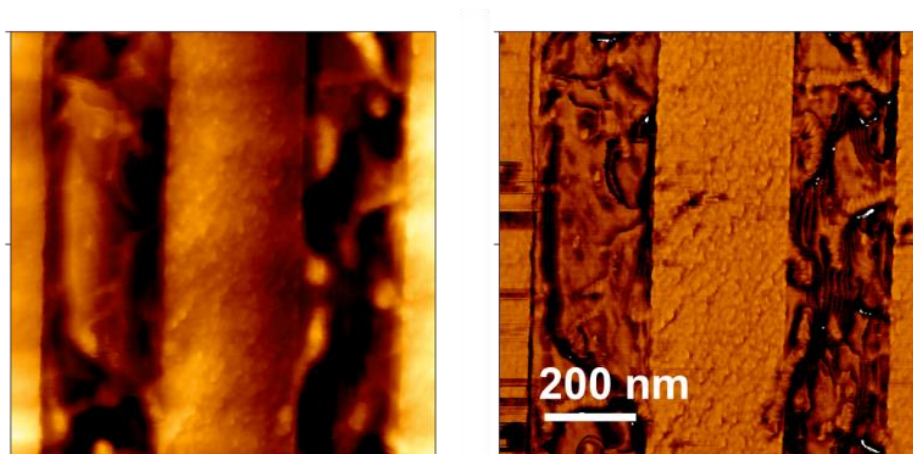


Figure 54. AFM images of PCL located inside AAO. AAO (200 nm) infiltrated with PCL was inserted into liquid N₂, and then the AAO template was cut with a metal cutter. Cross sectional images were obtained by tapping mode AFM; (Left) height image; (Right) phase image.

Dynamics under confinement

So far the effect of confinement on the crystalline segments of PCL was discussed (melting, degree of crystallinity and crystal orientation). In this section we discuss the effect of confinement on the amorphous segments and in particular the alteration of the segmental dynamics. The polymer dynamics under confinement was studied using dielectric spectroscopy. Dielectric spectroscopy probes the response of the inherent dipole moment of the material in the presence of an external electric field. The PCL repeat unit $[-(\text{CH}_2)_5\text{COO}-]$ has a dipole moment originating from the ester group (total ester dipole moment 1.72 D as obtained from dilute solutions in dioxane) with components parallel (0.64 D) and perpendicular (1.6 D) to the backbone [108]. Thus DS is capable, in principle, of following the local and global chain dynamics by recording dielectric spectra as a function of frequency at different temperatures. Nevertheless, a strong contribution from ionic conductivity and the presence of crystalline/amorphous domains and the associated Maxwell–Wagner–Sillars polarization precludes the investigation of the slower chain dynamics in the bulk state [98]. We are thus focusing our attention on the local dynamics below and above the glass temperature (T_g).

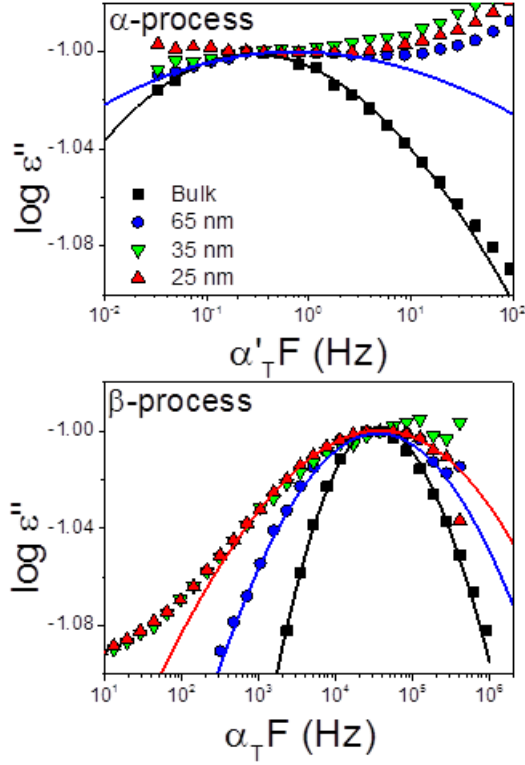


Figure 55. Normalized dielectric loss curves for the α - (top) and β -processes (bottom) for bulk PCL and PCL located inside AAO with pore diameters ranging from 65 to 25 nm obtained at $T=228$ K and $T=183$ K, respectively. Spectra have been slightly shifted horizontally with shift factors α' and α'_T respectively to better indicate the broadening of the curves.

Typical dielectric loss curves of bulk PCL are shown in Figure 55 at two temperatures corresponding to the segmental (α -process) and local (β -process). The α - and β -processes were fitted according to the HN function with respective shape parameters $m = 0.22$, $n = 0.20$ and $m = 0.43$, $n = 0.30$. The α -process conforms to the Vogel-Fulcher-Tammann (VFT) equation.

$$\tau = \tau_0 \exp\left(\frac{B}{T-T_0}\right) \quad (3.7)$$

where $\tau_0 (= 10^{-12}$ s) is the relaxation time in the limit of very high temperatures, $B (= 2300$ K) is the activation parameter and $T_0 (= 131$ K) is the “ideal” glass temperature. The conventional glass temperature is obtained from the above equation when the α -relaxation time is at 100 s. The β -process conforms to an Arrhenius equation instead,

$$\tau = \tau_0 \exp\left(\frac{E}{RT}\right) \quad (3.8)$$

with $\tau_0 = 3 \times 10^{-15}$ s and an activation energy, E , of 35 kJ/mol.

The effect of confinement on the dielectric loss spectra of PCL is also shown in Figure 56. Confinement of PCL within AAO has two effects. First, a broadening of the dynamic processes and a shift of the respective peaks to higher frequencies (faster dynamics) is observed. The latter is shown in Figure 56 where the relaxation times are plotted in the usual Arrhenius representation. The broadening of the processes and the limited frequency range available for the α -process within the smaller pores require the use of a fixed $\tau_0 = 10^{-12}$ s as with the bulk PCL₆₈. The estimated glass temperature is then reduced from 206 K in bulk PCL to 201 K within 65 and 35 nm to 190 K within 25 nm pores. Such reductions in the glass temperature are not uncommon in confined systems [109] [110].

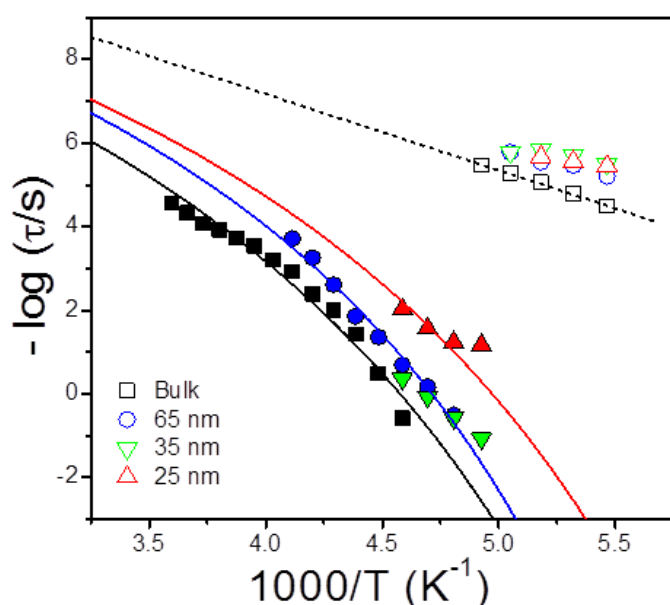


Figure 56. Relaxation times at maximum loss corresponding to bulk PCL₆₈ and to PCL₆₈ located inside AAO with pore diameters ranging from 65 nm to 25 nm. The α - and β -processes are shown by filled and empty symbols, respectively. Solid and dashed lines are fits to the VFT (α) and Arrhenius processes (β), respectively (the latter is shown only for bulk PCL).

The most dramatic effect of confinement is the broad distribution of relaxation times within the smaller pores. The latter reflects enhanced spatial and possibly temporal heterogeneity as probed by the PCL dipoles with the rates of α - and β - processes. This can be understood if we consider that both processes are probing dipoles located in the amorphous PCL segments that are spatially varying environment as seen by the ester dipoles. In addition, possible adsorption of chains near the walls can give rise to density modulations with regions of lower and higher density that can enhance the existing heterogeneities. It is surprising that confinement effects exist also for the faster and hence more local β - process. This process shifts to lower temperatures (becomes faster) and the activation energy is reduced from a bulk value to 35 kJ/mol to about 25 kJ/mol for PCL within the 65 nm pores.

In conclusion, confinement affects the dynamics in two ways. By creating a broad distribution of relaxation times and by speeding-up the segmental dynamics. In the next section we discuss the effect of confinement on the crystallization kinetics that requires input both from the crystallization and dynamics studies above.

Crystallization kinetics under confinement

The strong heterogeneous nucleation in bulk PCL and in PCL inside AAO templates with a pore size of 200 nm allows an investigation of the crystallization kinetics at rather low undercoolings. Measurements were made under isothermal conditions, following fast cooling from the melt. The DSC traces for bulk PCL and for PCL located inside AAO with 200 nm pores are depicted in Figure 57. The analysis of the traces is based on the Avrami equation for the volume fraction of the newly formed phase:

$$V_c(t) = 1 - \exp(-kt^n) \quad (3.9)$$

where k is the rate constant and n is the Avrami exponent that is associated with the dimensionality of the growing crystals and the time-dependence of nucleation. This equation requires the volumetric fraction of the crystalline phase that is obtained as

$$V_c = \frac{w(t)}{\left[w(t) + \left(\frac{\rho_c}{\rho_a} \right) (1 - w(t)) \right]} \quad (3.10)$$

Here, ρ_c and ρ_a ($=1.094 \text{ g cm}^{-3}$) are the densities of crystalline and amorphous PCL, respectively. The half-time of crystallization is obtained as, $t_{1/2} = (\ln 2/k)^{1/n}$, and is plotted in Figure 58. As expected from the low undercooling, the lower the crystallization temperature the faster the kinetics of crystal growth is. Confinement slows down the crystallization times and results in a lower Avrami exponent relative to the bulk (from a bulk value in the range $n = 3.5 - 5$ to $n \sim 3$ under confinement). Such values are in accordance with the heterogeneous nucleation probed at low undercoolings and distinctly different from the first-order kinetics observed in PCL-*b*-PS [111] and PCL-*b*-poly (4-vinylpyridine) [112] copolymers at higher undercoolings associated with homogeneous nucleation.

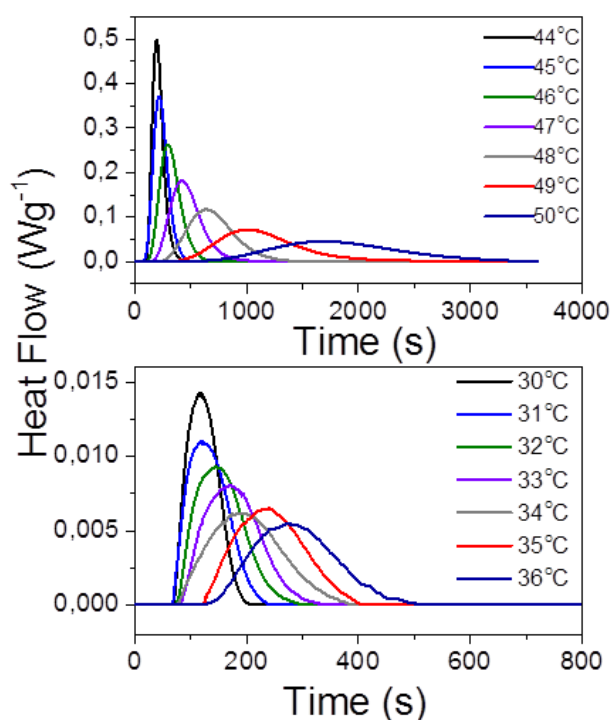


Figure 57. Heat flow during the isothermal crystallization of bulk PCL (top) and PCL₆₈ located inside AAO templates with a pore diameter of 200 nm (bottom) at different crystallization temperatures indicated.

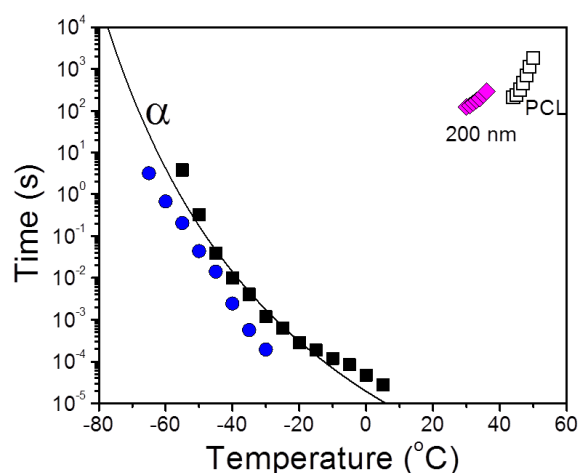


Figure 58. Characteristic crystallization times, $t_{1/2}$ (open symbols), obtained from the kinetics for bulk PCL (open squares) and for PCL located in AAO templates with a size of 200 nm (open rhombi). These kinetic times are compared with the α -process relaxation times of bulk PCL (filled squares) and of PCL in templates with a size of 65 nm (spheres). The line shows the VFT process for bulk PCL.

In the same figure we include the characteristic times of the segmental α -process for bulk PCL and for PCL in AAO with 65 nm pore size. Within this temperature range (*i.e.*, for temperatures in the vicinity of the glass temperature), the kinetics are expected to be dominated by segmental or chain transport (*i.e.*, diffusion-controlled) and hence become slower by decreasing temperature. A recent study with fast differential scanning calorimetry [15] indicated that an even faster time scale and a more local viscosity might be appropriate within the homogeneous nucleation regime. Nevertheless, the low heats of fusion and much higher undercooling preclude an investigation of the kinetics due to homogeneous

nucleation with our experimental set-up (such experiments are plausible by ultra-fast calorimetry [15]).

Inevitably, homogeneous nucleation is strongly coupled to the local viscosity at large undercoolings and possibly to the local segmental dynamics associated with the (supercooled) liquid-to-glass temperature. Confinement affects both the rates of segmental motion (with a lowering of the glass temperature) as well as the distribution of relaxation times (broader distribution). Further experiments on different polymers with slow crystallization kinetics are necessary as they can bring about the larger picture of how, why and when polymers crystallize under confinement.

3.3. Origin of heterogeneous nuclei: effects of additives, polydispersity and of a free top layer

As described in the introduction section, it is widely accepted that heterogeneous nucleation can be initiated by different sources: for example, by external surfaces (like dust or bubbles), by additives (such as remaining catalyst, solvent, other chemicals, polymer tacticity and chain poly dispersity), external nucleating agents (like graphite, carbon black, titanium oxide) and rough container surfaces, interfaces and possibly interphases [113]. However, very little is known on the precise origin of heterogeneous nucleation. In contrast to this some theoretical studies tried to better understand the mechanism of homogeneous nucleation [114].

In the previous chapters, it has been shown that heterogeneous nucleation is completely suppressed upon confinement to AAO with diameters below 65 nm. This implies that most impurities are excluded from the pores. This size exclusion effect potentially opens a new way of understanding the origin of heterogeneous nucleation. With the aim to better understand the origin of heterogeneous nucleation, we investigate (a) the effect of additives (b) of a free surface layer and (c) of chain polydispersity on nucleation of polymers under confinement.

At first, the effect of a top layer on PEO crystallization was investigated. Intentionally, the surface of AAO was not perfectly cleaned leaving a layer of PEO on top of the template. Crystallization in presence of a top layer is fundamentally different. Now all pores “communicate” through the top layer and a single nucleation event can eventually “crystallize” all pores. Obviously, this experiment enhances heterogeneous nucleation at the expense of homogeneous nucleation. The choice of PEO here is clear: Because of the large spherulites in bulk PEO and the small number of heterogeneous nuclei, a stronger effect is expected with a shift from homogeneous to heterogeneous nucleation.

Prior to the DSC experiment, the template with a top layer of PEO₄₆ was investigated with AFM. Typically, the film thickness was around 500 nm. As an example, an AFM phase image on top of AAO is shown in Figure 59. Spiral PEO structures due to self-assembly in a thin film are observed.

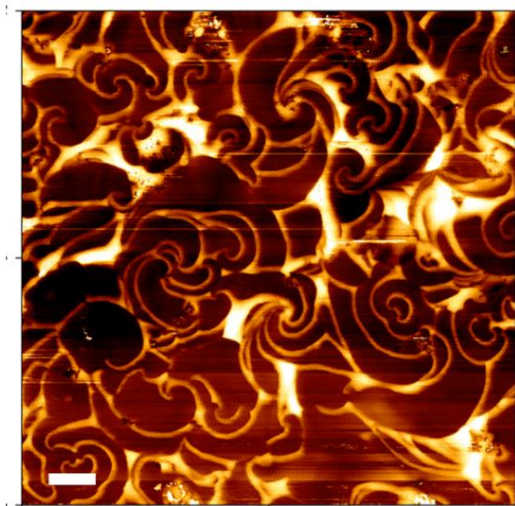


Figure 59. AFM phase image of PEO₄₆ on top of AAO template. The white scale bar corresponds to 1 μm . The color scale of image describes from 0 degree of black to 35 degree of white.

Figure 60 depicts DSC traces of bulk PEO₄₆ and of PEO₄₆ located inside AAO with different pore diameters in the presence of surface layer. Measurements were made on heating and subsequent cooling with a rate of 10 K/min. Unlike the previously discussed PEO with respect to Figure 41, the present system shows clear heterogeneous peaks even for the small pores (65 nm and 35 nm). In addition, at least two heterogeneous nucleation peaks were observed from PEO₄₆ confined to AAO with diameters below 200 nm. The stronger peak is slightly shifted to lower temperature than the bulk heterogeneous nucleation temperature. The weaker peak is intermediate to the main heterogeneous and homogeneous nucleation temperature and depends on pore diameter. Furthermore, the melting process provides additional information. Upon confinement, a clear broadening of melting peak was observed. This implies a broader distribution of lamellar thicknesses

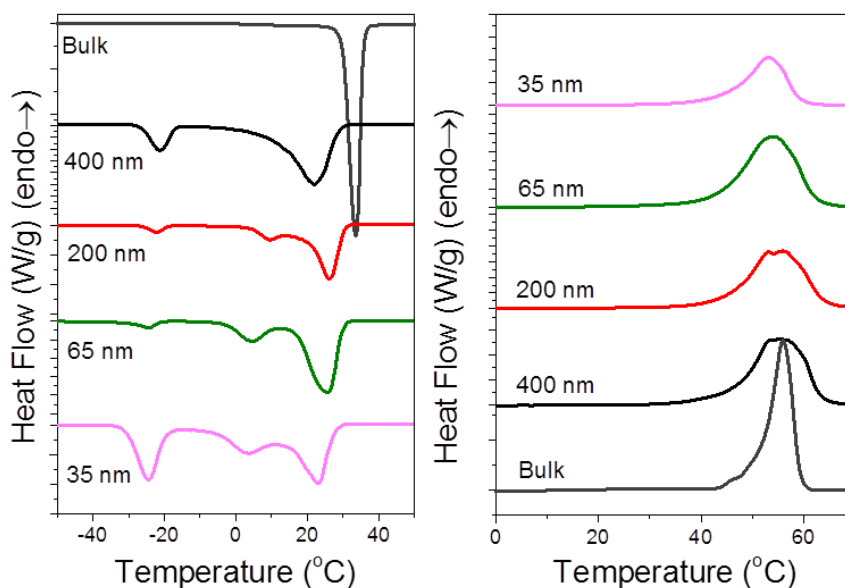


Figure 60. Cooling and (left) and subsequent heating (right) thermograms of bulk PEO₄₆ and PEO₄₆ located in AAO with pore diameters ranging from 400 nm to 35 nm in the presence of a top (*i.e.*, connecting) layer.

Secondly, the effect of chain polydispersity on the crystallization process was investigated. In chapter 3-1, we discussed the molecular weight dependence of homogeneous nucleation temperature. For relatively low molecular weights, homogeneous nucleation temperature strongly depends on polymer molecular weight; the lower the molecular weight is, the lower the homogeneous nucleation temperature is. For relatively high molecular weight polymers, the homogeneous nucleation temperature almost saturates. In this experiment, 10 wt% of high molecular weight PEO (PEO₂₂₇₀) was mixed with low molecular weight PEO (PEO₄₆).

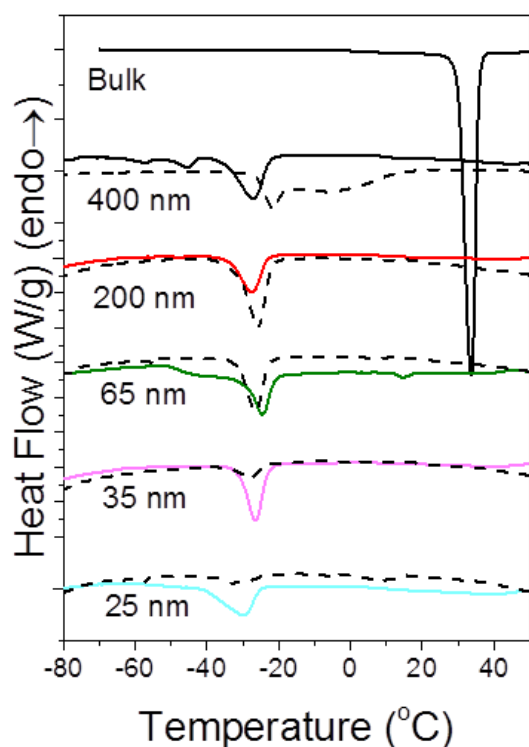


Figure 61. Cooling thermograms of bulk PEO₄₆ (black dashed line) and mixture of PEO₂₂₇₀ with 10 wt% into PEO₄₆ (color line) with a rate of 10 K/min.

In Figure 61, DSC traces of mixture of 10 wt% PEO₂₂₇₀ into PEO₄₆ are compared with pure PEO₄₆ upon confinement. Since homogeneous nucleation of PEO₄₆ is at lower temperature than that of PEO₂₂₇₀ (Figure 44), addition of PEO₂₂₇₀ is expected to increase the homogeneous nucleation temperature. Under some conditions, two homogeneous nucleation temperatures could be seen if some pores crystallized by the higher and lower molecular weights, respectively. The DSC traces (Figure 61) however, depicts a single nucleation event at a low temperature corresponding to the majority polymer (PEO₄₆). A single nucleation process has two possible interpretations: (i) PEO₄₆ may suppress the homogeneous nucleation of PEO₂₂₇₀ and/or (ii) the homogeneous nucleation temperature of PEO₂₂₇₀ is shifted to lower temperature and coincides with the homogeneous nucleation temperature of PEO₄₆ because of the faster segmental dynamics. In this view, the segmental dynamics of PEO₂₂₇₀ are plasticized (Figure 46) by the shorter PEO chains of PEO₄₆.

Lastly, the effect of mixing with another polymer was investigated. In this experiment, 5 wt% of PCL₆₈ was added to PEO₄₆. If PCL₆₈ acts as heterogeneous nuclei for PEO, then the dominance of heterogeneous nucleation is to be expected. As can be seen in Figure 62, in the asymmetric blend PEO₄₆/PCL₆₈ (95/5), PEO homogeneous nucleation mechanism remains the sole nucleation mechanism under confinement. This is not very surprising as PEO and PCL are miscible in the melt state (see section 3.4 below).

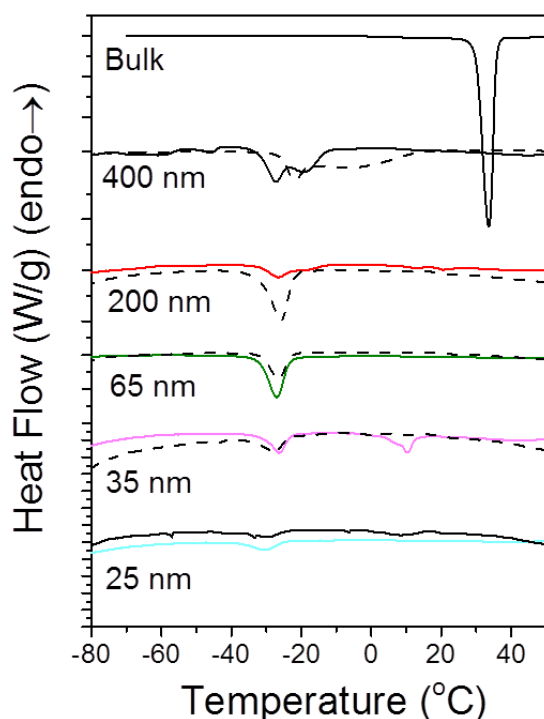


Figure 62. Cooling thermograms of bulk PEO₄₆ (black dashed line) and mixture of PCL₆₈ with 5 wt% into PEO₄₆ (color line) with cooling rates of 10 K/min.

In summary of this section, a clear effect of surface layer on top of the templates was observed. In the presence of a top layer, heterogeneous nucleation becomes the dominant nucleation mechanism. There are at least two different types of heterogeneous nucleation mechanisms in PCL and one of them may relate to the heterogeneous nucleation of thin film in a top layer. On the other hand, oligomers shift the homogeneous nucleation temperature to lower temperatures and this is attributed to the plasticizing effect of the liquid-to-glass temperature. Chain polydispersity and mixing with melt miscible chains does not alter significantly the homogeneous nucleation process. In both cases, homogeneous nucleation of the majority component remains unaltered.

3.4. Effect of confinement on the crystallization of double-crystalline diblock copolymers composed from PEO and PCL

Diblock copolymers comprising crystallizable blocks provide additional parameter space for studying the effect of confinement [29,35,115–117]. Polymer crystallization in bulk diblock copolymers is classified as confined, template and breakout, depending on the value of the product χN (where χ is the interaction parameter and N the total degree of polymerization) at the crystallization temperature with respect to the value at the order-to-disorder transition temperature [29]. Placing block copolymers under the extrinsic hard confinement provided by

AAO introduces additional parameters such as surface-polymer interactions and structural frustration related to incommensurability of the domain spacing to the pore diameter. Here we investigate the confined crystallization of double crystalline diblock copolymers of PEO-*b*-PCL within AAO. The crystallization in bulk PEO-*b*-PCL was already reported [118–120]. When PEO-*b*-PCL is located inside AAO, the PEO chains are subjected to double confinement: (1) confinement imposed by PCL crystals, which grow in bulk PEO-*b*-PCL at higher crystallization temperatures than PEO crystals and (2) hard confinement imposed by the rigid AAO pore walls. The investigation is made as a function of copolymer composition, pore size and heating/cooling rate with structural (X-ray scattering, polarizing optical microscopy), thermodynamic (DSC), and dynamic (dielectric spectroscopy) means. Although both homopolymers could crystallize homogeneously at large undercoolings, one of the blocks (PEO) in PEO-*b*-PCL confined to AAO is unable to crystallize under conditions where PCL crystallizes. Hence, the double soft/hard confinement imposed by the block copolymer domain structure and AAO pore geometry facilitates further control over crystallinity and thus a control over the final mechanical properties of copolymers with crystallizable blocks. We propose that confinement effects can be discussed in terms of the pertinent temperature vs. curvature “phase diagram” [99,100]. There, the equilibrium melt and nonergodic glassy states at higher and lower temperatures, respectively, are separated by the two nucleation regimes (heterogeneous and homogeneous). We explore the effect of proximity of nucleation regimes to these boundary states.

Effect of soft confinement by the nanodomain structure

The crystalline structure in the three diblock copolymers is discussed at the different pertinent length scales. The unit cell, nanodomain morphology, and spherulitic superstructure are obtained from wide-angle X-ray scattering (WAXS), small-angle X-ray scattering (SAXS) and polarizing optical microscopy (POM), respectively. WAXS on PEO-*b*-PCL revealed mixed scattering patterns with reflections that can be assigned to monoclinic PEO and orthorhombic PCL unit cell. As an example, the WAXS patterns of PEO₁₁₄-*b*-PCL₈₈ displayed in Figure 63 show the (120) and (032) reflections of monoclinic PEO at $2\theta = 19.5^\circ$ and $2\theta = 23.2^\circ$. The monoclinic PEO unit cell contains four PEO chains, each of which forms a $7/2$ helix. On the other hand, the (110), (111) and (200) reflections of orthorhombic PCL appear at 2θ angles of 21.3° , 21.9° and 23.6° . The PCL unit cell is composed from two chains with opposite orientation in an extended planar conformation [121].

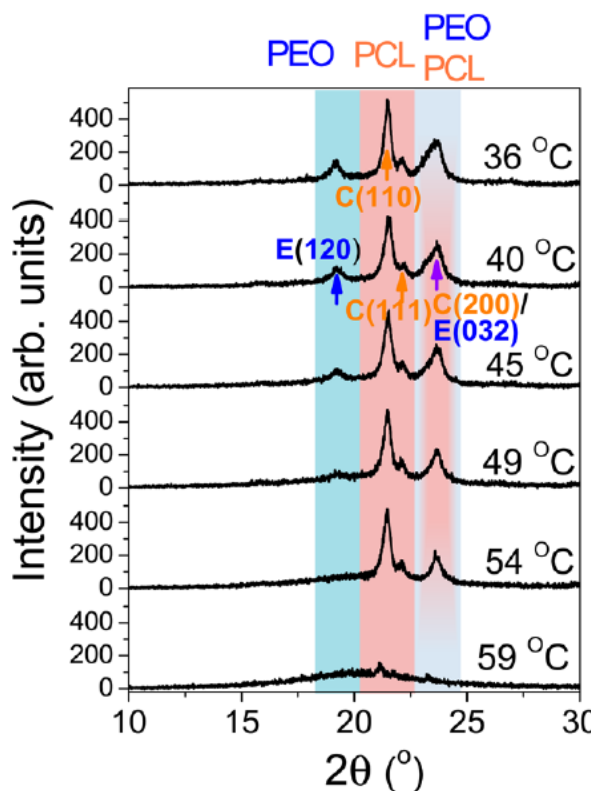


Figure 63. WAXS patterns measured in $\theta/2\theta$ geometry of bulk PEO-*b*-PCL at different temperatures. Letters E and C denote reflections of monoclinic PEO (E) and orthorhombic PCL (C). The corresponding Miller indices are indicated. Blue and red areas indicate 2θ ranges in which PEO and PCL reflections appear. The (200) reflection of PCL and the (032) reflection PEO coincide at $2\theta = 23.6^\circ$.

The appearance of PEO and PCL reflections in the WAXS patterns indicates the existence of regions in which PEO crystals are enriched and a high portion of PCL chains is incorporated in amorphous interphases as well as of different regions where now PCL crystals dominate and PEO chains are incorporated in amorphous interphases. Local suppression of crystallization of one block in the same double crystalline block copolymers was first reported in ref [118]. Basically, it is a consequence of the fact that both blocks would have to crystallize in different unit cells. On heating PEO₁₁₄-*b*-PCL₈₈, the PEO crystals melt at first at about 55 °C, whereas PCL crystals melt at about 65 °C.

The WAXS patterns of the three PEO-*b*-PCLs are compared in Figure 64, revealing reduced PEO crystallinity in the more asymmetric block copolymers.

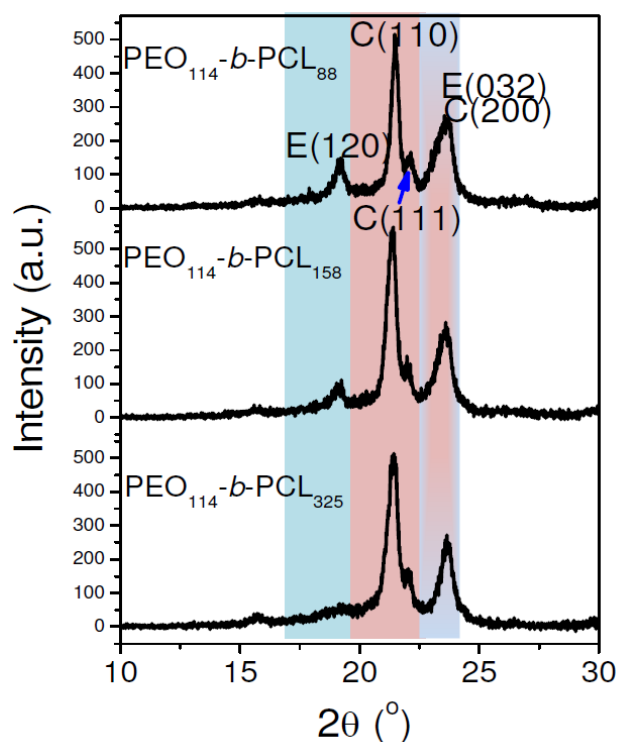


Figure 64. WAXS patterns measured in $\theta/2\theta$ geometry of bulk $\text{PEO}_{114}\text{-}b\text{-PCL}_{88}$, $\text{PEO}_{114}\text{-}b\text{-PCL}_{158}$, and $\text{PEO}_{114}\text{-}b\text{-PCL}_{88}$ at 40 °C. Letters E and C denote reflections of monoclinic PEO and orthorhombic PCL. The corresponding Miller indices are indicated. Blue and red areas indicate 2θ ranges in which PEO and PCL reflections appear.

Information on the state of the block copolymers prior to crystallization and on the nanodomain morphology following crystallization can be obtained from SAXS. Figure 65 illustrates the SAXS patterns of and oriented $\text{PEO}_{114}\text{-}b\text{-PCL}_{88}$ fiber as a function of temperature. At temperatures above the melting point of both blocks (*i.e.*, $T > 65$ °C) the scattering pattern does not contain any sharp peaks except a broad feature at lower scattering vectors, indicating that the block copolymer is disordered. Hence, the crystallization of PCL and PEO from the disordered melt drives the phase separation at lower temperatures in agreement with earlier reports [120]. The SAXS pattern at 30 °C is composed from a very broad peak around $q \sim 0.32 \text{ nm}^{-1}$. The broad feature (denoted with (a) in Figure 65) is associated with PEO crystals having average correlation distances in the range 13-19 nm. The narrower feature (denoted with b in Figure 65) reflects correlations of PCL crystals with an average correlation distance of 23.5 nm. These results are supported by the DSC traces.

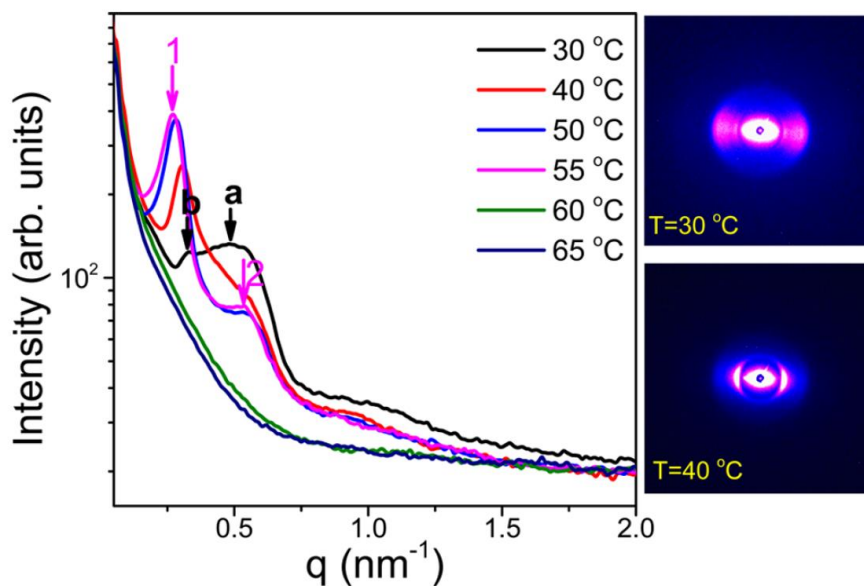


Figure 65. (Left) SAXS patterns of bulk $\text{PEO}_{114}\text{-}b\text{-PCL}_{88}$ at different temperatures as indicated. At 30 °C, (a) and (b) indicate the approximate peak positions associated with PEO and PCL crystals, respectively. The positions of the scattering vectors corresponding to the first and higher order reflections are shown for 55 °C. (Right) 2D-SAXS images obtained from extruded $\text{PEO}_{114}\text{-}b\text{-PCL}_{88}$ fibers at 30 (top) and 40 °C (bottom).

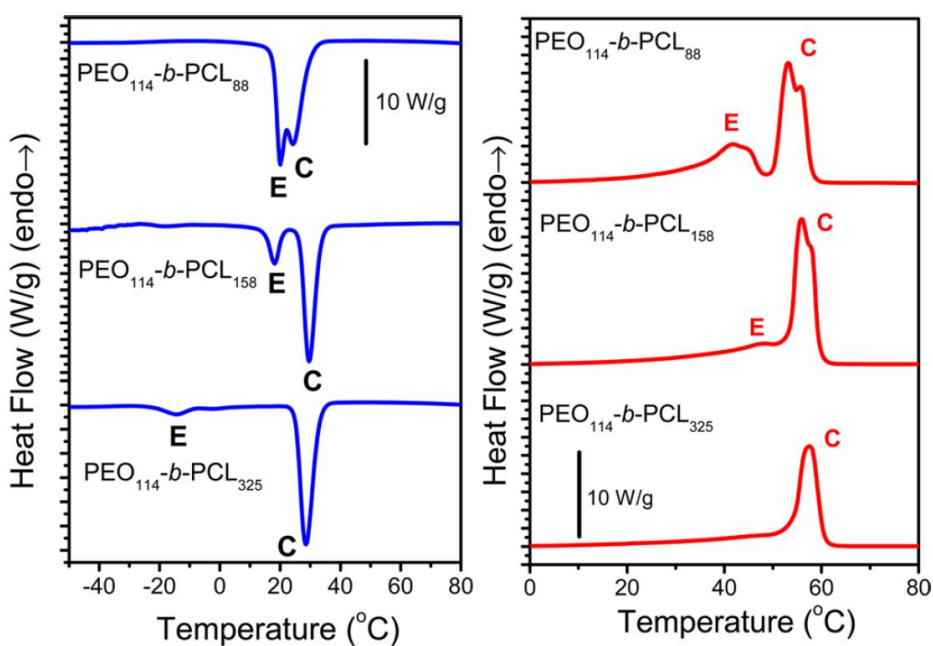


Figure 66. Cooling (left) and subsequent heating (right) thermograms of bulk $\text{PEO}\text{-}b\text{-PCL}$ (heating/cooling rate 10 K/min). Letters E and C denote crystallization/melting peaks of PEO and PCL, respectively.

Figure 66 shows the DSC traces of the three block copolymers on cooling and subsequent heating at a rate of 10 K/min. On cooling PEO₁₁₄-*b*-PCL₈₈, PCL crystallizes first (at ~25 °C) followed by the crystallization of PEO (at ~20 °C). On subsequent heating, PEO exhibits a broad melting peak ranging from 25 to 48 °C, in agreement with WAXS indicating a broad distribution of PEO crystal sizes. In PEO₁₁₄-*b*-PCL₁₅₈, PCL crystallizes at 29.6 °C followed by PEO crystallization at ~18.1 °C. On subsequent heating, there is again a broad PEO melting peak centered around 48 °C, followed by melting of PCL crystals. In general, the more asymmetric the investigated PEO-*b*-PCL is, the lower the PEO crystallization temperature is. This is more evident in PEO₁₁₄-*b*-PCL₃₂₅. Here, PCL crystallizes at 28.5 °C whereas PEO crystallization is shifted to -14.6 °C. The decrease in the PEO crystallization temperature can be understood by the confinement of PEO chains imposed by PCL crystals. A similar effect has found from PEO study discussed earlier. Confinement in pores with diameters below 200 nm resulted in homogeneous crystallization of PEO at substantially lower temperatures as in the case of PEO-*b*-PCL confined to AAO. The extracted degrees of crystallinity for both PEO and PCL chains ($X_c = \Delta H/w\Delta H_0$, where ΔH is the measured heat of fusion, ΔH_0 is the heat of fusion of an “ideal” crystal and w is the weight fraction of PEO or PCL in the diblocks) are listed in Table 5, Section 2-2.

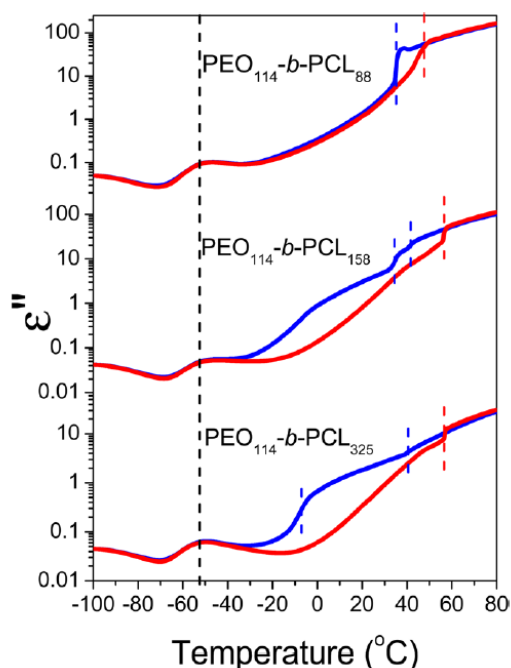


Figure 67. Isochronal dielectric loss curves (blue, cooling; red, heating) of bulk PEO₁₁₄-*b*-PCL₈₈ obtained at a frequency of 1154 Hz (heating/cooling rate 2 K/min). Dashed lines indicate crystallization temperatures (blue), melting temperatures (red) and the location of the segmental process (black), respectively.

The complex dielectric permittivity, ϵ^* , is also a sensitive probe of the structural and dynamic changes in the block copolymers. It has been shown earlier [99,100] that the temperature

dependence of dielectric permittivity and loss can be used as fingerprints of phase transitions. Figure 67 depicts the dielectric loss curves of the three copolymers on cooling and subsequent heating (with a rate of 2 K/min) under isochronal conditions ($f = 1154$ Hz). On cooling, PCL and PEO crystallization are better separated as shown by the blue dashed curves. For example, in $\text{PEO}_{114}\text{-}b\text{-PCL}_{325}$, PCL and PEO crystallization temperatures are separated by about 45 °C which is also in qualitative agreement with the DSC curves despite different cooling rates were applied. New information from the isochronal DS measurements is the dielectric loss peak at about -52 °C that, as it will be discussed below (with respect to Figure 68), associates with the molecular dynamics of amorphous PCL segments.

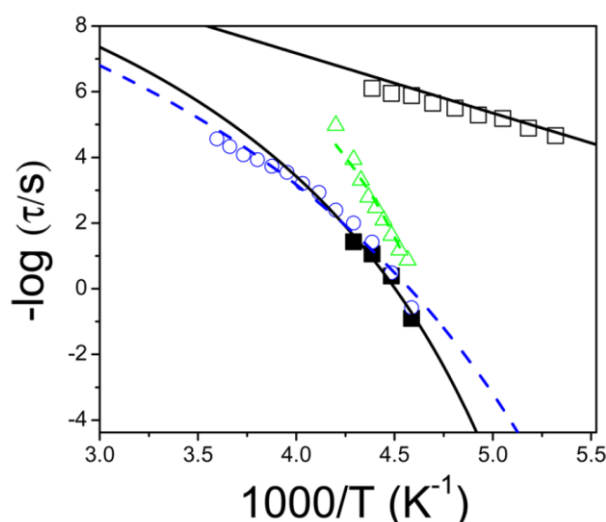


Figure 68. Relaxation times at maximum loss of bulk $\text{PEO}_{114}\text{-}b\text{-PCL}_{88}$. The α - (filled squares) and β - (open squares) processes are shown. Black lines represent fits to the VFT and Arrhenius equations. The α - relaxation times of bulk PEO (open triangles) and bulk PCL (open circles) are shown for comparison.

The α - and β -processes in bulk $\text{PEO}_{114}\text{-}b\text{-PCL}_{88}$ were fitted according to the HN function with respective shape parameters $m=0.55$, $n=0.50$ and $m=0.16$, $n=0.22$. Typical dielectric loss curves are depicted in Figure 69 at temperatures corresponding to the segmental (α -) and local (β -) processes. The two processes in $\text{PEO}_{114}\text{-}b\text{-PCL}_{88}$ have distinctly different T -dependencies and are shown in Figure 68 together with the bulk PEO and PCL times. The α - process in the copolymers conforms to the VFT equation: $\tau = \tau_0 \exp(B/(T - T_0))$, where τ_0 ($=10^{-12}$ s; held fixed because of the limited frequency range), B ($=1940$ K), T_0 ($=152$ K). The values of these parameters are in proximity to the PCL homopolymer values. The β -process conforms to an Arrhenius equation, $\tau = \tau_0 \exp(E/RT)$, with $\tau_0 = 1.4 \times 10^{-13}$ s and an activation energy, E , of 29.4 kJ/mol.

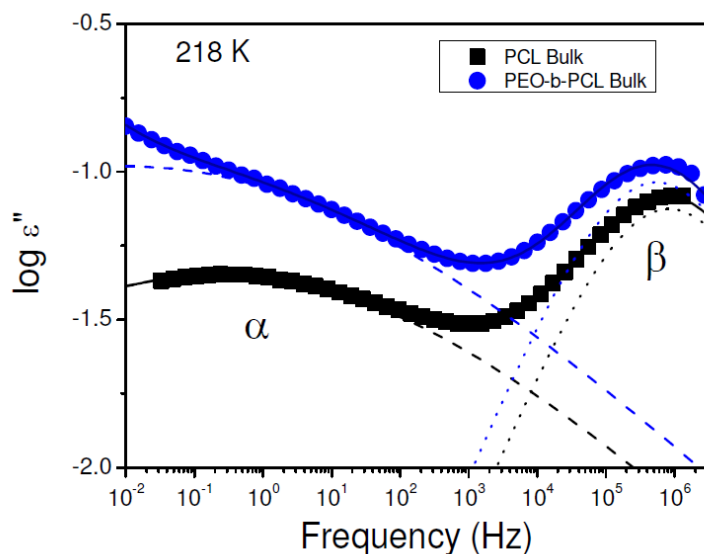


Figure 69. Dielectric loss as a function of frequency for PCL homopolymer and PEO₁₁₄-*b*-PCL₈₈ at 218 K. The dashed and dotted lines give the segmental (α -) and local (β -) processes, respectively.

The superstructure formation in the block copolymers was subsequently studied by POM. Measurements were made isothermally following quenching from the isotropic phase to different final crystallization temperatures. Figure 70 displays the growth rates of the superstructures that are associated with PCL crystals. Initially, PCL crystals consist of elongated (axialitic) objects that are converted into spherulites as crystal growth proceeds [118]. The growth rates of PCL superstructures can be fitted according to the Lauritzen-Hoffman theory or by the recent modification proposed by Strobl. According to the latter mode, the growth rate of a superstructure contains two terms with opposite temperature dependence (equation 1.14). As discussed earlier, the first term refers to the segmental mobility according to the VFT equation that reflects the dynamics of amorphous PCL segments. The second term reflects the free energy of activation for the placement of a secondary nucleus on the growth face. T_{zg} is the zero-growth temperature, *i.e.*, the temperature above which the superstructures cannot grow. The obtained T_{zg} values were 357, 353, and 353 K, respectively, for PEO₁₁₄-*b*-PCL₈₈, PEO₁₁₄-*b*-PCL₁₅₈ and PEO₁₁₄-*b*-PCL₃₂₅. In the same figure the growth rates of PCL and PEO homopolymers are included. Evidently, the growth rates of the formed superstructures in the three copolymers can be attributed to crystals formed by the PCL blocks as indicated by two observations. First, the temperature dependence of the growth rates is more similar to the growth rates of PCL homopolymer crystals. Second, the evolution of the growth shapes in the course of crystal growth (from axialities to spherulites) resembles that observed for PCL homopolymers (Figure 70). PEO, on the other hand, was found to crystallize in the background of the already impinged PCL spherulites in much larger spherulitic domains in the PEO₁₁₄-*b*-PCL₈₈ with the higher PEO

content and the higher PEO crystallinity (Table 5). This again confirms the preferential nucleation of PCL or PEO chains in the superstructures.

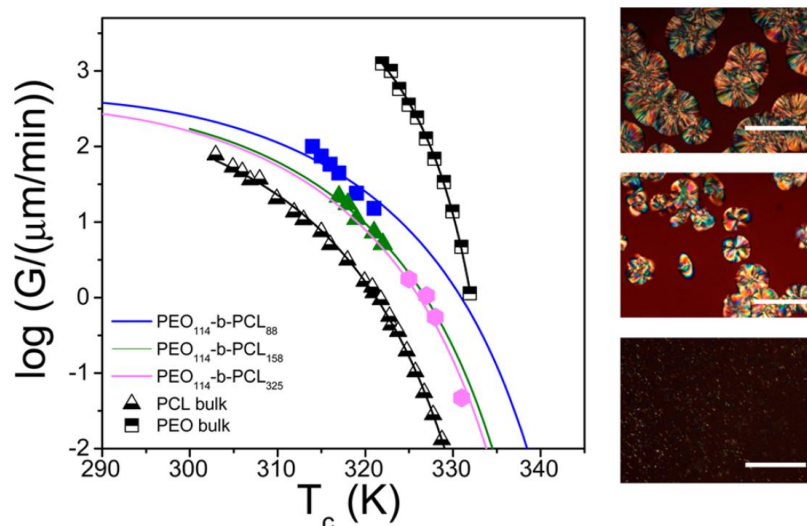


Figure 70. (Left) Spherulitic growth rates plotted as a function of temperature for PEO₁₁₄-b-PCL₈₈ (blue squares), PEO₁₁₄-b-PCL₁₅₈ (green triangles), PEO₁₁₄-b-PCL₃₂₅ (magenta hexagons), PEO homopolymer (black squares) and PCL homopolymer (black triangles). The lines are fits according to the Lauritzen-Hoffman and Strobl theories. (Right) POM images of PEO₁₁₄-b-PCL₈₈ (Top, $T=43$ °C), PEO₁₁₄-b-PCL₁₅₈ (middle, $T=46$ °C) and PEO₁₁₄-b-PCL₃₂₅ (bottom, $T=54$ °C), respectively. The scale bars correspond to 50 μm.

Thus, in the bulk block copolymers it is crystallization that drives phase separation. In this case, both blocks are able to crystallize via heterogeneous nucleation. However, in the more asymmetric copolymer, the minority block (PEO) is able to crystallize only at lower temperatures by homogeneous nucleation.

Effect of hard confinement by the AAO templates

The most dramatic effect of the hard confinement imposed by the rigid AAO pore walls on PEO-*b*-PCL is suppression of PEO crystallization. This is evident, for example, in the WAXS patterns of PEO₁₁₄-b-PCL₈₈ obtained at temperatures of -40 and -60 °C shown in Figure 71. The reason for performing WAXS measurement at such low temperatures will be explained later. Here we only mention that at such temperatures both PCL and PEO homopolymers would crystallize either heterogeneously and/or homogeneously. However, the WAXS pattern of PEO₁₁₄-b-PCL₈₈ inside AAO contains only a subset of the reflections appearing in WAXS patterns of bulk PEO₁₁₄-b-PCL₈₈. The selective appearance of these reflections indicates

preferred orientation of the {110} and {200} faces normal to the AAO pore axes. The same preferred orientation was found in PCL homopolymer located AAO. Schulz scans in that case revealed Hermans orientation parameter of ~ 0.95 , suggesting a nearly uniform orientation of the {110} crystal faces perpendicular to the AAO pore axes.

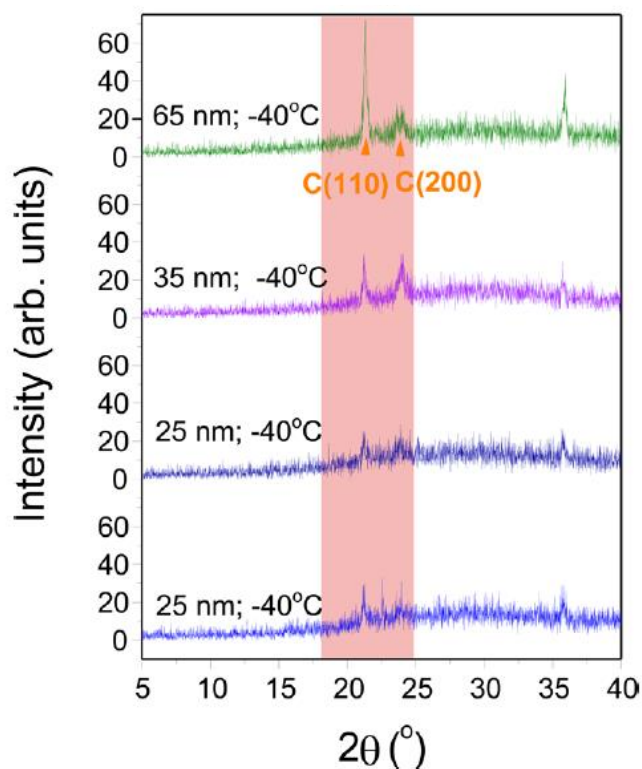


Figure 71. WAXS patterns measured in $\theta/2\theta$ geometry of $\text{PEO}_{114}\text{-}b\text{-PCL}_{88}$ located inside AAO with pore diameters ranging from 65 to 25 nm at -40 and -60 °C. The main PCL reflections (C) are indicated.

The effect of the hard confinement imposed by the rigid AAO pore walls on the type of nucleation process initiating crystallization in $\text{PEO-}b\text{-PCL}$ can be studied by DSC. Figure 72 shows DSC cooling traces and the subsequent heating traces (rate 10 K/min) of $\text{PEO}_{114}\text{-}b\text{-PCL}_{88}$ inside AAO in comparison with bulk $\text{PEO}_{114}\text{-}b\text{-PCL}_{88}$. As discussed above, DSC cooling runs of bulk $\text{PEO}_{114}\text{-}b\text{-PCL}_{88}$ show a dual exothermic peak associated with PCL (peak at 25 °C) and PEO (peak at 20 °C) crystallization. The DSC traces of $\text{PEO}_{114}\text{-}b\text{-PCL}_{88}$ confined to AAO reveal completely different crystallization behavior. Now the main crystallization peak is at lower temperatures and upon confinement shifts to even lower temperatures, from ~ 26 °C in 65 nm pores to about -53 °C in 25 nm pores. A weak exothermic peak is also visible at higher temperatures in some of the traces. These DSC traces can be interpreted with the aid of the WAXS results. Within AAO only PCL can crystallize. Thus, the exothermic peaks in the DSC curves reflect solely crystallization of PCL crystals. We attribute the weak exothermic peak at higher temperatures to PCL heterogeneous nucleation as found also in bulk PCL. Heterogeneous crystallization is a minor crystallization

mechanism in the smaller pores. Heterogeneous nucleation in the large pores can be explained as same as previous discussion in PEO and PCL study. The spherulite diameters of PCL crystals upon impingement are ~ 250 , 100 , and $40 \mu\text{m}$, respectively, in $\text{PEO}_{114}\text{-}b\text{-PCL}_{88}$, $\text{PEO}_{114}\text{-}b\text{-PCL}_{158}$, and $\text{PEO}_{114}\text{-}b\text{-PCL}_{325}$. This allows estimating the volume per heterogeneous nuclei, which is about $\sim 10^{-2}$, 10^{-4} and 10^{-5}mm^3 , respectively. However, within AAO, the copolymers are confined to discrete cylindrical pores with volumes in the range from $3 \times 10^{-9} \text{mm}^3$ (pore diameter 200nm , pore depth $100 \mu\text{m}$) to $5 \times 10^{-11} \text{mm}^3$ (pore diameter 25nm , pore depth $100 \mu\text{m}$). Since these pore volumes are several orders of magnitude smaller than the volume per heterogeneous nucleus in bulk $\text{PEO-}b\text{-PCL}$, only a minor fraction of pores will contain heterogeneous nuclei. The crystallization peak denoted E in the DSC traces of Figure 72 can be ascribed to PCL located in AAO pores containing heterogeneous nuclei.

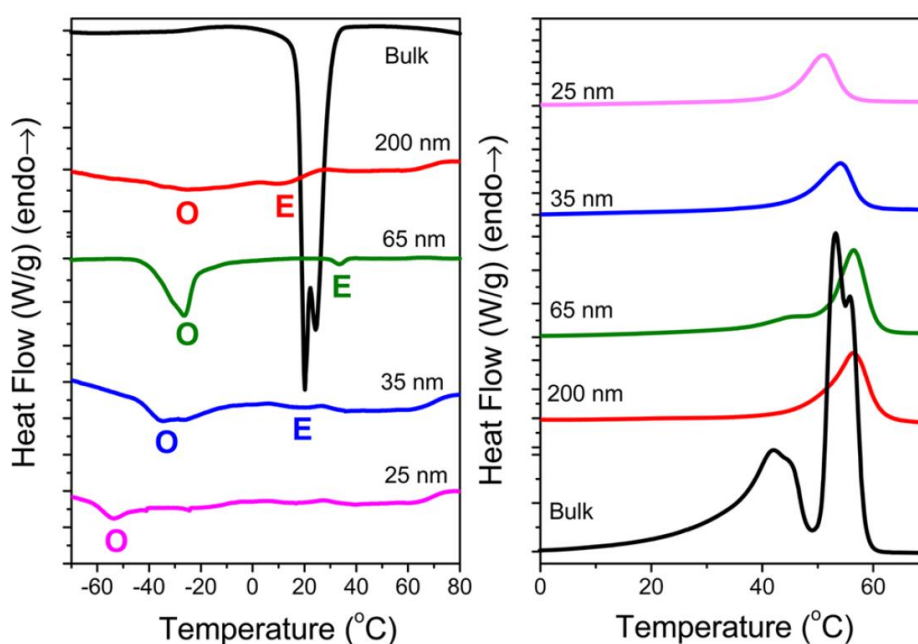


Figure 72. Cooling (left) and subsequent heating (right) thermograms of bulk $\text{PEO}_{114}\text{-}b\text{-PCL}_{88}$ and of $\text{PEO}_{114}\text{-}b\text{-PCL}_{88}$ located inside AAO with pore diameters ranging from 400 to 25nm (heating/cooling rate 10K/min). DSC thermograms of the corresponding bulk block copolymers are shown for comparison. Letters E and O denote heterogeneous and homogeneous nucleation, respectively.

The probability of heterogeneous nucleation in the smaller pores is negligible; PCL in the smaller pores can only nucleate by crossing the intrinsic barrier for homogeneous nucleation. The critical nucleus size for homogeneous nucleation l^* , ($l^* = 4\sigma_e T_m^0 / \Delta T \Delta H_m \rho_c$), with σ_e (106 and 93mJ/m^2 for PCL and PEO, respectively), T_m^0 (348 and 331K for PCL and PEO,

respectively), ΔH_0 (148 and 200 J/g for PCL and PEO, respectively), $\Delta T = T_m^0 - T_c$ the undercooling and ρ_c (1.187 and 1.239 g/cm³, respectively, for PCL and PEO) the crystal density. For the PCL block in PEO₁₁₄-*b*-PCL₈₈ ΔT is 30 K, but it increases to 105 K for PEO₁₁₄-*b*-PCL₈₈ inside AAO with a pore diameter of 25 nm. At such undercooling, the critical nucleus size for homogeneous PCL nucleation is about 8 nm and, therefore, smaller than the diameter of the smallest pores. Thus, the PCL blocks of PEO-*b*-PCL are able to crystallize even within 25 nm pores. However, the onset of PCL crystallization limits the available space for PEO crystallization. Homogeneous nucleation of PEO at an undercooling of $\Delta T = 100$ K requires a critical nucleus size of ~ 5 nm and this size increases at higher temperatures, *i.e.*, by decreasing ΔT . Thus, PEO chains in PEO-*b*-PCL located in AAO remain amorphous, being restricted by the rigid AAO pores walls and by PCL crystals already formed.

In the previously discussed PEO study, we proposed a relation of the homogeneous nucleation process with the spatiotemporal heterogeneity associated with the liquid-to-glass temperature. To explore the relationship in the present system, DS measurements have been carried out on the PEO₁₁₄-*b*-PCL₈₈ located inside AAO in comparison to the bulk PEO₁₁₄-*b*-PCL₈₈. The results for the segmental dynamics are shown in the Arrhenius representation of Figure 74. There is a speed-up of the PCL segmental dynamics in PEO₁₁₄-*b*-PCL₈₈ inside AAO with respect to bulk PEO-*b*-PCL (Figure 73) and only a minor effect on the local β -process. In addition, as with PEO, the effect of confinement is to broaden the distribution of relaxation times associated with the segmental process.

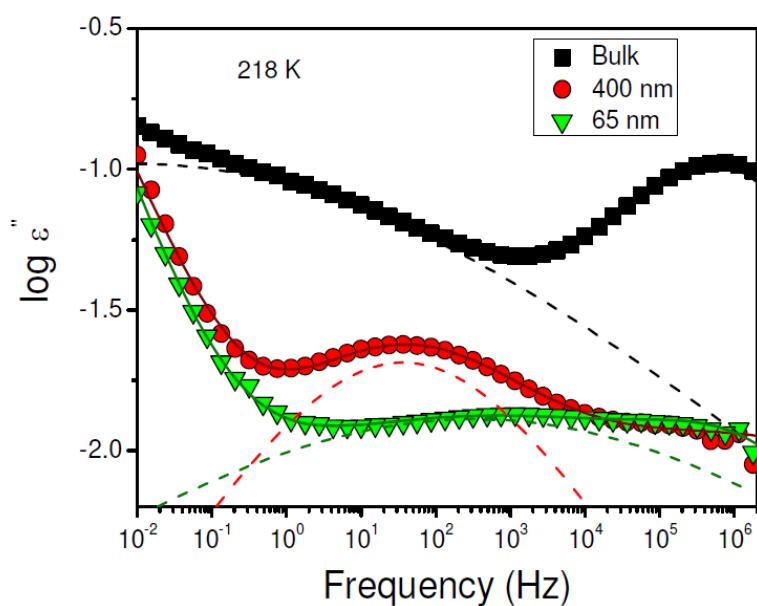


Figure 73. Dielectric loss as a function of frequency for bulk PEO₁₁₄-*b*-PCL₈₈ and PEO₁₁₄-*b*-PCL₈₈ inside AAO with two pore diameters, 400 nm and 65 nm, at 218 K. Dashed lines give the segmental process. Notice the shift and broadening of the segmental process.

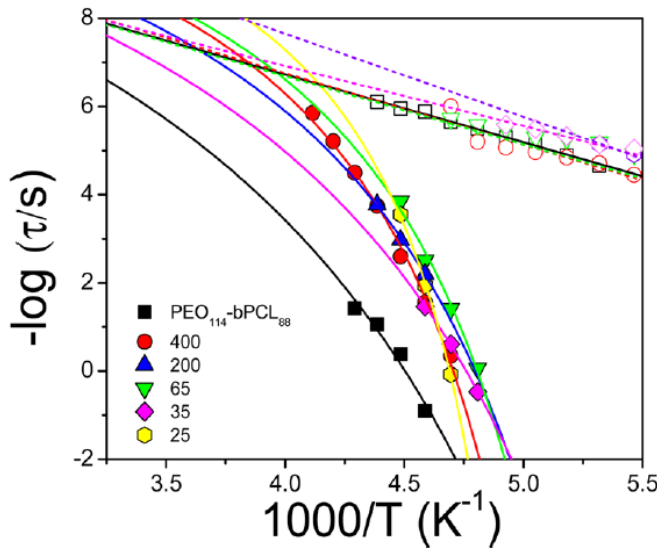


Figure 74. Relaxation times at maximum loss corresponding to the PCL α - and β -processes in bulk $\text{PEO}_{114}\text{-}b\text{-PCL}_{88}$ and $\text{PEO}_{114}\text{-}b\text{-PCL}_{88}$ confinement to AAO with pore diameters ranging from 400 nm to 25 nm; (squares): bulk $\text{PEO}_{114}\text{-}b\text{-PCL}_{88}$ and $\text{PEO}_{114}\text{-}b\text{-PCL}_{88}$ within AAO with a pore diameter of 400 nm (circles), 200 nm (up triangles), 65 nm (down triangles), 35 nm (rhombi) and 25 nm (hexagons). Solid and dashed lines indicate fits to the α - and β -processes, respectively, with the VFT and Arrhenius equations.

The modifications of nucleation behavior and local segmental dynamics of $\text{PEO}_{114}\text{-}b\text{-PCL}_{88}$ related to the hard confinement imposed by the rigid AAO pores on the copolymers can best be discussed in terms of the “phase-diagram” of Figure 74. This diagram is based on the DSC results obtained on cooling (heterogeneous and homogeneous nucleation) and heating (apparent melting temperatures) as well as on the liquid-to-glass temperatures obtained from DS (T_g is operationally defined as the temperature where the segmental time is at $\tau \sim 100$ s). Figure 74 depicts the polymer melt state at high temperatures separated from the nonergodic glassy state at lower temperatures by two crystal nucleation regimes; heterogeneous nucleation at higher temperatures and homogeneous nucleation at lower temperatures. In $\text{PEO}_{114}\text{-}b\text{-PCL}_{88}$, both nucleation processes are solely ascribed to PCL, which is the only crystallizable component under conditions of double confinement. The liquid-to-glass temperature also refers to the freezing of the local segmental dynamics of the more polar PCL block. Interestingly, there seems to be a minimum in the $T_g(1/d)$ dependence at around 50 nm pores. In addition, homogeneous nucleation occurs in the vicinity of the liquid-to-glass temperature. For $\text{PEO}_{114}\text{-}b\text{-PCL}_{88}$ inside 25 nm pores, PCL homogeneous nucleation is located only 10 K above the corresponding T_g . This finding is a further confirmation of the close relation between the spatio-temporal fluctuations associated with the liquid-to-glass temperature and the onset of homogeneous nucleation. In this picture, homogeneous nucleation is controlled by the faster segments in the distribution of relaxation times associated with the α - process.

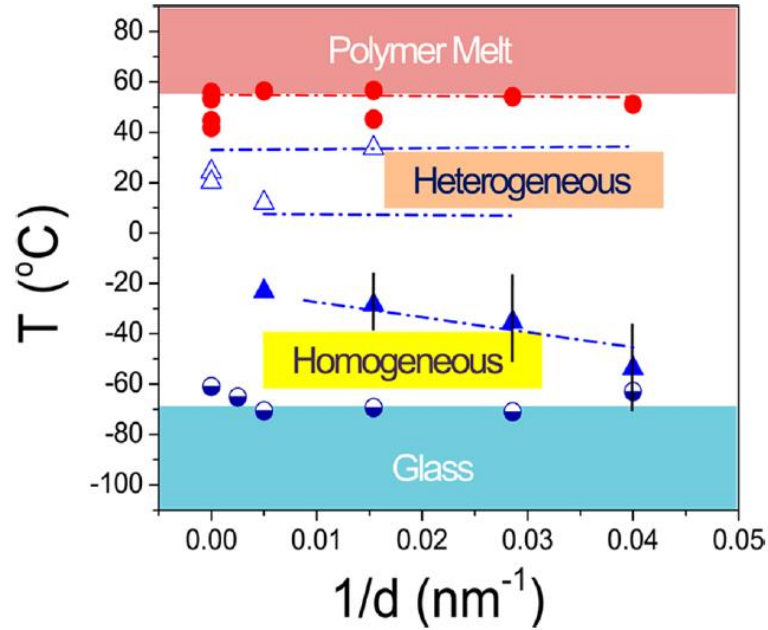


Figure 75. “Phase diagram” of PEO₁₁₄-*b*-PCL₈₈ within AAO based on DSC measurements and dielectric spectroscopy (liquid-to-glass temperatures). Filled spheres denote apparent melting temperatures obtained by DSC. Open and filled triangles denote temperatures at which crystallization of PCL is initiated by heterogeneous and homogeneous nucleation, respectively. Liquid-to-glass temperatures (half-filled spheres) obtained by DS are operationally defined as corresponding to 100 s. Horizontal dashed lines give the range of heterogeneous nucleation for bulk PCL. The dashed line in the vicinity of homogeneous nucleation is a guide for the eye.

In the next section we explore the effect of confinement on the crystallization and dynamics of water located within the same templates. Our aim is to extract the pertinent phase diagram under confinement and to compare it with the one for polymer presented in Figure 75.

3.5. Structure of Ice under confinement

As discussed in the introduction, of central importance to the discussion of the different phases of ice is the existence of pure cubic ice at ambient conditions. Since partial cubic ice has been reported in small droplets and in confined space, AAO can be considered as a good alternative confining medium. Herein we present a structural study of confined water in the same AAO templates.

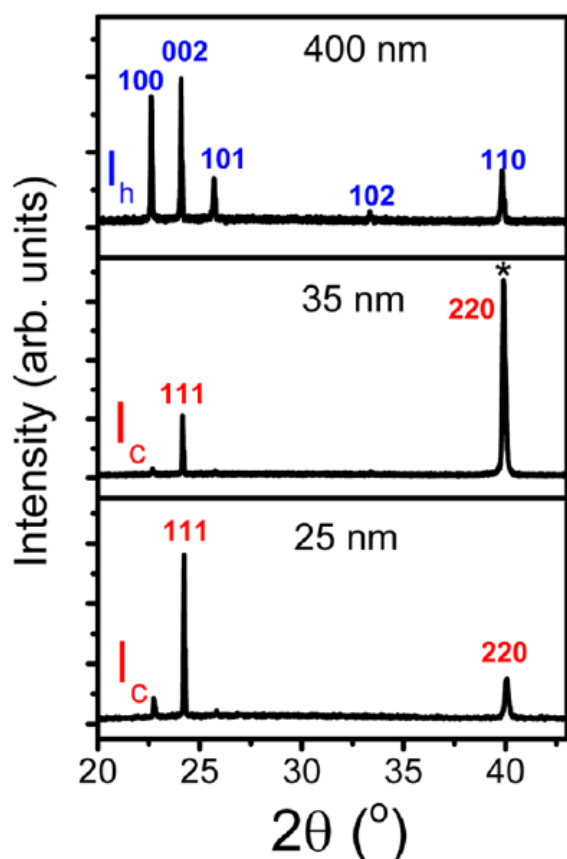


Figure 76. WAXS patterns measured in $\theta/2\theta$ geometry of confined water in AAO. Diameters of AAO pores are 400 nm (Top), 35 nm (Middle) and 25 nm (Bottom). In this configuration, the AAO pore axes are oriented parallel and the AAO surface oriented perpendicularly to the plane of the incident and scattered X-ray beams. The main reflections corresponding to hexagonal ice (I_h) and cubic ice (I_c) are shown in blue and red, respectively. The star indicates background scattering from the Al substrate.

Figure 76 shows WAXS patterns of ice confined to AAO with diameters of 400 nm, 35 nm and 25 nm at -50°C . Diffraction patterns within AAO with a pore diameter of 400 nm show relative peak intensities similar to those of bulk water. The (111) and (200) reflections were more intense, but the structure is still identified as I_h . When reducing the pore diameter to 35 and 25 nm, the diffraction patterns were fundamentally different. The dominant peaks correspond to the (111) and (220) reflections of cubic ice (I_c). A minor feature is some remaining peaks from the I_h structure most likely due to condensation at the AAO surface. Another possibility is the formation of stacked disordered ice (I_{sd}) containing a small amount of stacking faults. To the best of our knowledge, under atmospheric conditions such

diffraction patterns corresponding to a predominantly cubic ice at $-50\text{ }^{\circ}\text{C}$ have not been reported previously.

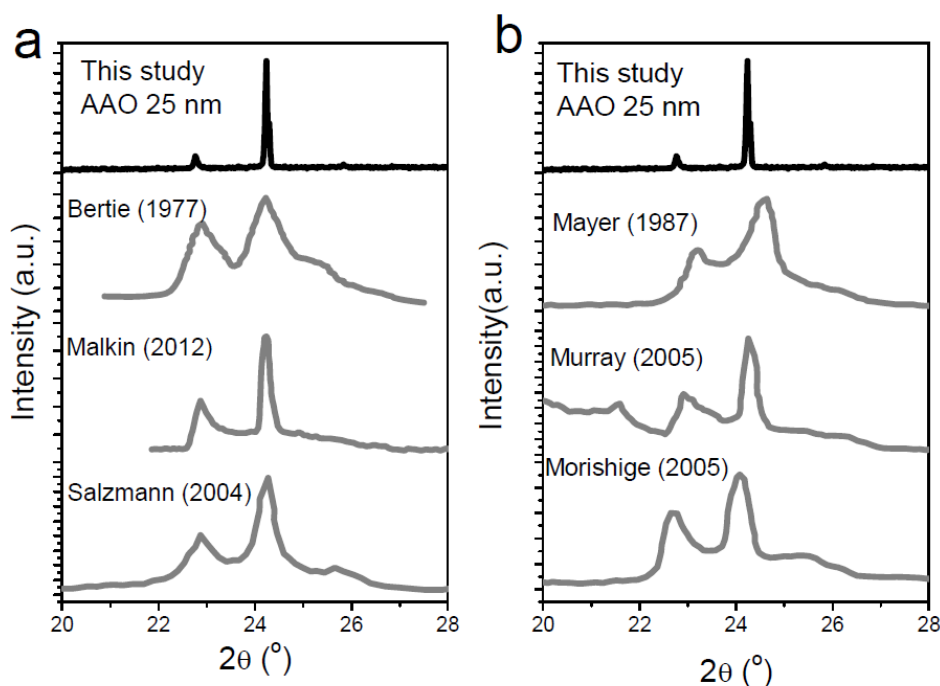


Figure 77. Comparison of the diffraction patterns of water frozen inside AAO with a pore diameter of 25 nm obtained at $-50\text{ }^{\circ}\text{C}$ to some X-ray patterns from the literature. a. Data from bulk metastable ice [68] [140] [141]. b. Data from confined metastable ice [70] [72] [142]. The patterns were digitized from the references so the quality may be poor. Nevertheless the patterns clearly show a “predominantly I_c ” in the present study unlike the other studies.

In order to further emphasize this point, a comparison of previously reported X-ray diffraction patterns for unconfined (left) and confined (right) ice with the present case is made in Figure 77. The chosen diffraction patterns are some of the best reported diffraction patterns of cubic ice. In general, the (101) peak for hexagonal ice is almost suppressed. However, the (100) peak from hexagonal ice is still present. This is the reason for proposing the stacked disorderd ice that contains both hexagonal and cubic sequences. On the other hand, the diffraction pattern for ice within the present AAO templates shows predominantly cubic ice. The intensity of the (100) peak from hexagonal ice is very weak in comparison to (111) peak of cubic ice. Given that condensation of ice on top of the AAO surface is unavoidable in our set-up and this will certainly produce some hexagonal ice, we are justified in saying that ice within AAO template is nearly in pure cubic phase. In fact, it is the purest I_c structure reported under ambient pressure conditions (*i.e.*, on earth).

In addition, this form is stable under annealing and persists up to the melting point as shown in the diffraction patterns of Figure 78 obtained at $-50\text{ }^{\circ}\text{C}$ and subsequently at $-10\text{ }^{\circ}\text{C}$. Both patterns indicate a predominantly I_c form. To the best of our knowledge, all the forms of previously reported cubic ice are known to change into hexagonal ice at around $-40\text{ }^{\circ}\text{C}$ [122,123]. On the other hand, the cubic ice formed in AAO is stable even at $-10\text{ }^{\circ}\text{C}$ and directly melts without phase transition to hexagonal ice. Hence, this is the first time that a *stable* cubic ice is reported.

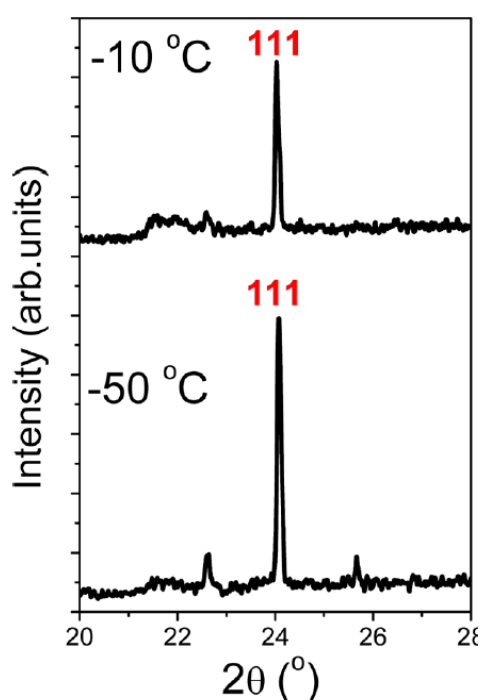


Figure 78. Diffraction patterns of water frozen inside AAO with a pore diameter of 35 nm (bottom) at $-50\text{ }^{\circ}\text{C}$ and following subsequent heating to $-10\text{ }^{\circ}\text{C}$ (top). The main reflection (111) of cubic ice is indicated.

As with polymer nucleation within the same templates, information on the nucleation mechanism can be extracted by comparing the size of critical nuclei with the pore diameter. The suppression of the hexagonal and the dominance of cubic phase in AAO pores having diameters $\leq 35\text{ nm}$ can be understood if we compare the size of the critical nuclei, l^* , with respect to the pore size, d . It is known that certain metastable crystalline phases can be stabilized within nanoporous materials such as AAOs. This may reflect the relation of the critical nucleus size to the degree of undercooling, ΔT (equation 1.12). Phases formed at small undercooling have large nuclei that are most affected by confinement. In the smaller pores only phases having $l^* < d$ are stable. On the basis of this finding, the radius of the critical nucleus for the I_c phase is below $\sim 17\text{ nm}$, which is in excellent agreement with a thermodynamic estimate from Johari.

3.6. Nucleation mechanism of ice in confinement

As we mentioned earlier the high dielectric permittivity of water and its temperature dependence is employed as a fingerprint of the mechanism of ice nucleation. Figure 79 (left) compares the dielectric permittivity of bulk water measured at a frequency of 1 MHz with water in AAO for pore diameters ranging from 400 nm down to 25 nm. The derivative of permittivity with respect to temperature is shown in Figure 79 (right). This gives more clear peaks corresponding to the phase transition temperature.

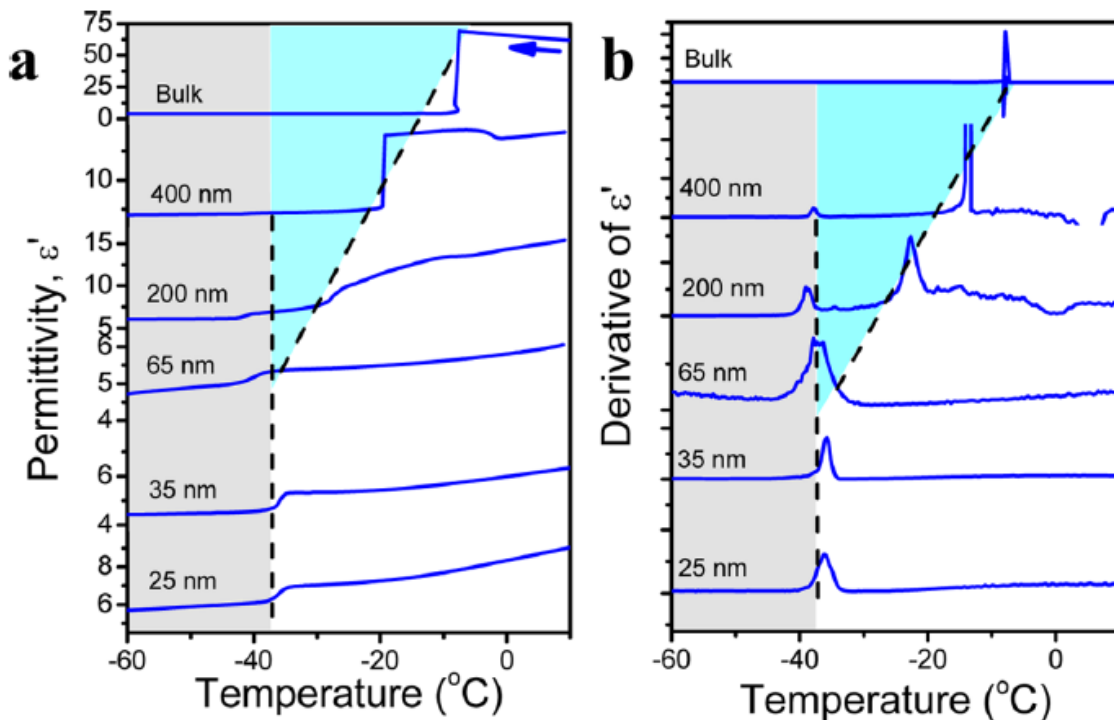


Figure 79. Temperature dependence of the dielectric permittivity for bulk water and water inside AAO measured at 1 MHz. a) Permittivity obtained on cooling with 5 K/min. Gray and blue areas correspond to ice formation via homogeneous and heterogeneous nucleation, respectively. b) Derivative of dielectric permittivity, $d\epsilon'/dT$, as a function of temperature.

At the cooling rate of 5 °C/min, bulk water freezes at -7.9 °C. The bulk dielectric permittivity first increases on cooling. Below freezing, the permittivity value corresponds to the limiting high frequency permittivity of hexagonal ice of $\epsilon'_{\infty} \sim 3.2$.

The dielectric permittivity of water inside AAO within a pore diameter of 400 nm was substantially different (Figure 80). First, the permittivity had a tendency to decrease upon cooling except in the range from 7.5 to 1.2 °C where it increased by 7.5%. The overall decrease was due to the unavoidable fact that during the experiment a small amount of water evaporated. The steep increase likely reflects changes of the effective dipole moment due to

dipole-dipole interactions namely, the Kirkwood factor g : $g = \mu_{interact}^2 / \mu^2$, where $\mu_{interact}$ is an interacting dipole moment while μ is the non-interacting isolated dipoles. Upon further cooling, water froze at -13.6 °C to a permittivity value of ~ 5 . Continuous decrease of permittivity from -13.6 °C to ~ -38 °C could reflect secondary crystallization. At -38 °C, another clear step is observed. This temperature is the lowest reported temperature for water crystallization via homogeneous nucleation for confinement within submicron sizes. The step in dielectric permittivity at this temperature is $\Delta\epsilon \sim 0.16$, that is, only a fraction of the step at -13.6 °C ($\Delta\epsilon \sim 12.4$). Based on this observation, it is concluded that the majority of pores contain impurities that initiate crystallization via heterogeneous nucleation. However, about 1% of pores are either free from such heterogeneities or the nucleation mechanism in these pores is very slow.

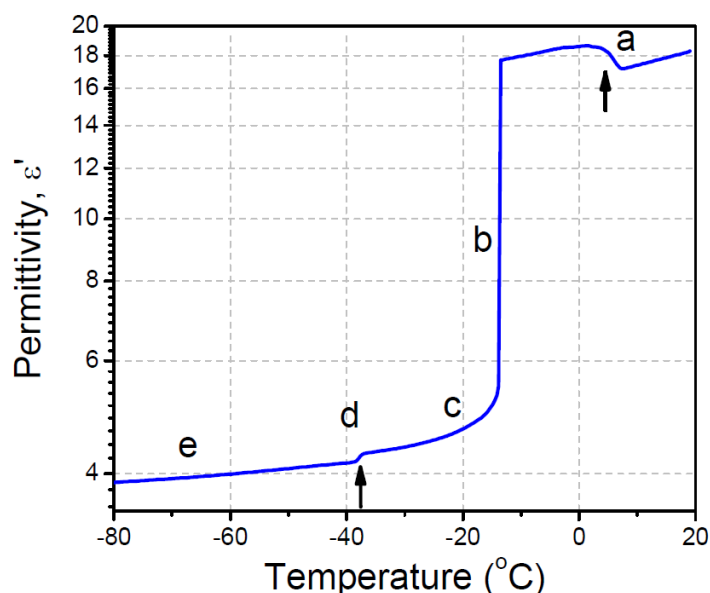


Figure 80. Detailed temperature dependence of dielectric permittivity for water in AAO with pore diameter of 400 nm. The permittivity is obtained on cooling with 5 K/min at a frequency of 1 MHz. Different regimes are indicated that corresponds to: (a) Permittivity change due to density anomaly of water. (b) Crystallization to I_h via heterogeneous nucleation. (c) Continuous decrease of permittivity presumably due to secondary crystallization. (d) Crystallization to I_c via homogeneous nucleation. (e) Further decrease of dielectric permittivity on cooling.

In AAO with a pore diameter of 200 nm in Figure 79, first a shallow increase in dielectric permittivity in the range from 1.5 to -1.7 °C was observed, followed by stepwise decrease at -22.7 and -38.9 °C attributed to heterogeneous and homogeneous nucleation, respectively.

Crystallization in the smaller pores was fundamentally different. Only a single step in dielectric permittivity was observed in the range from -36 to -38 °C. For the 65 nm pores, we

could instead distinguish two broad peaks in the derivative of the permittivity at -36 and -38 °C. These results can be interpreted by assuming that heterogeneous nucleation become less and less likely the smaller the pores become.

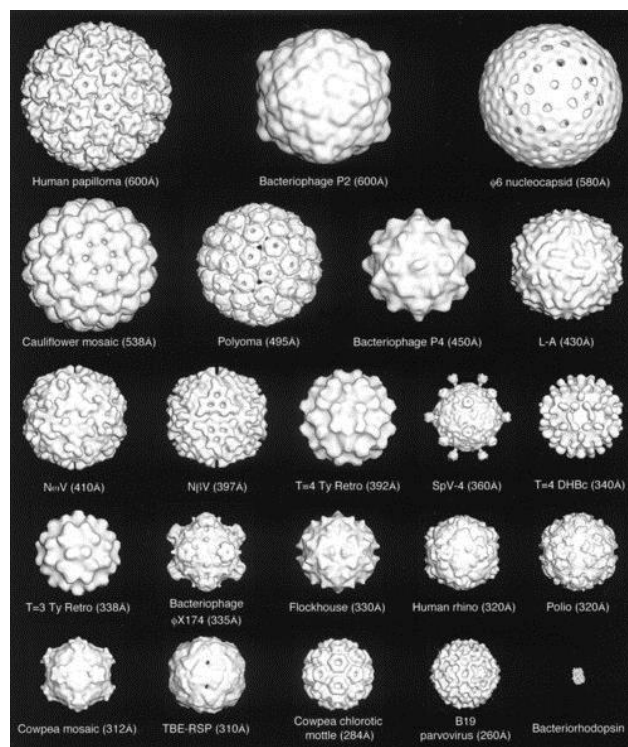


Figure 81. List of virus with their morphology and size. Most of their sizes are above 30 nm. The figure is taken from ref. [143].

Possible origins of heterogeneous nucleation (*i.e.*, impurities) in water

The reduced propensity for heterogeneous nucleation in the smaller pores can be discussed by water heterogeneities that are excluded in the smaller pores. This suggests that the size of most common heterogeneities in water exceed 35 nm. Indeed, biological impurities such as viruses have sizes above 30 nm (Figure 81). In addition, there exist several inorganic impurities. As an example, the list of possible inorganic impurities remaining in pure water (Wasser Ultra-Qualität (Roth)) is shown in Table 8. Since they are atomic size scale, they can easily enter the AAO pores with a pore diameter below 35 nm. Our data of small AAO pores implies that such inorganic impurities do not act as heterogeneous nuclei, at least for confined water. Alternatively, the pore curvature may also play some role in suppressing crystallization [124].

Table 8. List of possible inorganic impurities in pure water. The list is prepared based on the data of Wasser Ultra-Qualität (Roth).

Substance	Actual values	Substance	Actual values
Chloride ion (Cl ⁻)	< 1 ppb	Lead (Pb)	< 1 ppt
Phosphate (PO ₄ ³⁻)	< 1 ppb	Calcium (Ca)	< 10 ppt
Sulfate (SO ₄ ²⁻)	< 1 ppb	Gold (Au)	< 10 ppt
Aluminium (Al)	< 2 ppt	Potassium (K)	< 5 ppt
Antimon (Sb)	< 1 ppt	Copper (Cu)	< 2 ppt
Arsen (As)	< 2 ppt	Magnesium (Mg)	< 2 ppt
Barium (Ba)	< 1 ppt	Sodium (Na)	< 5 ppt
Nickel (Ni)	< 2 ppt	Selenium (Se)	< 10 ppt
Mercury (Hg)	< 10 ppt	Silver (Ag)	< 5 ppt
Tantalum (Ta)	< 5 ppt	Titan (Ti)	< 2 ppt

Existence of some liquid like layer

The value of the dielectric permittivity at low temperature (-90 °C) in AAO was higher than the limiting high-frequency permittivity of bulk ice ($\epsilon'_{\infty} \sim 3.2$) suggesting the presence of some undercooled water. A fraction of remaining liquid water was estimated in the following way. In all cases, the complex dielectric permittivity $\epsilon^* = \epsilon' - i\epsilon''$, where ϵ' is the real and ϵ'' is the imaginary part, was obtained at 1 MHz. This allows calculating the real and imaginary parts of the dielectric permittivity as a function of the respective volume fractions by using: $\epsilon^*_M = \epsilon^*_W \phi_W + \epsilon^*_A \phi_A$. First, we employed this relation in obtaining the porosity ϕ_W . For this purpose the measured permittivity values of water infiltrated nanoporous alumina at 20 °C were used ($\epsilon' = 16.3, 16.5, 8.4$ and 11.4 for 400 nm, 65 nm, 35 nm and 25 nm pores, respectively) together with the AAO value of $\epsilon_A = 2.6$. This resulted in porosities of 17.3 %, 17.5 %, 7.3 % and 11.1 %, respectively for 400 nm, 65 nm, 35 nm and 25 nm pores. We note here that these values are substantially smaller than earlier estimates based on SEM images or by weighting. Second, the measured permittivity values of water within AAO at -90 °C were employed ($\epsilon' = 3.83, 4.17, 4.2$ and 5.28 for 400 nm, 65 nm, 35 nm and 25 nm pores, respectively) and further assumed $\epsilon^*_M = \epsilon^*_{i1} \phi_{i1} + \epsilon^*_{ice} \phi_{ice} + \epsilon^*_A \phi_A$, where ϕ_{i1} and ϕ_{ice} are now the fractions of supercooled water and ice, respectively. Based on this, the limiting high frequency

permittivity value of ice ($\epsilon'_{\infty} \sim 3.2$) and the limiting low frequency permittivity of water ($\epsilon'_0 \sim 82$), the fraction of supercooled water was estimated as 1.4%, 1.9%, 2.0% and 3.3% for 400 nm, 65 nm, 35 nm and 25 nm pores, respectively.

Effect of cooling rate

The extent of homogeneous nucleation as compared to heterogeneous nucleation increased with increasing cooling rate, as shown in Figure 82, for water crystallizing within AAO with pore diameter of 200 nm. At relatively high cooling rates, the two processes were observed at -23 and at -38 °C, respectively. When cooling very slowly, that is, with a mere 1 K/min, heterogeneous nucleation dominated. This indicates that all 200 nm pores contain heterogeneities that can ignite crystallization. However, at the faster cooling rates, heterogeneous nucleation can be suppressed for kinetic reasons. In contrast, in AAO with pore diameters of 35 and 25 nm, water crystallization is exclusively initiated by homogeneous nucleation, independent of the cooling rate as shown in Figure 83.

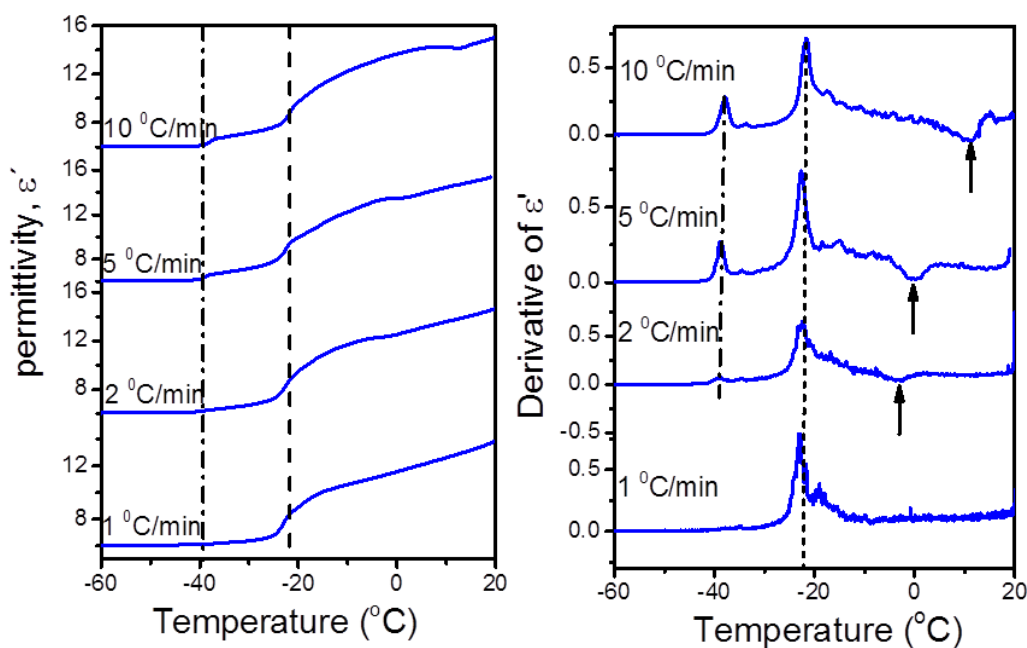


Figure 82. (Left) Permittivity of water in AAO with a pore diameter of 200 nm measured at different cooling rates. Vertical dashed and dash-dotted lines indicate the characteristic temperatures of heterogeneous and homogeneous nucleation, respectively. (Right) Derivative of dielectric permittivity curves as a function of temperature. Arrows indicate the rate dependence of the density anomaly of water in 200 nm pores.

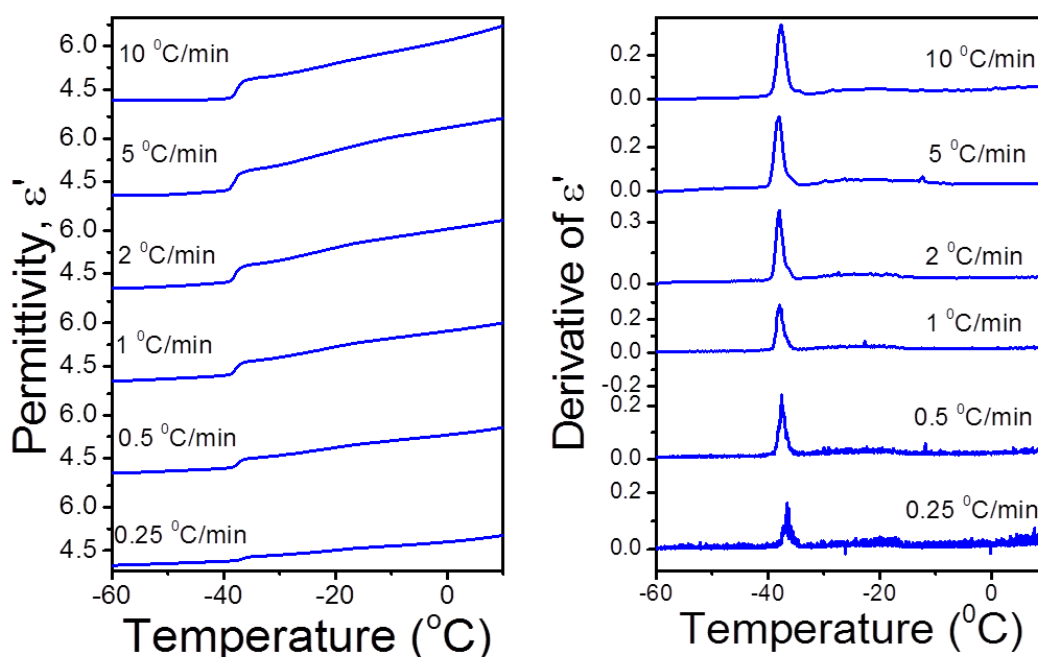


Figure 83. Rate dependence of dielectric permittivity for water within AAO with pore diameter of 25 nm. (Left) Permittivity obtained at a frequency of 1 MHz on cooling with different rates, as indicated. (Right) Derivative of dielectric permittivity curves as a function of temperature.

The nucleation mechanism as seen in DSC

These results on ice formation under uniform confinement are further supported by DSC. Figure 84 (left) shows DSC traces of water inside AAOs at a cooling rate of 10 K/min. Under these conditions, water inside 400 nm pore freezes predominantly at -10 °C via heterogeneous nucleation with a smaller exothermic peak at -40 °C revealing some homogeneous nucleation. In AAOs with 65 nm pores, two processes at -34 °C and at -42 °C were observed, reflecting ice formation via heterogeneous and homogeneous nucleation, respectively. For even smaller pores (35 nm and 25 nm), water freezes solely via homogeneous nucleation in agreement with dielectric spectroscopy results. Figure 84 (right) depicts the corresponding melting curves. The reason for slightly lower/higher temperatures during cooling/heating curves respectively in DSC as compared to DS is the higher thermal conductivity and higher cooling/heating rate in the former experiment. This is also the reason that the melting temperature of bulk water from DSC is slightly higher than 0 °C. Nevertheless a significant depression of the melting temperature with decreasing pore diameter is observed. In addition, as has been observed earlier, the enthalpy of melting is also decreasing with pore size. For example, for ice inside AAOs with 400 nm pores the enthalpy of melting is 3.5 kJ/mol whereas within 25 nm pores it is only 2.4 kJ/mol, that is, a fraction of the bulk value (~5.9 kJ/mol). Although this reduction

is beyond the expected one based on the lower crystallization temperatures within the 400 and 25 nm pores, we cannot make more quantitative discussion for all pores because of some evaporation during sample preparation in DSC.

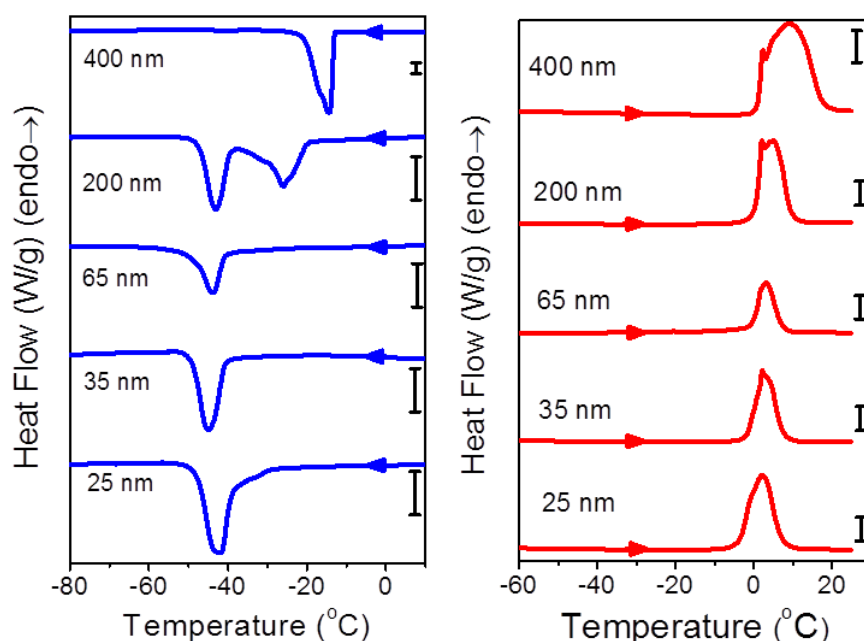


Figure 84. Differential scanning calorimetry traces of water inside AAO. (Left) DSC traces obtained upon cooling with 10 °C/min. (Right) DSC traces obtained upon heating with 10 °C/min immediately following cooling (left). The vertical bar indicates a scale of 1 W/g.

Phase diagram under confinement

The proposed “phase diagram” (Figure 85) of temperature versus curvature compiles the heterogeneous and homogeneous nucleation results from dielectric spectroscopy, DSC, and X-ray scattering. Instead of pressure as in a normal phase diagram, in this diagram, $1/d$ is used as horizontal axis. This is appropriate for confined systems because $1/d$ can be thought as proportional to the Laplace pressure. Hexagonal ice formed by heterogeneous nucleation predominates under moderate confinement. Under higher confinement characterized by a radius of curvature below 35 nm cubic ice formed by homogeneous nucleation dominates. Implicit is a correlation between the nucleation mechanism, the size of confinement and the type of ice crystals. In addition, Figure 85 includes the melting temperatures obtained from dielectric spectroscopy. The melting temperature decreases with the Gibbs-Thomson (GT) equation as $T_m(d) = T_m^{bulk} - K_{GT}/(d - d_0)$, where T_m^{bulk} is the bulk melting temperature, d_0

is the thickness of a premelted layer, and K_{GT} is a constant ($T_m^{bulk} = 271.1 \pm 0.6$ K, $K_{GT} = 76 \pm 3$ nm · K, and $d_0 = 0.30 \pm 0.003$ nm)

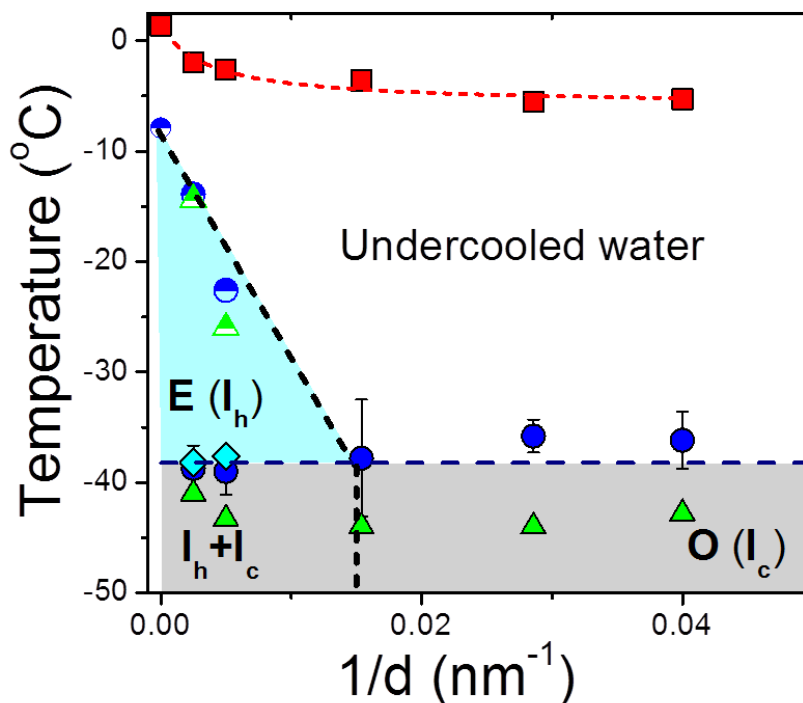


Figure 85. Effective phase diagram of water located inside AAO. The squares indicate the melting temperatures as a function of inverse pore diameter. The red-dashed line is the result of a fit to the Gibbs-Thomson equation. The half-filled circles indicate heterogeneous nucleation whereas the completely filled circles homogeneous nucleation as obtained from dielectric spectroscopy. Half-filled and completely filled triangles give the respective transition temperatures obtained from DSC. Gray and blue areas correspond to ice formation via homogeneous (O) and heterogeneous (E) nucleation, respectively. I_h indicates hexagonal ice, I_c predominantly cubic ice, whereas I_h+I_c indicates mixed crystals with predominantly hexagonal ice.

As listed in section 2, more than 10 different sources of water were examined. In all cases, a transition from heterogeneous to homogeneous nucleation was observed with decreasing pore size. However, as shown in Figure 86 schematically, the heterogeneous nucleation temperatures were not identical. It turned out that the heterogeneous nucleation line depends both on the quality of water and the quality of AAO (*i.e.* surface treatment at high temperature). In addition, stochastic nature of nucleation is also involved (see next chapter). Despite this, homogeneous nucleation is observed invariably for water located into AAO with pore diameters below 35 nm.

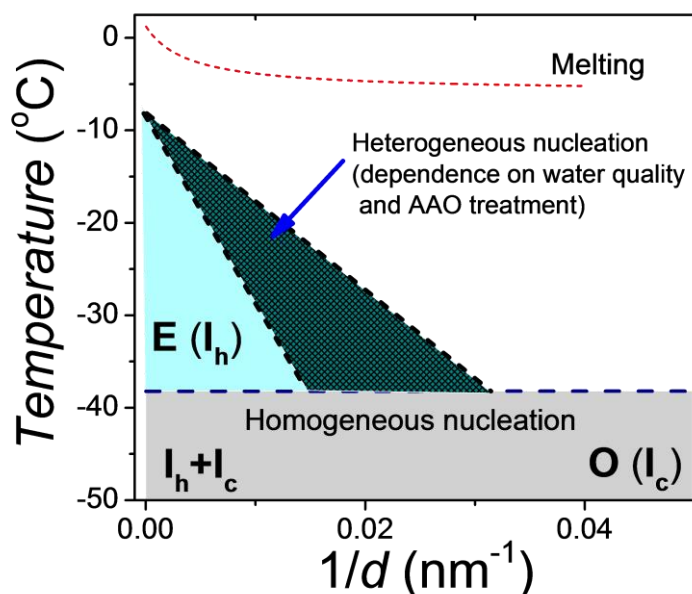


Figure 86. A schematic of heterogeneous nucleation range depending on the quality of water and the quality of the AAO. Stochastic nature of nucleation may also contribute (see below). Metastability range corresponds to meshed area. In any case, homogeneous nucleation is observed from water located into AAO with a pore diameter below 35 nm.

In conclusion, we demonstrated a correlation between the ice nucleation mechanism and the type of crystal structure: heterogeneous nucleation in larger pores gives the well-known hexagonal ice (I_h) whereas homogeneous nucleation in smaller pores results in a predominant cubic ice (I_c) instead. These results lead to a phase diagram of water under confinement. It contains a (stable) predominant I_c form below about 35 nm pores. The proposed phase diagram for confined water can have possible technical application in various research areas where water exists in confined spaces including construction materials like cement. The differential scanning calorimetry (DSC) curves of hardened Portland cement pastes for example, contain two well-defined peaks at $-41\text{ }^\circ\text{C}$ and $-23\text{ }^\circ\text{C}$ due that based on the proposed phase diagram reflect the homogeneous/heterogeneous freezing of water in different pore structures. In addition, the suppression of heterogeneous nucleation in the smaller AAO pores suggests that the majority of impurities in water have sizes that exceed 35 nm. This observation opens up the possibility of employing AAO templates as filters for ultra-pure water.

3.7. Kinetics of ice nucleation confined in AAO

Herein we investigate the kinetics of ice nucleation within the same AAOs. For this purpose we employ dielectric permittivity as a fingerprint of the ice nucleation mechanism under confinement in conjunction with structural probes (X-rays). We explore the heterogeneous and homogeneous nucleation kinetics for water located inside 400 and 25 nm, respectively, by performing temperature quench experiments to different final crystallization temperatures. Although both processes are stochastic in nature the range of metastability for heterogeneous and homogeneous nucleation is very different. Furthermore, before the onset of crystallization, water molecules undergo a structural relaxation associated with the formation of additional hydrogen bonds.

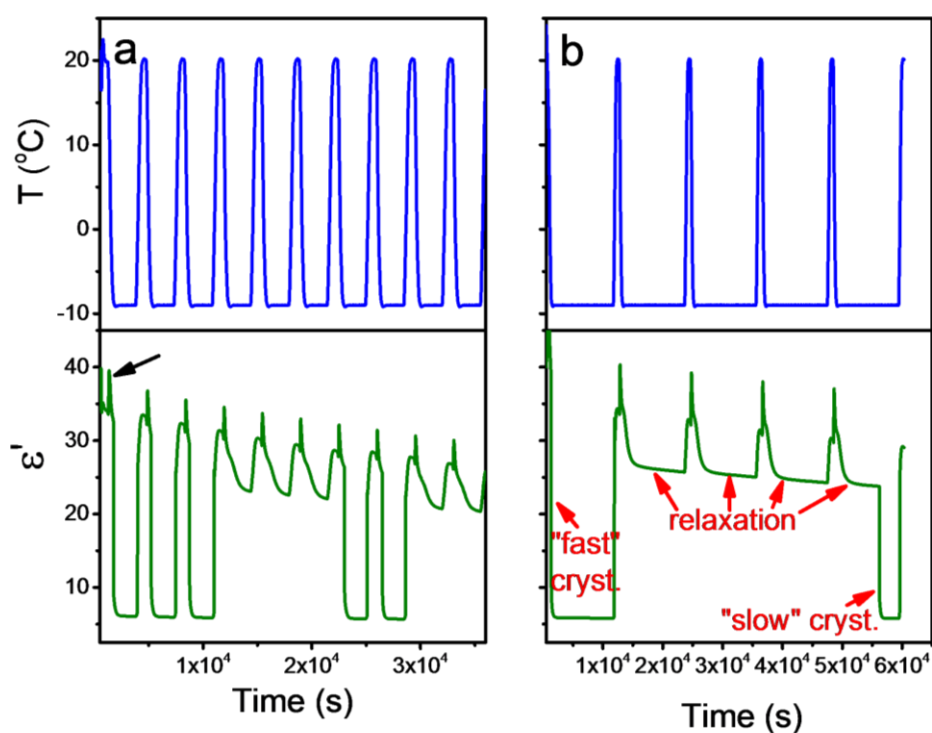


Figure 87. Temperature profiles (top) and dielectric permittivity curves as measured (bottom) for water inside AAO with a pore diameter of 400 nm. All measurements refer to water crystallization at -9 °C at a frequency of 1 MHz. Isochronal measurements refer to -9 °C for different time intervals: 40 min (a) or 3 hours (b).

Figure 87 gives the dielectric permittivity traces during consecutive cooling/heating runs for water located inside AAO with pore diameter of 400 nm at a frequency of 1 MHz. Results are shown for the crystallization kinetics from an initial temperature of 20 °C to the same final temperature of -9 °C and for different waiting times at the final temperature. The temperature profile during these runs is also shown for comparison. There are three features in the

permittivity traces that deserve attention. First, $\varepsilon'(T)$ displays a peak (arrows in Figure 87) during cooling at a temperature corresponding the density anomaly of water. Second, the traces clearly demonstrate that heterogeneous ice nucleation is a stochastic effect [125] [126]. Under some circumstances ice nucleates immediately after reaching the final temperature, otherwise, it can take much longer times. Third, once ice is nucleated within the pores it leads to the same limiting permittivity value ($\varepsilon'_\infty \sim 5 - 6$). By studying different crystallization temperatures, we conclude that these findings agree with the notion that heterogeneous nucleation is a stochastic process. As such it depends on the pore size, the degree of supercooling and the time interval.

The third observation, however, deserves more attention. It suggests, that somehow pores “communicate”, *i.e.*, the news on the crystallization in one pore are spread to all pores. The obvious communication through some liquid layer at the top of the template is excluded since this would enforce a heterogeneous nucleation independence of the pore size contrary to the experimental findings. Here we consider two possibilities; a heat wave and a sound wave. We first discuss the heat wave produced by freezing water within a single pore. We assume an array of parallel cylindrical pores with radius r ($=200$ nm) and length l ($=100$ μm). With a density of ice of 917 Kg/m^3 the mass of ice within a single pore is $m_i = 1.15 \times 10^{-14}$ Kg . Employing the latent heat, $L = 333$ kJ/Kg , the heat released by ice formation in a single pore is $Q_i = 3.8 \times 10^{-9}$ J . Such a heat will raise the temperature by $\Delta T = 157$ K ($\Delta T = Q_i / c_i m_i$, where c_i is the heat capacity of ice $= 2.093$ kJ/kg K [127]). With such a temperature gradient ice would melt instantly. As for the time scales of temperature equilibration these correspond to 3 ns in the radial direction ($t = r^2 / 4\kappa$, where $\kappa = 1.2 \times 10^{-5}$ m^2/s is the thermal diffusivity of alumina) and 0.4 ms along the whole AAO thickness, l ($t = l^2 / 2\kappa$). These estimates of the time scales should be considered as the shortest possible limits. They are ignoring phonon scattering in low dimensional systems with large surface-to-volume ratios (like AAOs) that can lead to a drastic reduction in thermal conductivity [128] [129].

On the other hand, a sound wave with velocity $u = (C_{11} / \rho)^{1/2}$ (with an elastic constant for alumina of $C_{11} \sim 500$ GPa and a density $\rho \sim 3.8$ g/cm^3) of $\sim 1.1 \times 10^4$ m/s takes a fraction of ps to traverse a distance of 400 nm. As to the origin of a sound wave, upon water crystallization the modulus increases by many orders of magnitude (practically from zero to about 10 GPa) [130]. This exerts a stress on the pore walls (the shear modulus of alumina is ~ 170 GPa) [131] and to a friction (probably stick-slip friction) across the interface. Above a certain stress, energy is released in the form of sound wave in pretty much the way that

seismic waves are travelling during an earthquake [130]. The sound wave communicates the “news” to the remaining pores.

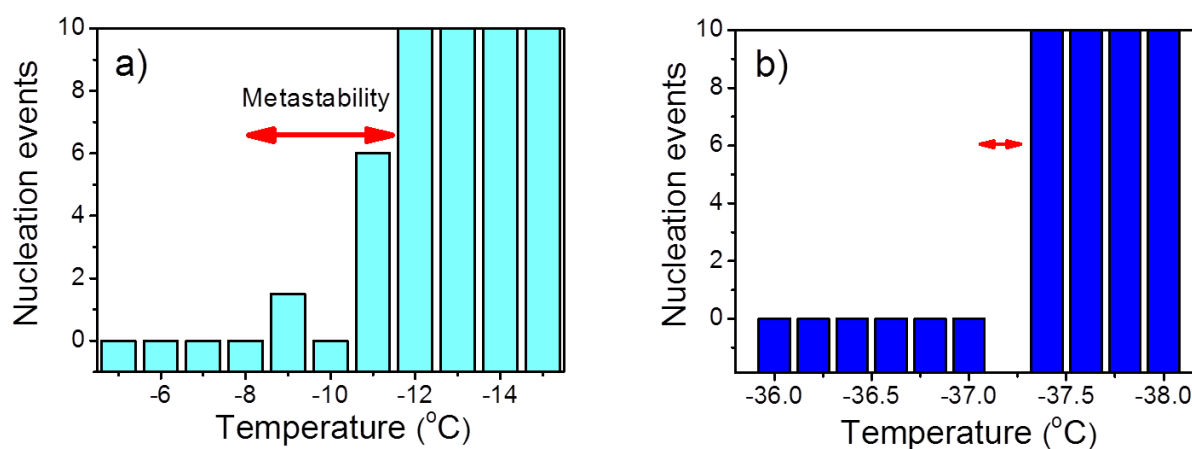


Figure 88. Number of nucleation events as a function of crystallization temperature following temperature jumps from 20 °C to different final temperatures for water inside AAO with pore diameter of 400 nm (a) and 25 nm (b). Red arrows indicate the range of metastability. Notice the much smaller temperature range in (b) corresponding to homogeneous nucleation.

The frequency of nucleation events, following crystallization within AAO with pore diameters of 400 nm and 25 nm at different final temperatures corresponding to heterogeneous nucleation, respectively, are depicted in Figure 88. The results for the heterogeneous ice nucleation reveal that metastability exists within the range from -8 to -11 °C. At temperatures above -8 °C water was unable to crystallize whereas at temperatures below about -12 °C ice was always formed during the kinetic runs. This suggests a metastability of ~4 °C for the heterogeneous ice nucleation under conditions of low undercooling. The same procedure was repeated for ice nucleation within 25 nm pores by following the $\varepsilon'(T)$ traces to lower temperatures. The result for the frequency of nucleation events during homogeneous nucleation is depicted in Figure 88 (b). It shows a much smaller range of metastability of only ~0.4 °C. The small range of metastability for homogeneous nucleation is consistent with some of the reported homogeneous ice nucleation rates. Assuming a single nucleation event per pore and a pore volume of $\sim 5 \times 10^{-14} \text{ cm}^3$ (for 25 nm pores) a nucleation rate of $\sim 10^{-14} \text{ cm}^3 \text{ s}^{-1}$ at 235 K [66] gives a freezing rate of $\sim 5 \text{ s}^{-1}$. On the other hand, nucleation rates close to some reported values of $\sim 10^{10} \text{ cm}^{-3} \text{ s}^{-1}$ [25] would give too low freezing rates to be observed experimentally. This point requires further work, for example, by performing nucleation rate measurements by fast calorimetry with the same AAO templates.

The characteristic time scales involved in the kinetics of heterogeneous ice nucleation are discussed next. The DS traces contain information on the relaxation of undercooled water as well as on the time scales involved in ice formation. One example is depicted in Figure 89.

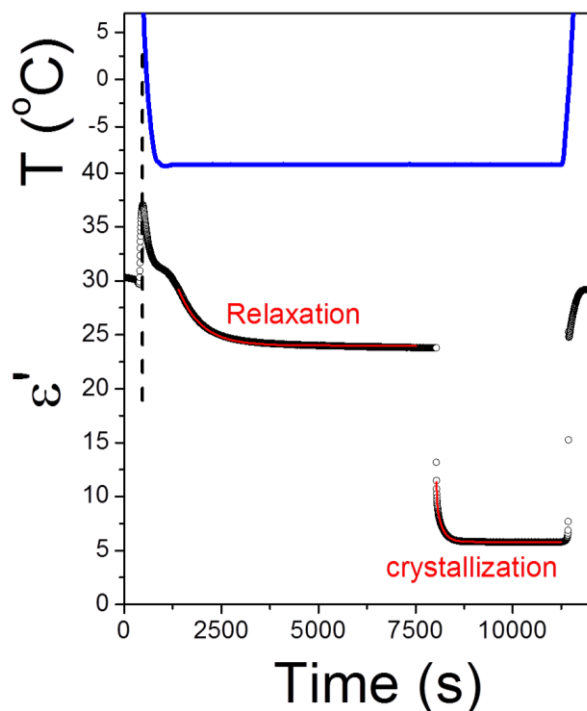


Figure 89. Temperature profile (top) and evolution of dielectric permittivity (bottom) for water inside AAO with a 400 nm pore diameter. The vertical dashed line gives the maximum value of permittivity that corresponds to the density anomaly of water. Red lines give the result of a fit to the relaxation process using a single exponential and to the crystallization process using a summation of two exponentials.

The figure shows characteristic times for final temperatures in the range from -5 to -13 °C. Invariably, *fast* crystallization occurs within 200 s after reaching the final temperature. A careful examination of the temperature profile during this process revealed that it occurs within the temperature variations (± 0.2 K) during temperature stabilization. However, heterogeneous nucleation is a stochastic process and when nucleation is not triggered by these temperature fluctuations then ice nucleation can take much longer time typically few hours. At intermediate times a relaxation of undercooled water takes place. From these results the temperature dependence of the relaxation times can be extracted and the result is plotted in Figure 90. The characteristic relaxation times within the narrow temperature interval of metastability show a Arrhenius temperature dependence $\tau = \tau_0 \exp(E/RT)$ with $\tau_0 = 5.6 \times 10^{-12}$ s and an activation energy, E , of ~ 50 kJ/mol. Such activation energy corresponds to the formation of few hydrogen bonds and suggests some reorganization (*i.e.* relaxation) of the undercooled water molecules in confinement. This observation is in line with results from neutron scattering on water in mesoporous silica [78]. There it was shown that confined water is more hydrogen bonded, and thus more structured than bulk water at the same temperature.

However, as we will discuss below with the help of X-rays, this reorganization does not lead to crystallization but may act as precursors to nucleation.

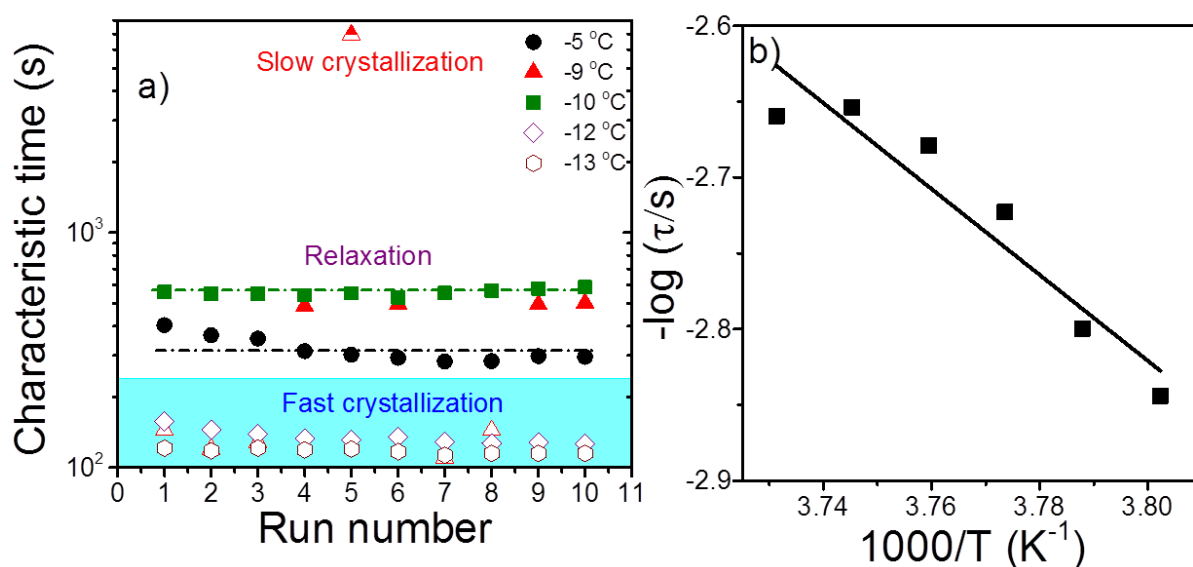


Figure 90. (a) Characteristic time corresponding to fast crystallization (empty symbols), slow crystallization (half-filled symbol) and relaxation before crystallization (filled symbols) obtained for water inside AAO templates with a pore diameter of 400 nm plotted as a function of run number. The characteristic times from different final crystallization temperatures are shown. Lines are guides for the eye at two “relaxation” experiments. (b) Mean relaxation time plotted as a function of inverse temperature. The line is the result of a linear fit.

The kinetics of homogeneous ice nucleation was studied by employing both dynamics/kinetic and structural probes. The dielectric permittivity at 1 MHz is followed for water inside AAO with pore diameter of 25 nm by making consecutive cooling/heating runs but to different final temperatures (Figure 91a).

The final temperatures were -10 °C, -20 °C, -30 °C and -40 °C where the sample stayed for 2 hours and the dielectric permittivity was continuously monitored. Subsequently, the structural aspects were studied by ex-situ WAXS at the same temperatures and the results are depicted in Figure 91b. For the cooling /heating run to a low temperature limit of -10 °C, it can be observed that the $\epsilon'(T)$ curve is not completely reversible due to some unavoidable evaporation at -10 °C. The subsequent cooling/heating run to a low temperature of -20 °C (point 3 in Figure 91) is nearly completely reversible (due to the lower evaporation at this temperature). The structure at this temperature corresponds to amorphous supercooled water as indicated by the absence of any sharp diffraction peaks (the shallow peaks are attributed to some water condensation). The next cooling/heating run to -30 °C does not initiate any

crystallization. However, cooling to below $-38\text{ }^{\circ}\text{C}$ results to ice nucleation and to a non-reversible dielectric permittivity curve. On heating, $\epsilon'(T)$ the values remain constant up to the melting point at $\sim -5\text{ }^{\circ}\text{C}$.

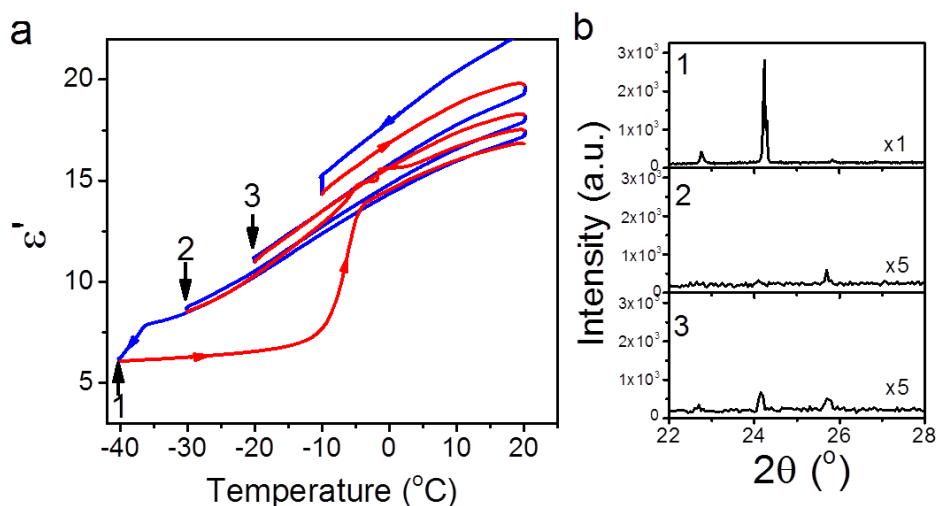


Figure 91. (a) Dielectric permittivity during consecutive cooling (blue curves)/ heating (red curves) of water inside AAO with a pore diameter of 25 nm. The template was cooled from $20\text{ }^{\circ}\text{C}$ to different final temperatures ($-10\text{ }^{\circ}\text{C}$, $-20\text{ }^{\circ}\text{C}$, $-30\text{ }^{\circ}\text{C}$ and $-40\text{ }^{\circ}\text{C}$) where stayed for 2 hours. (b) Diffraction patterns obtained ex-situ for (top) a template that was cooled to $-50\text{ }^{\circ}\text{C}$ (cooling speed of $5\text{ }^{\circ}\text{C}/\text{min}$), (middle) the same template cooled at $-30\text{ }^{\circ}\text{C}$ (cooling speed of $5\text{ }^{\circ}\text{C}/\text{min}$) and (bottom) cooled to $-20\text{ }^{\circ}\text{C}$ (cooling speed of $5\text{ }^{\circ}\text{C}/\text{min}$). The diffraction patterns taken at $-30\text{ }^{\circ}\text{C}$ and at $-20\text{ }^{\circ}\text{C}$ are multiplied by a factor of 5. Arrows give the corresponding annealing temperatures in (a).

In conclusion, the combined analyses using dielectric spectroscopy and X-ray scattering techniques could capture the details of the kinetics of ice nucleation under confinement. We found that both heterogeneous and homogeneous nucleation, obtained at low and high undercooling respectively, are stochastic in nature involving variable degrees of metastability. The range of metastability is $\sim 4\text{ }^{\circ}\text{C}$ and $0.4\text{ }^{\circ}\text{C}$ for heterogeneous and homogenous nucleation, respectively. Nucleation within a single pore is spread to all pores in the template. We have examined here a possible coupling of all pores through a heat wave and a sound wave. Finally, prior to crystallization undercooled water molecules relax with an activation energy of $\sim 50\text{ kJ/mol}$ corresponding to the formation of few hydrogen bonds. This corroborates the notion that confined water is more structured than bulk water.

3.8. Dynamics of water/ice under confinement

Dynamics of supercooled water and ice in AAO were studied with dielectric spectroscopy. Figure 92 gives the dielectric loss spectra for water located inside AAO templates as function of frequency for a range of different temperatures. They all show a discontinuous decrease of the dielectric loss curves whose magnitude and exact temperature is a function of the AAO pore diameter as anticipated from the dielectric permittivity data show in Figure 92. For example, for water located inside AAO with pores of 400 nm in diameter the discontinuous change occurs at 263 K whereas inside pores with diameters of 65 nm and 25 nm at 235 K. As we discussed earlier, this reflects a different mechanism of ice nucleation; from heterogeneous nucleation of hexagonal ice within the 400 nm pores to homogenous nucleation of predominantly cubic ice within the smaller pores. Furthermore, the curves depict at least two processes in the high frequency side and a more intense process in the low frequency side.

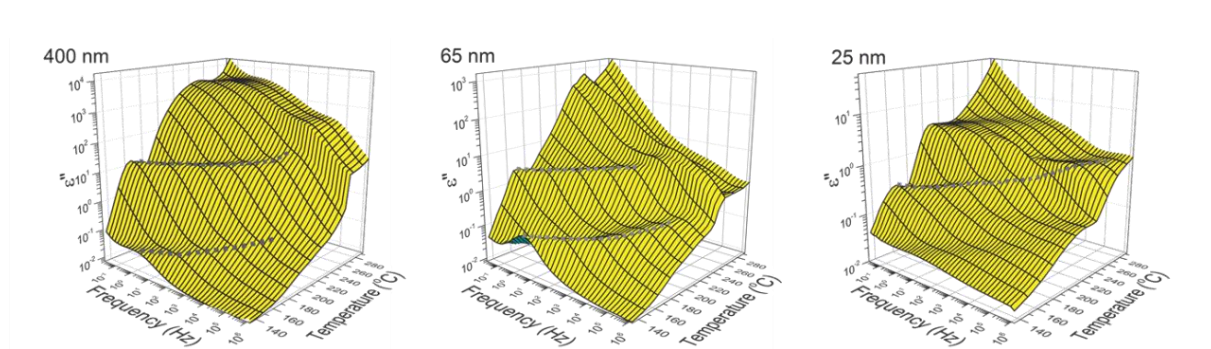


Figure 92. Dielectric loss curves in a 3D representation for water located inside AAOs with different pore sizes. Gray dots indicate the frequency positions of the main process of ice relaxation under confinement.

For the analyses of the processes under confinement a summation of two HN processes was necessary. Figure 93 shows some representative fits of the dielectric loss spectra at $T=183$ K. The data for bulk ice are from ref. [88]. It depicts a single albeit non-Debye process. The effect of confinement is three-fold: first the main process shifts to lower frequencies (*i.e.*, becomes slower on confinement). Second, the process is broadened and third, another faster process appears at higher frequencies. In addition, the main process for ice within 400nm AAO is coupled to the process of ionic conductivity (extracted from the crossing frequency of the real and imaginary parts) whereas in the smaller pores the latter process is slower than the process corresponding to the maximum of the dielectric loss. This suggests a different mechanism of ice relaxation in the larger and smaller pores.

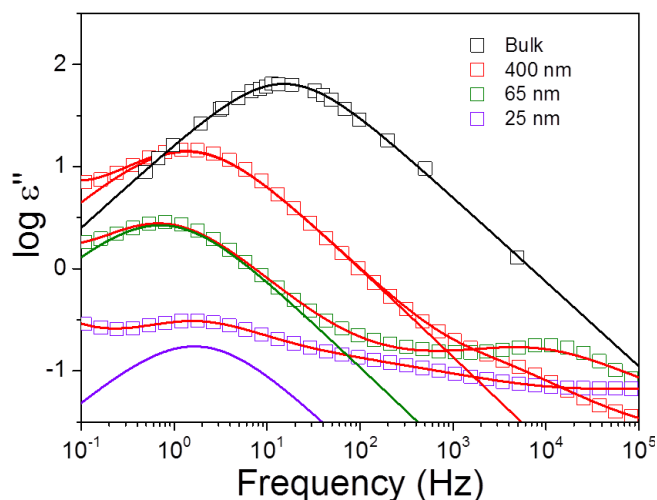


Figure 93. Dielectric loss curves of ice in the bulk (from ref. [88]) and inside AAO with different pore diameters. All data refer to 183 K. Black lines are fits to a single HN (bulk) or to a summation of two HN processes. Dashed lines give the slower process for ice within AAO.

The low frequency HN shape parameter for the main process is plotted in Figure 94 as a function of temperature for some AAO pore diameters. In the bulk, measurements on ice single crystals revealed a single relaxation process of the Cole-Cole type ($n=1$) or Debye type ($m=n=1$) at temperatures below or above 250 K, respectively. For ice located inside AAO, the distribution of relaxation times for the main process is very broad and furthermore depends on the pore size. Apparently, confinement results in a variety of environments that are reflected on a variety of rates.

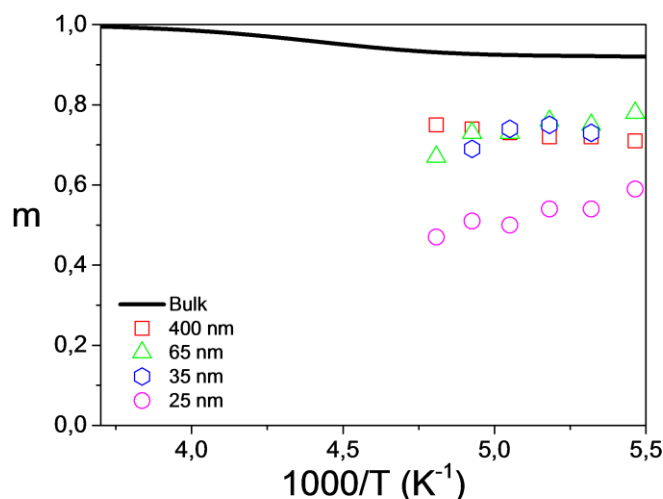


Figure 94. Temperature dependence of low frequency HN shape parameter of the main process corresponding to bulk ice (the data is taken from ref. [84].) and to ice located inside AAO. There is a significant broadening of the dynamics of ice on confinement.

In the bulk, the distribution of relaxation times in I_h was attributed to the presence of impurities that generate orientational defects that are thought to be spatially heterogeneous, *i.e.*, different regions relax with different rates. Apart from the distribution of relaxation times, the characteristic frequency at maximum loss and in particular its temperature dependence has been debated. Figure 95 shows literature data of ice I_h relaxation as a function of temperature. It depicts three characteristic temperature regimes. At high temperatures ice relaxes via an Arrhenius temperature dependence with an activation energy of ~ 53 kJ/mole. At intermediate temperatures it follows another Arrhenius dependence with an activation energy of ~ 19 kJ/mol. At lower temperatures the activation energy increases again to ~ 46 kJ/mol. However, while the high temperature crossover is distinct in the $\tau(T)$ dependence the same is not true for the crossover at lower temperatures. Therefore, as discussed in the introduction, several attempts have been made to explain the origin of the high temperature dynamic crossover. Bjerrum proposed an orientation mechanism for the dielectric relaxation and conductivity of I_h crystals that violates the Bernal-Fowler-Pauling rules and produce two kinds of orientational defects; one with a pair of neighboring O \cdots O atoms missing a hydrogen (L-defect) and one with a pair of neighbors O-H H-O, *i.e.*, with two hydrogen atoms (D-defect). Water molecules can reorient by the diffusion of L and D defects. Different ideas have been proposed to explain the dynamic crossover. In one it was suggested that the crossover reflects the reorientation of a single molecule at high temperatures and a concerted reorientation of several molecules at low temperatures. A second approach attributed the crossover to a decrease in concentration of intrinsically generated defects by decreasing temperature. Lastly, a more recent approach discussed the competition of L/D orientational defects with the generation and migration of ionic defects that dominate at higher and intermediate temperatures, respectively.

The dynamics of ice located inside AAOs is depicted in Figure 95 together with the bulk ice data. Interestingly, the main process under confinement has an Arrhenius temperature dependence with an activation energy $E \sim 44$ kJ/mol, *i.e.*, similar to bulk ice in the high temperature region. This could suggest the dominance of orientational L/D defects under confinement. Moreover, a faster process exists with a lower activation energy.

Finally, it would be interesting to compare the dynamics under confinement with recent studies of high density amorphous ice (HDL) produced via pressure. The results, shown with lines in Figure 95, depict a low temperature process with an Arrhenius temperature dependence. On heating HDL transforms to another metastable state corresponding to low density amorphous ice (LDL) with an activation energy of 34 kJ/mol. On further heating,

LDL transforms to the thermodynamically stable cubic ice I_c state. Interestingly, the relaxation times of I_c produced via homogenous nucleation within AAO templates at ambient pressure are in the vicinity of the I_c produced in bulk through a totally different path: HDL \rightarrow LDL \rightarrow I_c . In addition, the faster process under confinement has rates intermediate to the LDL and HDL processes.

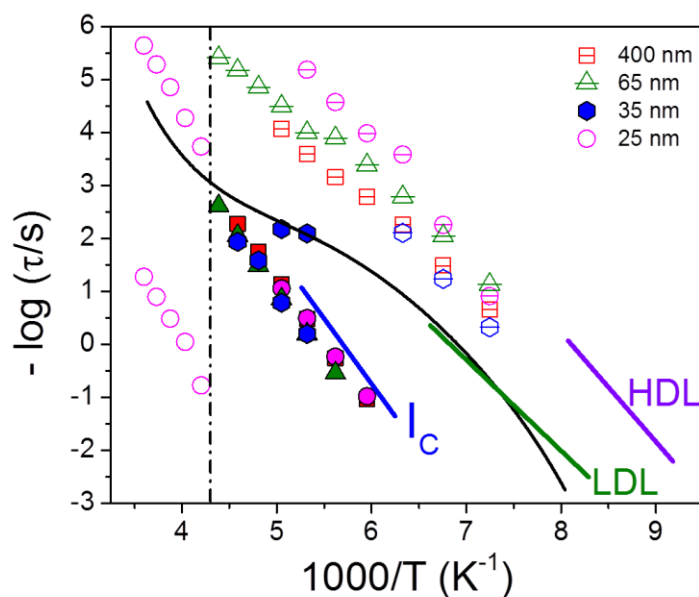


Figure 95. Relaxation times of bulk ice (solid line is from ref. [85]) and of ice/water confined to AAO at maximum loss based on fitting with the Havriliak-Negami function. The vertical dash-dotted line at 235 K is the temperature of homogeneous nucleation in the smaller pores. The colored lines correspond to the dynamics of cubic ice (blue), low density liquid (LDL: green) and high density liquid (HDL: purple) from ref. [64].

4. Conclusion

In this Thesis, crystallization of some diverse soft materials like polymers and water was investigated with the aim to better understand *how*, *why* and *when* soft materials crystallize under confinement. We find that polymers crystallize via heterogeneous nucleation in the bulk and via homogeneous nucleation in the smaller pores with reduced crystallinity and exhibit strong crystal orientation effects. Subsequently, we investigated the effect of polydispersity, additives and oligomers on the nucleation mechanism. In particular, the effect of oligomers supports the notion that homogeneous nucleation and liquid-to-glass temperature are intimately connected. These findings are summarized at the pertinent phase diagram shown in Figure 96 (left).

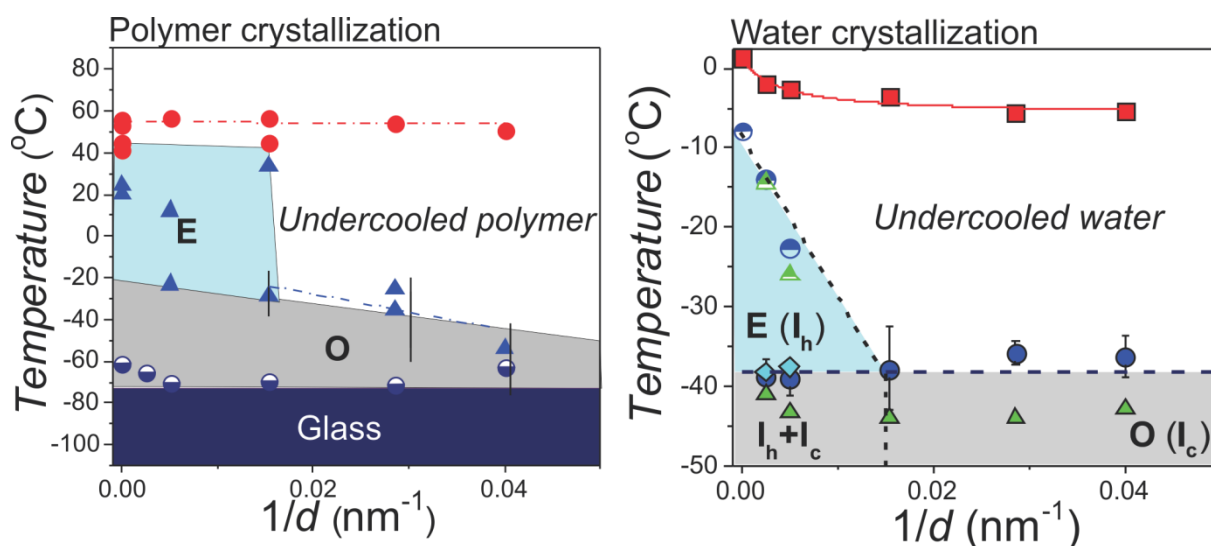


Figure 96. Comparison of the phase diagrams from semicrystalline polymers and of water under confinement. E denotes regions of *heterogeneous* nucleation whereas O denotes regions of *homogeneous* nucleation. In water crystallization, I_h corresponds to hexagonal ice and I_c corresponds to cubic ice.

With respect to ice nucleation within the same AAOs, we find a direct connection between the crystallization pathway and the ice phase that is formed. Ice formation proceeds via heterogeneous nucleation in larger pores and by homogeneous nucleation in the smaller pores. Furthermore, there is a phase transformation from the usual hexagonal ice in the larger pores to a predominantly cubic ice below about 35 nm pores. Interestingly, cubic ice is not metastable to its hexagonal form but a stable phase under confinement at ambient pressure. Again these findings are summarized at the pertinent phase diagram shown in Figure 96 (right).

By comparing the two phase diagrams we come to the conclusion that they are not fundamentally different. Within pores with diameter of around 35 nm, a “transition” from heterogeneous nucleation to homogeneous nucleation is observed in both cases. The main similarities and differences are summarized in the table below.

Table 9. Summary of similarities and differences of polymer crystallization and water crystallization under confinement within AAO templates.

Similarities	Differences
<ul style="list-style-type: none"> - Fundamentally similar phase diagrams. - Heterogeneous nucleation dominates at low undercooling whereas homogeneous nucleation prevails at high undercooling. - As a result, the nucleation mechanism can be controlled by selecting appropriate pore sizes. - In both cases there are strong effects on crystal size, perfection and orientation. 	<ul style="list-style-type: none"> - Homogeneous nucleation temperature is nearly independent from pore size in confined water. This is reflecting the high nucleation rates for ice formation under submicron size confinement. - Homogeneous nucleation temperature in confined polymers is in the vicinity of the liquid-to-glass temperature. However, the homogeneous nucleation temperature in confined water is much above the reported liquid-to-glass temperature(s).

This, at first site, is surprising, since water is a small molecule much smaller than the smaller pore. However, because of the extended network of hydrogen bonds it behaves similar to a polymer (*i.e.* “polywater”).

The results presented herein could be of importance in designing polymeric materials with pre-determined crystallinity and hence with controlled mechanical, electrical and optical properties. Similarly, the proposed phase diagram of confined water can have application in areas where water exists in confined space like construction materials. In addition, complete suppression of heterogeneous nucleation in AAO pores having diameters ≤ 35 nm opens up the possibility of employing AAO templates as filters for ultrapure water.

5. References

- [1] C. A. Angell, *Science* **267**, 1924 (1995).
- [2] P. G. Debenedetti and F. H. Stillinger, *Nature* **410**, 259 (2001).
- [3] P. W. Anderson, *Science* **267**, 1615 (1995).
- [4] H. Sillescu, *J. Non. Cryst. Solids* **243**, 81 (1999).
- [5] A. Deres, G. Floudas, K. Müllen, M. Van Der Auweraer, F. De Schryver, J. Enderlein, H. Uji-I, and J. Hofkens, *Macromolecules* **44**, 9703 (2011).
- [6] K. Fukao and Y. Miyamoto, *Phys. Rev. E* **61**, 1743 (2000).
- [7] Z. Fakhraai and J. A Forrest, *Science* **319**, 600 (2008).
- [8] C. L. Jackson and G. B. McKenna, *J. Chem. Phys.* **93**, 9002 (1990).
- [9] A. Keller, *Philos. Mag.* **2**, 1171 (1957).
- [10] E. W. Fischer, *Z. Naturforsch* **12a**, (1957).
- [11] U. W. Gedde, *Polymer Physics* (Springer-Science+Business Media, B.V., 1995).
- [12] P.H.Till, *J.Polym.Sci* **24**, (1957).
- [13] G. Strobl, *Rev. Mod. Phys.* **81**, 1287 (2009).
- [14] L. H. Palys and P. J. Phillips, *J. Polym. Sci. Polym. Phys. Ed.* **18**, 829 (1980).
- [15] E. Zhuravlev, J. W. P. Schmelzer, B. Wunderlich, and C. Schick, *Polymer*. **52**, 1983 (2011).
- [16] M. Imai, K. Kaji, T. Kanaya, and Y. Sakai, *Phys. Rev. B* **52**, 12696 (1995).
- [17] H. Asakawa, K. Nishida, G. Matsuba, T. Kanaya, and H. Ogawa, *J. Phys. Conf. Ser.* **272**, 012024 (2011).
- [18] H. Asakawa, K. Nishida, J. Yamamoto, R. Inoue, and T. Kanaya, *Polymer*. **53**, 2777 (2012).
- [19] K. Mita, H. Okumura, K. Kimura, T. Isaki, M. Takenaka, and T. Kanaya, *Polym. J.* **45**, 79 (2012).
- [20] E. Q. Chen, X. Weng, A. Zhang, I. Mann, F. W. Harris, S. Z. D. Cheng, R. Stein, B. S. Hsiao, and F. Yeh, *Macromol. Rapid Commun.* **22**, 611 (2001).
- [21] G. Hauser, J. Schmidtke, and G. Strobl, *Macromolecules* **31**, 6250 (1998).

- [22] H. Duran, M. Steinhart, H.-J. Butt, and G. Floudas, *Nano Lett.* **11**, 1671 (2011).
- [23] H. Duran, A. Gitsas, G. Floudas, M. Mondeshki, M. Steinhart, and W. Knoll, *Macromolecules* **42**, 2881 (2009).
- [24] B. Vonnegut, *J. Colloid Sci.* **3**, 563 (1948).
- [25] A. Manka, H. Pathak, S. Tanimura, J. Wölk, R. Strey, and B. E. Wyslouzil, *Phys. Chem. Chem. Phys.* **14**, 4505 (2012).
- [26] A. Taden and K. Landfester, *Macromolecules* **36**, 4037 (2003).
- [27] M. V Massa, J. L. Carvalho, and K. Dalnoki-Veress, *Eur. Phys. Journal. E* **12**, 111 (2003).
- [28] M.V Massa and K. Dalnoki-Veress, *Phys. Rev. Lett.* **92**, 255509 (2004).
- [29] Y. Loo, R. Register, and A. Ryan, *Phys. Rev. Lett.* **84**, 4120 (2000).
- [30] G. Reiter, G. Castelein, J.-U. Sommer, A. Röttele, and T. Thurn-Albrecht, *Phys. Rev. Lett.* **87**, 226101 (2001).
- [31] Y.-L. Loo, R. Register, and A. Ryan, *Macromolecules* **35**, 2365 (2002).
- [32] A. Röttele, T. Thurn-Albrecht, J.-U. Sommer, and G. Reiter, *Macromolecules* **36**, 1257 (2003).
- [33] Y.-L. Loo, R. A. Register, A. J. Ryan, and G. T. Dee, *Macromolecules* **34**, 8968 (2001).
- [34] H. Chen, S. Hsiao, T. Lin, K. Yamauchi, H. Hasegawa, and T. Hashimoto, *Macromolecules* **34**, 671 (2001).
- [35] N. Hadjichristidis, S. Pispas, and G. Floudas, *Block Copolymers* (2003).
- [36] M. W. Matsen and F. S. Bates, *Macromolecules* **29**, 1091 (1996).
- [37] A. K. Khandpur, S. Forster, F. S. Bates, I. W. Hamley, A. J. Ryan, W. Bras, K. Almdal, and K. Mortensen, *Macromolecules* **28**, 8796 (1995).
- [38] E. Woo, J. Huh, Y. G. Jeong, and K. Shin, *Phys. Rev. Lett.* **98**, 136103 (2007).
- [39] H. Duran, M. Steinhart, H. H.-J. Butt, and G. Floudas, *Nano Lett.* **11**, 1671 (2011).
- [40] J. Maiz, J. Martin, and C. Mijangos, *Langmuir* **28**, 12296 (2012).
- [41] J. Mart, A. Nogales, and C. Mijangos, *Macromolecules* **46**, 7415 (2013).
- [42] J. Maiz, H. Schäfer, G. Trichy Rengarajan, B. Hartmann-Azanza, H. Eickmeier, M. Haase, C. Mijangos, and M. Steinhart, *Macromolecules* **46**, 403 (2013).
- [43] Y. Cao, H. Wu, Y. Higaki, H. Jinnai, and A. Takahara, *IUCrJ* **1**, 439 (2014).

- [44] J. M. Giussi, I. Blaszczyk-Lezak, M. S. Cortizo, and C. Mijangos, *Polymer*. **54**, 6886 (2013).
- [45] M. Salsamendi, N. Ballard, B. Sanz, J. M. Asua, and C. Mijangos, *RSC Adv.* **5**, 19220 (2015).
- [46] L. Li, D. Zhou, D. Huang, and G. Xue, *Macromolecules* **47**, 297 (2014).
- [47] M. Hofmann, a. Herrmann, S. Ok, C. Franz, D. Kruk, K. Saalwächter, M. Steinhart, and E. a. Rössler, *Macromolecules* **44**, 4017 (2011).
- [48] M. Krutyeva, A. Wischniewski, M. Monkenbusch, L. Willner, J. Maiz, C. Mijangos, A. Arbe, J. Colmenero, A. Radulescu, O. Holderer, M. Ohl, and D. Richter, *Phys. Rev. Lett.* **110**, (2013).
- [49] I. Blaszczyk-lezak, H. Marianella, and C. Mijangos, *Macromolecules* **46**, 4995 (2013).
- [50] J. Maiz, W. Zhao, Y. Gu, J. Lawrence, A. Arbe, A. Alegría, T. Emrick, J. Colmenero, T. P. Russell, and C. Mijangos, *Polymer*. **55**, 4057 (2014).
- [51] S. Alexandris, G. Sakellariou, M. Steinhart, and G. Floudas, *Macromolecules* **47**, 3895 (2014).
- [52] J. D. Thrower, M. P. Collings, M. R. S. McCoustra, D. J. Burke, W. A. Brown, A. Dawes, P. D. Holtom, P. Kendall, N. J. Mason, F. Jamme, H. J. Fraser, I. P. Clark, and A. W. Parker, *J. Vac. Sci. Technol. A* **26**, 919 (2008).
- [53] J. Thrower, A. Abdulgalil, M. Collings, M. McCoustra, D. Burke, W. Brown, A. Dawes, P. Holtom, P. Kendall, N. Mason, F. Jamme, H. Fraser, and F. Rutten, *J. Vac. Sci. Technol. A* **28**, 799 (2010).
- [54] D. H. Bager and E. J. Sellevold, *Cem. Concr. Res.* **16**, 709 (1986).
- [55] P. V. Hobbs, *Ice Physics* (Oxford University Press, 2010).
- [56] A. Falenty, T. C. Hansen, and W. F. Kuhs, *Nature* **516**, 231 (2014).
- [57] J. Russo, F. Romano, and H. Tanaka, *Nat. Mater.* **13**, 733 (2014).
- [58] O. Mishima and H. E. Stanley, *Nature* **396**, 329 (1998).
- [59] G. Tammann and J. Starinkewitsh, *Z. Phys. Chem.* **85**, 573 (1913).
- [60] O. Mishima, L. D. Calvert, and E. Whalley, *Nature* **310**, 393 (1984).
- [61] O. Mishima, L. D. Calvert, and E. Whalley, *Nature* **314**, 76 (1985).
- [62] E. Mayer, a Hallbrucker, G. Sartor, and G. P. Johari, *J. Phys. Chem.* **99**, 5161 (1995).
- [63] C. A. Angell, *Science* **319**, 582 (2008).

- [64] K. Amann-Winkel, C. Gainaru, P. H. Handle, M. Seidl, H. Nelson, R. Böhmer, and T. Loerting, *Proc. Natl. Acad. Sci. U. S. A.* **110**, 17720 (2013).
- [65] P. H. Poole, F. Sciortino, U. Essmann, and H. E. Stanley, *Nature* **360**, 324 (1992).
- [66] D. E. Hagen, R. J. Anderson, and J. L. Kassner, *J. Atmos. Sci.* **38**, 1236 (1981).
- [67] R. J. Anderson, R. C. Miller, J. L. Kassner, and D. E. Hagen, *J. Atmos. Sci.* **37**, 2508 (1980).
- [68] T. L. Malkin, B. J. Murray, V. Andrey, J. Anwar, C. G. Salzmänn, and A. V. Brukhno, *Proc. Natl. Acad. Sci.* **109**, 4020 (2012).
- [69] E. Whalley, *Science*. **211**, 389 (1981).
- [70] E. Mayer and A. Hallbrucker, *Nature* **325**, 601 (1987).
- [71] J. Huang and L. S. Bartell, *J. Phys. Chem.* **99**, 3924 (1995).
- [72] B. J. Murray, D. A. Knopf, and A. K. Bertram, *Nature* **434**, 202 (2005).
- [73] J. E. Shilling, M. A. Tolbert, O. B. Toon, E. J. Jensen, B. J. Murray, and A. K. Bertram, *Geophys. Res. Lett.* **33**, 1 (2006).
- [74] G. P. Arnold, E. D. Finch, S. W. Rabideau, and R. G. Wenzel, *J. Chem. Phys.* **49**, 4365 (1968).
- [75] T. C. Hansen, M. M. Koza, P. Lindner, and W. F. Kuhs, *J. Phys. Condens. Matter* **20**, 1 (2008).
- [76] P. J. Stewart, D. J.C., and R. a Webster, *J. Phys. Chem.* **87**, 2458 (1983).
- [77] K. Morishige and K. Kawano, *J. Chem. Phys.* **110**, 4867 (1999).
- [78] J. Dore, *Chem. Phys.* **258**, 327 (2000).
- [79] G. H. Findenegg, S. Jähnert, D. Akcakayiran, and A. Schreiber, *ChemPhysChem* **9**, 2651 (2008).
- [80] G. P. Johari, *J. Chem. Phys.* **130**, (2009).
- [81] E. Tombari and G. P. Johari, *J. Chem. Phys.* **139**, 064507 (2013).
- [82] T. L. Malkin, B. J. Murray, C. G. Salzmänn, V. Molinero, S. J. Pickering, and T. F. Whale, *Phys. Chem. Chem. Phys.* **17**, 60 (2015).
- [83] K. Thürmer and S. Nie, *Proc. Natl. Acad. Sci. U. S. A.* **110**, 11757 (2013).
- [84] I. Popov, A. Puzenko, and Y. Feldman, *Phys. Chem. Chem. Phys.* **17**, 1489 (2014).
- [85] G. P. Johari, *J. Chem. Phys.* **75**, 1333 (1981).

- [86] G. P. Johari and S. J. Jones, Proc. R. Soc. A Math. Phys. Eng. Sci. **349**, 467 (1976).
- [87] R. P. Auty and R. H. Cole, J. Chem. Phys. **20**, 1309 (1952).
- [88] S. R. Gough and D. W. Davidson, J. Chem. Phys. **52**, 5442 (1970).
- [89] T. Loerting, V. Fuentes-landete, P. H. Handle, M. Seidl, K. Amann-winkel, C. Gainaru, and R. Böhmer, J. Non. Cryst. Solids **407**, 423 (2015).
- [90] H. Masuda and K. Fukuda, Science. **268**, 1466 (1995).
- [91] W. Lee, R. Ji, U. Gösele, and K. Nielsch, Nat. Mater. **5**, 741 (2006).
- [92] H. Marand, J. Xu, and S. Srinivas, Macromolecules **31**, 8219 (1998).
- [93] A. Gitsas and G. Floudas, Macromolecules **41**, 9423 (2008).
- [94] G. Floudas, *2.41 Dielectric Spectroscopy (DS) in Polymer Science: A Comprehensive Reference* (Elsevier, 2011).
- [95] G. Floudas, M. Paluch, A. Grzybowski, and K. L. Ngai, *Molecular Dynamics of Glass-Forming Systems. Effects of Pressure* (Springer, 2011).
- [96] S. Havriliak and S. Negami, Polymer. **8**, 161 (1967).
- [97] N. Yamaguchi and M. Sato, Polym. J. **41**, 588 (2009).
- [98] F. Kremer and A. Schönhal, *Broadband Dielectric Spectroscopy* (Springer, Berlin, 2002).
- [99] C. Grigoriadis, H. Duran, M. Steinhart, M. Kappl, H. J. Butt, and G. Floudas, ACS Nano **5**, 9208 (2011).
- [100] H. Duran, B. Hartmann-azanza, M. Steinhart, D. Gehrig, X. Feng, and K. Müllen, ACS Nano **6**, 9359 (2012).
- [101] J. Choi, Y. Luo, R. B. Wehrspohn, R. Hillebrand, J. Schilling, and U. Gösele, J. Appl. Phys. **94**, 4757 (2003).
- [102] Y. Takahashi, I. Sumita, and H. Tadokoro, J. Polym. Sci. Polym. Phys. Ed. **11**, 2113 (1973).
- [103] U. Tracht, M. Wilhelm, a. Heuer, H. Feng, K. Schmidt-Rohr, and H. Spiess, Phys. Rev. Lett. **81**, 2727 (1998).
- [104] J. E. Mark, *Physical Properties of Polymers Handbook*, 2nd ed. (Springer, 2007).
- [105] I. W. Hamley, J. Phys. Condens. Matter **13**, 643 (2001).
- [106] E. L. Thomas, D. M. Anderson, C. S. Henkee, and D. Hoffman, Nature **334**, 598 (1988).

- [107] F. B. Khambatta, F. Warner, T. Russell, and R. S. Stein, *J. Polym. Sci., Part B Polym. Phys.* **14**, 1391 (1976).
- [108] B. M. Baysal and W. H. Stockmayer, *Macromolecules* **27**, 7429 (1994).
- [109] M. Alcoutlabi and G. B. McKenna, *J. Phys. Condens. Matter* **17**, 461 (2005).
- [110] M. M. Elmahdy, K. Chrissopoulou, A. Afratis, G. Floudas, and S. H. Anastasiadis, *Macromolecules* **39**, 5170 (2006).
- [111] S. Nakagawa, K. I. Kadana, T. Ishizone, S. Nojima, T. Shimizu, K. Yamaguchi, and S. Nakahama, *Macromolecules* **45**, 1892 (2012).
- [112] Y. Sen Sun, T. M. Chung, Y. J. Li, R. M. Ho, B. T. Ko, U. S. Jeng, and B. Lotz, *Macromolecules* **39**, 5782 (2006).
- [113] G. R. Strobl, *The Physics of Polymers* (Springer, Berlin, 2007).
- [114] M. P. Howard and S. T. Milner, *Macromolecules* **46**, 6600 (2013).
- [115] A. J. Müller, V. Balsamo, and M. L. Arnal, *Adv. Polym. Sci.* **190**, 1 (2005).
- [116] R. M. Michell, A. T. Lorenzo, A. J. Müller, M. C. Lin, H. L. Chen, I. Blaszczyk-Lezak, J. Martín, and C. Mijangos, *Macromolecules* **45**, 1517 (2012).
- [117] A.-C. Shi and B. Li, *Soft Matter* **9**, 1398 (2013).
- [118] G. Floudas, G. Reiter, O. Lambert, and P. Dumas, *Macromolecules* **31**, 7279 (1998).
- [119] G. Floudas, G. Reiter, O. Lambert, P. Dumas, F. J. Yeh, and B. Chu, in *ACS Symp. Ser.* (2000), pp. 448–455.
- [120] S. Jiang, C. He, Y. Men, X. Chen, L. An, S. S. Funari, and C. M. Chan, *Eur. Phys. J. E* **27**, 357 (2008).
- [121] H. Bittiger, R. H. Marchessault, and W. D. Niegisch, *Acta Crystallogr. Sect. B Struct. Crystallogr. Cryst. Chem.* **26**, 1923 (1970).
- [122] B. J. Murray and A. K. Bertram, *Phys. Chem. Chem. Phys.* **8**, 186 (2006).
- [123] B. J. Murray, *Environ. Res. Lett.* **3**, 025008 (2008).
- [124] L. Lupi, A. Hudait, and V. Molinero, *J. Am. Chem. Soc.* **136**, 3156 (2014).
- [125] M. C. Cross and P. C. Hohenberg, *Rev. Mod. Phys.* **65**, 851 (1993).
- [126] L. Goh, K. Chen, V. Bhamidi, G. He, N. C. S. Kee, P. J. A. Kenis, C. F. Zukoski, and R. D. Braatz, *Cryst. Growth Des.* **10**, 2515 (2010).
- [127] M. Sugisaki, H. Suga, and S. Seki, *Bull. Chem. Soci* **41**, 2591 (1968).

- [128] M. Maldovan, *Nature* **503**, 209 (2013).
- [129] S. Neogi, J. S. Reparaz, L. F. C. Pereira, B. Graczykowski, M. R. Wagner, M. Sledzinska, A. Shchepetov, M. Prunnila, J. Ahopelto, C. M. Sotomayor-Torres, and D. Donadio, *ACS Nano* **9**, 3820 (2015).
- [130] A. Godio and R. B. Rege, *J. Appl. Geophys.* **115**, 92 (2015).
- [131] R. G. Munro, *J. Am. Ceram. Soc.* **80**, 1919 (1997).
- [132] C. V. Thompson and F. Spaepen, *Acta Metall.* **27**, 1855 (1979).
- [133] W. Kurz and D. J. Fisher, *Fundamentals of Solidification*, Fourth Rev (Trans Tech Publications, 1998).
- [134] J. Lauritzen and J. Hoffman, *J. Res. Natl. Bur. Stand. Sect. A. Phys. Chem.* **64**, 73 (1960).
- [135] J. D. Hoffman, G. T. Davis, and J. I. Lauritzen, *Cryst. Noncrystalline Solids* **7**, (1976).
- [136] G. Floudas, B. Vazaiou, F. Schipper, R. Ulrich, U. Wiesner, H. Iatrou, and N. Hadjichristidis, *Macromolecules* **34**, 2947 (2001).
- [137] T. Bartels-Rausch, V. Bergeron, J. H. E. Cartwright, R. Escibano, J. L. Finney, H. Grothe, P. J. Gutiérrez, J. Haapala, W. F. Kuhs, J. B. C. Pettersson, S. D. Price, C. I. Sainz-Díaz, D. J. Stokes, G. Strazzulla, E. S. Thomson, H. Trinks, and N. Uras-Aytemiz, *Rev. Mod. Phys.* **84**, 885 (2012).
- [138] J. E. McDonald, *J. Meteorol.* **10**, 416 (1953).
- [139] L. Dowell and A. Rinfret, *Nature* **118**, 1144 (1960).
- [140] J. E. Bertie and S. M. Jacobs, *J. Chem. Phys.* **67**, 2445 (1977).
- [141] C. G. Salzmann, E. Mayer, and A. Hallbrucker, *Phys. Chem. Chem. Phys.* **6**, 1269 (2004).
- [142] K. Morishige and H. Uematsu, *J. Chem. Phys.* **122**, 44711 (2005).
- [143] T. S. Baker, N. H. Olson, and S. D. Fuller, *Microbiol. Mol. Biol. Rev.* **63**, 862 (1999).

Acknowledgements

(removed)

Appendix A: Abbreviations and acronyms

AAO	Anodic Aluminum Oxide
AFM	Atomic Force Microscopy
DS	Dielectric Spectroscopy
DSC	Differential Scanning Calorimetry
e.g.	exempli gratia, for example
G-T equation	Gibbs-Thomson equation
I _c	Cubic ice
I _h	Hexagonal ice
I _{sd}	Stacking-disordered ice
i.e.	it est, that is
LH theory	Lauritzen-Hoffman theory
HDA	High density amorphous ice
LDA	Low density amorphous ice
ODPA	Octadecyl phosphonic acid
PCL	Poly(ϵ -caprolactone)
PEO	Poly(ethylene oxide)
PEO- <i>b</i> -PCL	Diblock copolymers of poly(ethylene oxide)- <i>b</i> -poly(ϵ -caprolactone)
POM	Polarizing Optical Microscopy
WAXS	Wide Angle X-ray Scattering
SAXS	Small Angle X-ray Scattering
SEM	Scanning Electron Microscopy
TEM	Transmission Electron Microscopy
vs.	versus

Appendix B: Symbols used in equations

A	Area
d	The pore diameter
E	Activation energy
G	Gibbs free energy
ΔG_V	The Gibbs free energy difference between the liquid and the solid per unit volume
H	Enthalpy
ΔH_f	the bulk enthalpy of fusion
K	Mean curvature
L	Volumetric latent heat of fusion
N	Total degree of polymerization
P	Pressure
r	radius
r_1, r_2	The principal radii curvature
r^*	critical nucleus radius
S	Entropy
ΔS_f	the entropy of fusion per unit volume
T	Temperature
T_0	The “ideal” glass temperature
T_c	Crystallization temperature
T_g	Liquid-to-glass temperature
T_m'	Apparent melting temperature
T_m^0	The equilibrium melting temperature
T_{zg}^0	The zero growth temperature
u	The growth rate
u_0	The initial growth rate
Z	The number of nearest neighbor monomers configuration cell
ϵ_{AB}	The interaction energy per monomer units between A and B monomers
ρ	Density
ρ_s	The density of the solid

σ	Surface energy
σ_e	The fold surface free energy
σ_{sl}	The surface energy of the solid-liquid interface
χ_{AB}	The segment-segment interaction (Flory-Huggins) parameter
N	The total degree of polymerization
F	The volume fraction

Appendix C: Derivation of equation (1.4) based on ref [132], [133]

The difference in Gibbs free energy between the liquid and crystalline phase is given by

$$\Delta G = \Delta H - T\Delta S \quad (1)$$

where

$$\Delta H = \Delta H_f - \int_T^{T_m} \Delta C_p dT \quad (2)$$

and

$$\Delta S = \Delta S_f - \int_T^{T_m} \Delta C_p \frac{dT}{T} \quad (3)$$

and where T_m is the melting temperature, ΔS_f is the entropy of fusion, ΔH_f is the enthalpy of fusion and ΔC_p defined as $C_p^l - C_p^x$ is the difference in specific heats of the two phases. Here, ΔC_p calculated from extrapolated C_p^l data, can often be satisfactorily described by the linear relation

$$\Delta C_p = K_1 T + K_2 \quad (4)$$

This relation leads to a free energy difference given by

$$\Delta G = \frac{\Delta H_f \Delta T}{T_m} - \frac{1}{2} K_1 (\Delta T)^2 + K_2 \left(T \ln \frac{T_m}{T} - \Delta T \right) \quad (5)$$

where

$$\Delta T \equiv T_m - T$$

This can be simplified by use of the approximation

$$\ln \left(\frac{T_m}{T} \right) \cong \frac{2\Delta T}{T_m + T} \quad (6)$$

which is strictly valid only for small ΔT . However, in the temperature range of interest here ($T_m/2 < T < T_m$), this leads to errors in ΔG of less than 4% at the largest undercoolings.

Then, equation (5) can be simplified to

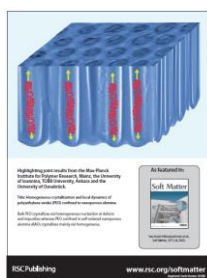
$$\Delta G = \frac{\Delta H_f \Delta T}{T_m} - (\Delta T)^2 \left(\frac{1}{2} K_1 + \frac{K_2}{T_m + T} \right) \quad (7)$$

If the value of ΔC_p is unknown, the simplest assumption (and one which is quite reasonable for metals) is that $\Delta C_p = 0$. This leads to:

$$\Delta G = \frac{\Delta H_f \Delta T}{T_m} = \Delta S_f \Delta T \quad (8)$$

List of publications

- [1] **Y. Suzuki**, M. Steinhart, H.-J. Butt, and G. Floudas, “Kinetics of ice nucleation confined in nanoporous alumina” **J. Phys. Chem. B**, 119, 11960 (2015).
- [2] **Y. Suzuki**, H. Duran, M. Steinhart, M. Kappl, H.-J. Butt, and G. Floudas, “Homogeneous Nucleation of Predominantly Cubic Ice Confined in Nanoporous Alumina” **Nano Lett.** 15, 1987 (2015).
- [3] **Y. Suzuki**, H. Duran, M. Steinhart, H. Butt, and G. Floudas, “Suppression of Poly (ethylene oxide) Crystallization in Diblock Copolymers of Poly (ethylene oxide) -b-poly (ϵ -caprolactone) Con fi ned to Nanoporous Alumina” **Macromolecules** 47, 1793 (2014).
- [4] **Y. Suzuki**, H. Duran, W. Akram, M. Steinhart, G. Floudas, and H.-J. Butt, "Multiple nucleation events and local dynamics of poly(ϵ -caprolactone) (PCL) confined to nanoporous alumina" **Soft Matter** 9, 9189 (2013).
- [5] **Y. Suzuki**, H. Duran, M. Steinhart, H.-J. Butt, and G. Floudas, "Homogeneous crystallization and local dynamics of poly(ethylene oxide) (PEO) confined to nanoporous alumina" **Soft Matter** 9, 2621 (2013).



- [6] **Y. Suzuki**, J. Hunger, M. Steinhart, M. Bonn, H.-J. Butt, and G. Floudas, “Dynamics of ice confined in nanoporous alumina“ **J. Phys. Chem. B**, 119, 11960 (2015)
- [7] **Y. Suzuki**, H. Duran, M. Steinhart, H.-J. Butt, and G. Floudas, “Effect of additives, polydispersity and mixing on polymer crystallization confined to nanoporous alumina” **J. Phys. Chem. B**, accepted